Research Article

A Novel Approach for Automatic Car Plate Detection and Recognition

Fattah Alizadeh [a, *], **Sazan Luqman** [b]

Department of Computer Science and Engineering, School of Science and Engineering, University of Kurdistan Hewlêr, Erbil, KRI, Iraq

E-mail: [a] f.ibrahim@ukh.edu.krd, [b] s.bibani@ukh.edu.krd

Access this article online		
Received on: January 18, 2020	**Accepted on:** November 20, 2021	**Published on:** December 28, 2021
DOI: 10.25079/ukhjse.v5n2y2021.pp1-9	**E-ISSN:** 2520-7792	

Abstract

The increasing number of cars inside cities creates problems in traffic control. This issue can be solved by implementing a computer-based automatic system known as the Automatic Car Plate Recognition System (ACPRS). The main purpose of the current paper is to propose an automatic system to detect, extract, segment, and recognize the car plate numbers in the Kurdistan Region of Iraq (KRI). To do so, a frontal image of cars is captured and used as an input of the system. After applying the required pre-processing steps, the SURF descriptor is utilized to detect and extract the car plate from the whole input image. After segmentation of the extracted plate, an efficient projection-based technique is being exploited to describe the available digits and the city name of the registered car plate. The system is evaluated over 200 sample images, which are taken under various testing conditions. The best accuracy of the proposed system, under the controlled condition, shows the high performance and accuracy of the system which is 94%.

Keywords: Automatic Car Plate Recognition, SURF Descriptor, Segmentation, Character Recognition, Digit Recognition, Horizontal Projection, Vertical Projection.

1. Introduction

During the last decade, Image processing and computer vision have gained enormous attention from researchers from various fields of study such as medical, security, game, agriculture, etc. Traffic control (Davies *et al.*, 1990), car owner identification (Draghici, 1997), automatic toll collection (Lotufo *et al.*, 1990), Automatic vehicle parking system (Albiol *et al.*, 2011), etc. are among the dozen applications of image processing for which the car plate (license) should be automatically detected, extracted and recognized. Therefore, the Automatic Car Plate Recognition (ACPR) has become an interesting field of study among researchers in the literature.

The typical ACPR system gets a car plate (or car image which includes the car plate), as input and generates the combination of letters, digits, and words by which a car plate can be identified.

Besides the high speed and accuracy of ACPR systems, invariance to the light condition, rotation, and scale transformations are the decent features that an ideal system should be empowered with.

One of the main steps of any ACPR system is the accurate extraction of the car plates which is referred to as Car Plate Localization. The results of this step will be directly reflected in the next stages of the whole system for the recognition process.

The Car Plate Recognition step, on the other hand, is the core part of the system by which the extracted car plates should be segmented, described and recognized, correctly.

Several studies have postulated a direct relationship between the accuracy of the segmentation process and the recognition rate, so the better segmentation of the alphanumeric symbols of the plates, the more precise the car plate recognition result.

As will be shown in the next section, plenty of previous researches into ACPR have mainly focused on the recognition of the car plates, rather than the localization (Algainahi, 2011), that is, the input image of such systems is considered to be a manually-extracted well-aligned image of car plates.

In this paper, a fully automated novel approach of ACPR system is presented by which the car plates of the Kurdistan Region of Iraq will be detected, segmented, and recognized. The system acquires the frontal image of the vehicle, in different sizes and directions, and performs the preprocessing operations, then the required steps toward recognizing the car plate letters and digits will be applied.

The proposed system will perform both localization (detection) and recognition of the car plates at the same time. The plate's location will be detected from the frontal image of the car. Then, the extracted part will be passed to the recognition part of the system. This part will segment the available symbols and recognize them using an effective and efficient descriptor. A detailed description of the proposed system is presented in section 3.

The rest of this paper is organized as follows: the next section will briefly discuss some similar researches that have been conducted in the literature. Then, we will present a detailed description of the proposed system in section 3. Practical results of the simulated system will be shown in section 4. And finally, a summary of the main findings, together with the future works is provided in the last section.

2. Literature Review

Since the first appearance of ACPR systems in 1979 in Britain, the literature on automatic car plate recognition has highlighted several approaches to improve the accuracy and efficiency of such systems. Valuable surveys on the efforts done in the literature can be found in (Patel *et al.* 2013) and (Amatya & Sarvanan, 2017). Due to the closer relationship between the current work and the Arabic/Persian ACPR systems, this section is mainly dedicated to reviewing the techniques done in Iran and the Arabic countries.

An Iraqi ACPR system using a template matching approach has been proposed by Abbas and Hashem (2016). Their system includes two main phases: car plate detection and recognition. After the pre-processing stage, plate detection using Sobel edge detection is performed followed by the removal of undesired objects. On the other hand, the correlated template matching approach was used for recognizing the digits, letters, and words which resulted in 98.2% of accuracy.

Another Arabian ACPR system for Egyptian cars was proposed in 2013 (Massoud *et al.*, 2013). According to the authors' claim, unlike the other systems, their system gets video stream as input, but they have not clarified the process of selecting the appropriate frame. The car plates are extracted using Sobel edge detection followed by dilation, and erosion to locate the rectangular areas. Finally, the characters and digits have been described and recognized via the statistical cross-correlation approach. Under a controlled testing condition on 100 car plates, an accuracy rate of 91% has been achieved.

In a different work, the multi-resolution scheme along with Hidden Markov Model (HMM) have been leveraged for recognition of Arabic (Indian) digits (Awaidah & Mahmoud, 2009). The authors have followed a trial and error scheme to estimate the best size and states of the HMM. They used structural, gradient, and concavity as features of the numbers. The experiments on their dataset, having 21120 sample images show an average accuracy rate of 99%.

Ebrahimi *et al.* (2015) have recently introduced an ACPR system for the Iranian car plates. They have detected the car plates using the blue margins available for all typical Iranian car plates and used Support Vector Machine as an approach for the plate recognition. Their achievement rates were 90%, 95%, and 97% for plate detection, segmentation, and recognition, respectively.

To the best of our knowledge, there are only two research that has been conducted for ACPR in the Kurdistan Region of Iraq (Ali *et al.*, 2015) and (Wady *et al.,* 2017). Regardless of the common steps, they have followed, the main difference between their works is related to the descriptors they have leveraged; in the former study, the cluster of Gabor feature vectors along with Support Vector Machine and Neural Network were used for the feature extraction and recognition phase, while the Haar Wavelet transformation and a color histogram is the underlying descriptor in the latter one. As the result of evaluation under various illumination conditions, the best optimal accuracy of the Neural Network-based approach was 96.72%

Despite the availability of several studies and implemented ACPR systems, a gap still exists between the existing systems and the ideal ones. Accurate localizing of the plate under various viewing/ weather conditions is among the gaps which are being tackled in the current paper.

3. Proposed Approach

In this section the proposed ACPR system and its sub-systems will be described, a general view of the system is illustrated in Figure 1.

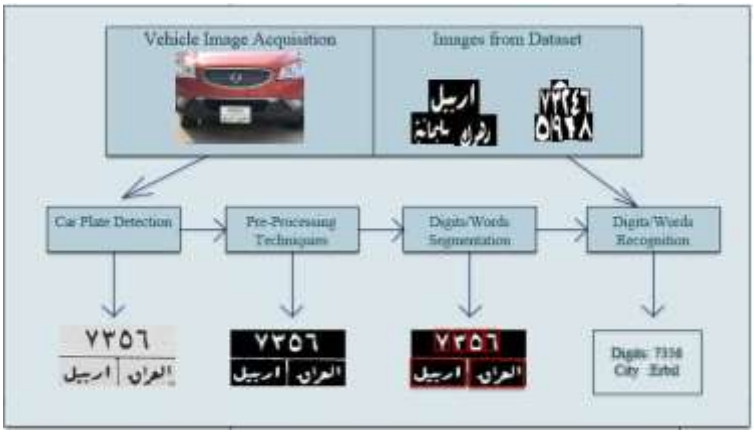

Figure 1. The Overview of the Proposed System.

3.1. Image Acquisition

Any ACPR system begins with the image acquisition step. This stage aims to capture the image of frontal view of the vehicle using a digital camera. The image also can be loaded from a pre-stored dataset of police stations. The images might differ in size, color, distance, angles and resolution depending on the utilized camera. Figure 2 shows a set of sample images that will be utilized as the input of the system.

Figure 2. A Set of Sample Images of Car Plates in the Kurdistan Region. (Note That the Plates Can Have a White, Yellow, or Red Background).

3.2. Image Pre-Processing

As mentioned before, the input image might have some variations in terms of size and alignment. Furthermore, the images might be degraded due to the presence of noise, low-resolution deficiency, etc. Therefore, the input images should go through several pre-processing operations such as resizing all images to 200*200 pixels, converting the color image into a grey scale and binary one, and then the de-noising process. Figure 3 shows a sample image before and after applying the preprocessing operations. As depicted in this figure, there are several undesired black spots appear in the original image which has been removed after pre-processing step.

Figure 3. A Sample Car Image After Binarization and Noise Removal.

It is worthwhile to mention that for the car plates having a red background, an extra pre-processing is required for the following reasons: in such car plates, the foreground of the plate (digits and words) are written in white color which is different from other plates. So, after binarizing the images in the pre-processing step, the color of the foreground and the background should be swapped to be consistent with the other car plates.

3.3. Car Plate Localization (Detection):

Due to its effect on the total accuracy of the recognition process, car plate detection plays a significant role in any typical ACPR system. Although some of the available ACPR systems perform automatic car plate extraction, accurate localization of plates is still among the hot topics which have attracted researchers' attention. In the current work we have employed, an efficient fast approach, using SURF descriptor (Bay *et al.*, 2006), to detect car plate location.

In the following sub-sections, the structure of the car plates is firstly presented and then the proposed approach for car plate localization will be illustrated.

3.3.1. Car Plate Structure

The car plates of the Kurdistan Region of Iraq, which are different from the rest of the country, have a unique template. As illustrated in Figure 4 the upper part of the plate comprises 1 to 6 digits, written in Arabic script which specifies the plate number. The background colors of the plates are white, red, or yellow. In the right side of the lower part, the unique word of "العراق" (Iraq) appears beside the left sub-part which includes the name of one of the three main provinces of the region: اربيل (Erbil), دهوک (Dohuk) or سليمانيه (Sulaymaniyah).

a) b)

Figure 4. Car Plate Structure in KRI. A) General Template of Car Plates, B) Sample Car Plates.

3.3.2. Car Plate Extraction

In this work, the Speeded Up Robust Features (SURF) descriptor is utilized for separating the car plate region from the whole image. To do so, a simple and efficient shape matching approach has been used; As mentioned in the previous section, a common sub-image which contains the word "العراق" is available in all car plates of the region. Therefore, according to the structure of the car plates, the SURF descriptor is utilized to find the part of "العراق" (which is available in the right half of the lower part of the plates). The similarity measurement process is performed to match between the target image and a pre-stored binary sample image of word" العراق" (see Figure 5 which, will hereafter be referred to as "base image").

Figure 5. A Sample Image of the Common Part of the Plates (Base Image).

Figure 6 illustrates the matching between a sample input image and the base one. As shown in this figure, despite the variation in the size and orientation of the input image, the key points of the images can be matched correctly, as the SURF descriptor is rotation and scale-invariant.

Figure 6. Matching Between Input and Base Images Using SURF Descriptor.

After locating the car plate in the image, using some geometrical relationship, the full image of the car plate will be extracted and rotated to be aligned properly. The final image of the plate will be fed as an input to the next stage, which is known as the segmentation phase. Figure 7 depicts an extracted car plate from a sample input image.

Figure 7. An Input Image and the Extracted Aligned Car Plate.

3.4. Car Plate Segmentation:

The extracted car plate should be segmented twice to be ready for the recognition phase; the first segmentation separates the upper part of the plate (which includes plate digits) from the lower part (which comprises the city name of the plate and the word "العراق"). On the other hand, the second segmentation should be performed on the upper part to distinguish between the digits.

Since the shapes of the car plates in the region follow a unique standard (in terms of size and location), by dividing the car plate evenly into upper/lower parts and later by dividing the lower part into two equal-size halves, the sub-parts can be easily extracted from the plate.

The final step of segmentation should be performed to extract the digits from the upper part segment of the plate. To this end, the connected component labeling algorithm (He *et al.*, 2017) is applied on the upper part of the plate to extract the individual digits. As the result of this step, separated components that specify available digits will be extracted and finally are saved individually in a separate file for the further process of recognition. Figure 8 depicts the result of the segmentation phase applied on a sample car plate.

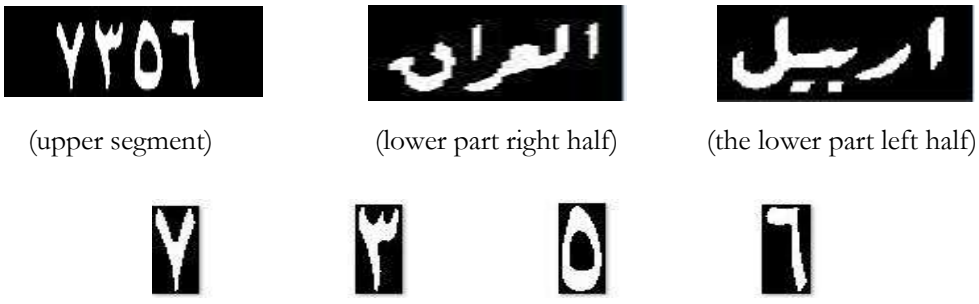

(upper segment) (lower part right half) (the lower part left half)

(segmented individual digits)

Figure 8. The Segmented Parts of the Car Plate.

3.5. Car Plate Description and Recognition

The input data of the recognition phase are the extracted digits of the car plates along with the city name of the plate which will be described and recognized, separately.

Similar to any object recognition system, the objects (digits/city name) should be described using a robust descriptor by which the shapes are represented as a set of numerical vectors or an appropriate graph. The underlying descriptors of the digits later will be compared to those which have already been saved in the dataset. The minimum distance between the target image and the saved ones indicates the digit.

In this research, the vertical and horizontal projection of the pixels is utilized as an efficient robust descriptor to recognize each segmented digit/word.

Vertical/Horizontal projection is the procedure that translates two-dimensional images into one-dimensional vector. A horizontal projection vector is the summation of all pixel values (foreground) in each row in the black and white image and is saved in a vector. Similarly, vertical projection is the summation of all pixel values (foreground) in each column in a black and white image and is kept in a vector. Figure 9. shows the vertical and horizontal projection for the sample digit ٦.

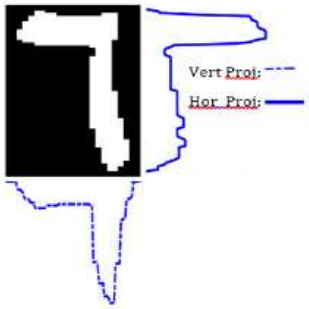

Figure 9. Vertical and Horizontal Projection of Digit "٦".

After extracting both vertical and horizontal projections, the related vectors will be concatenated to generate the hybrid projection vector. Finally, the distance between two hybrid projection vectors X and Y is computed as follows:

$$\mathrm{D}(X,Y) = \sum_{i=0}^{n} abs(x_i - y_i) \qquad (1)$$

Where n is the vector size, and abs is a function to compute the absolute value.

The digit (or city name) having the minimum distance from the target image is considered as the recognition result. The recognition process of the digits, in the current work, can be summarized as the following flowchart:

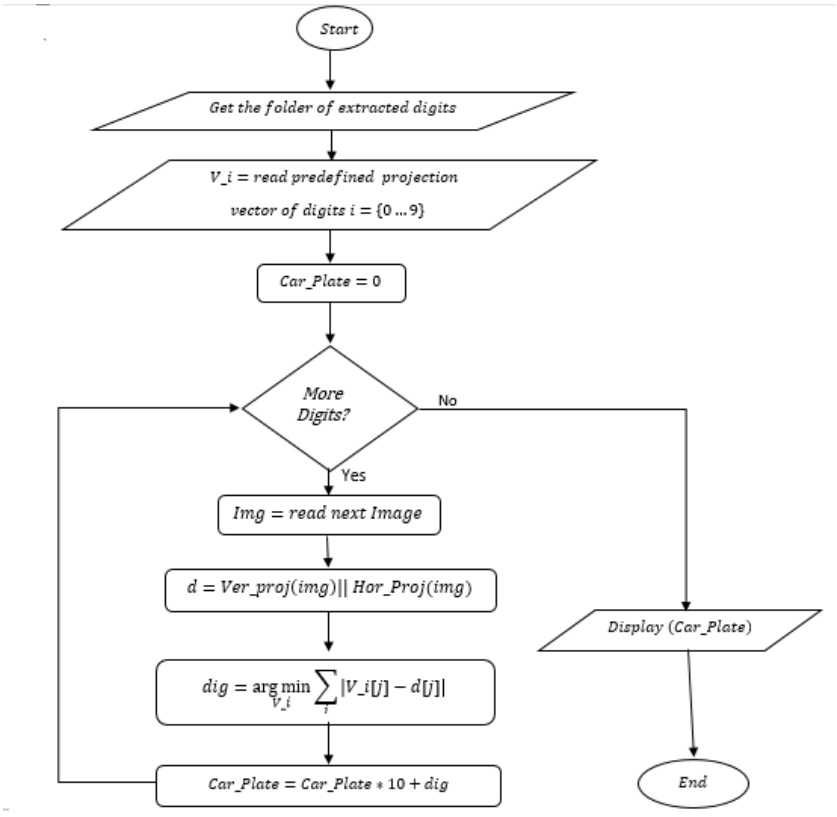

Figure 10. Flowchart Diagram of the Plate Number Recognition.

Almost similar process has been followed for recognizing the city name of the plates in which the horizontal and vertical projections of the city names of the car plates are compared to the reference projections of 3 city names available in the Kurdistan car plates. This will yield the name of the city having most similarity with the projection matrix.

4. Experimental Results

The proposed approach is been implemented in MATLAB and evaluated under various testing scenarios.

4.1. Test Data

There is no standard dataset for the car plates available in the Kurdistan region of Iraq. Therefore, to evaluate the proposed system, the test images have been collected, manually. A digital camera having 12Mega Pixels, dual pixel resolution, f/1.8 aperture and 28mm (wide) have been exploited to take photos of the frontal views of the cars.

The generated dataset includes 200 images which have been categorized into 5 groups, in terms of distance from the camera, view angle, alignment, plate color, and weather condition. The images have been taken in different locations of the region, mainly in Erbil city, and grouped into the following categories (table 1):

Table 1. Categories of the Test Data.

#	Category	No. of Samples	Description
1	Distance of Camera from the Car	45	Images having 1, 2, and 4 meters distance from the camera
2	Car Plate Alignment	60	Car plates have been rotated 0, 45,90 and 180 degree
3	Camera View Points	35	Images are taken from left, right, and frontal views of the car
4	Car Plate Color	30	Car plates having a red, white, or yellow background-color
5	Weather Condition	30	Images have been taken in sunny and heavy rainy weather

Figure 11 depicts some samples of the images used in the current study.

Figure 11. Samples of the Images of the Cars Used for Testing the Proposed System.

4.2. Testing Results

A number of experiments have been conducted on the proposed system to test it under various criteria, precisely. Each category of data is fed to the system separately and the accuracy of the system in terms of both car plate localizing and recognition are computed. Table2. illustrates the percentage accuracy obtained for each testing scenario.

Table 2. The Accuracy of the Proposed System for Different Testing Scenarios.

Scenario / Process	Distance of Camera from the Car S			Car Plate Alignment (Distance=1M)				Camera View points (Distance=1M)			Car Plate Background Color (Distance=1M)			Weather Condition (Distance=1 M)	
	1M	2M	4M	0°	45°	90°	180 °	Left	Right	Front	White	Yellow	Red	Sunny	Rainy
Car Plate Localizing	**94 %**	61 %	27 %	**94 %**	86 %	93 %	86 %	33 %	33%	**94%**	**94%**	**94%**	90 %	**94%**	60%

Car Plate Recognition	**94 %**	61 %	27 %	**94 %**	80 %	86 %	80 %	25 %	33%	**94%**	**94%**	**94%**	70 %	**94%**	50%

As revealed in table2. different testing scenarios have shown different results. The followings are the summary of the results for each scenario:

- For the first scenario, when the car plate is 1 Meter far from the camera, the highest accuracy will be achieved which is 94%, but for the 4-meter distance, the localizing and recognition is not satisfactory at all (27%). The low accuracy rate for longer distances can be due to the presence of other undesired objects in the image. Therefore, for all the other scenarios, the distance of the camera from the car plate is set to be 1 meter.

- Since the SURF descriptor is rotation-invariant, the obtained result for different alignments of the car plate illustrates the same range of accuracy (between 80% and 94%) which is reasonable.

- When the camera viewpoint is changing, the accuracy of the system will change dramatically, from 94% to 25%. These changes are due to the fact that the SURF descriptor is not affine transform insensitive.

- The proposed system produces the same accuracy for both plates having white and yellow backgrounds. But for the red backgrounds plates, the accuracy is slightly lower as the clinching spot on the plate will be considered as foreground and will decline the accuracy.

- Finally, for the rainy situation, the accuracy rate will deteriorate as the raindrops on the image will affect the distinguishing power of the SURF descriptor.

According to the aforementioned discussions, the proposed system has shown the highest accuracy whenever the car plate image is taken from the frontal view having 1-meter distance in sunny weather. Therefore, the system can be used for the controlled area such as the entrance of the security zones and the parking lots.

5. Conclusion

In this paper, we have proposed an Automatic Car Plate Recognition system that works for the cars in the Kurdistan region of Iraq. The system performs car plate localizing using SURF descriptor and recognition using Horizontal/vertical projection. To evaluate the performance of the system, 200 images under various testing scenarios have been prepared and fed to the system. The results show a high accuracy rate, especially for the controlled environments (94%). During the test, we have noticed that the accuracy of the proposed system is directly proportional to the distance of the camera from the car plate which restricts the applications of the system to the specific domains such as parking lots and security zone entrance. Further improvements on the proposed system, as part of the future works, will let the system be employed everywhere with a higher quality of accuracy. Future works need to be done; firstly, improving the algorithm to be able to detect and recognize car plates in real-time rather than working on taken images. Secondly, enabling the approach to function for car plates of the rest of the cities of Iraq as they are existing in KRI such as car plates of Baghdad, Babil, and Wasit. Lastly, making the algorithm handle all kinds of car plates including different fonts, styles of numbers, and positions of numbers and cities on the plate.

References

Abbas, E. I., & Hashim, T. A. (2016). Iraqi Cars License Plate Detection and Recognition System using Edge Detection and Template Matching Correlation. *Engineering and Technology Journal*, *34*(2 Part (A) Engineering), 257-271.

Albiol, A., Sanchis, L., Albiol, A., & Mossi, J. M. (2011). Detection of parked vehicles using spatiotemporal maps. *IEEE Transactions on Intelligent Transportation Systems*, *12*(4), 1277-1291.

Alginahi, Y. M. (2011). Automatic arabic license plate recognition. *International Journal of Computer and Electrical Engineering*, *3*(3), 454-460.

Ali, A. M., Shareef, S. M., & Rashid, T. A. (2015). Automatic License Plate Recognition in Kurdistan Region of Iraq (KRI). *Journal of Zankoi Sulaimani*, Part-A-(Pure and Applied Sciences), 17, 235-244.

Amatya, M. L., & Sarvanan, K. N. (2017). The state of the art–Vehicle Number Plate Identification–a complete Survey. *International Research Journal of Engineering and Technology (IRJET)*, *4*(2), 785-792. Retrieved from https://www.irjet.net/archives/V4/i2/IRJET-V4I2153.pdf

Awaidah, S. M., & Mahmoud, S. A. (2009). A multiple feature/resolution scheme to Arabic (Indian) numerals recognition using hidden Markov models. *Signal Processing*, *89*(6), 1176-1184.

Bay, H., Tuytelaars, T., & Van Gool, L. (2006, May). *Surf: Speeded up robust features*. In European conference on computer vision (pp. 404-417), Berlin, Heidelberg.

Davies, P., Emmott, N., & Ayland, N. (1990, February). *License plate recognition technology for toll violation enforcement*. In IEE Colloquium on Image Analysis for Transport Applications (pp. 7-1). IET. London, UK. Retrieved from https://ieeexplore.ieee.org/document/191012

Draghici, S. (1997). A neural network based artificial vision system for licence plate recognition. *International Journal of Neural Systems*, *8*(01), 113-126.

Ebrahimi, A., Amirkhani, A., A Raie, A., & Mosavi, M. R. (2015). Car license plate recognition using color features of Persian license plates. *Journal of Advances in Computer Research*, *6*(4), 27-38.

He, L., Ren, X., Gao, Q., Zhao, X., Yao, B., & Chao, Y. (2017). The connected-component labeling problem: A review of state-of-the-art algorithms. *Pattern Recognition*, 70, 25-43.

Lotufo, R. A., Morgan, A. D., & Johnson, A. S. (1990, February). *Automatic number-plate recognition*. In IEE Colloquium on Image Analysis for Transport Applications (pp. 6-1). IET. London, UK. Retrieved from https://ieeexplore.ieee.org/document/191011

Massoud, M. A., Sabee, M., Gergais, M., & Bakhit, R. (2013). Automated new license plate recognition in Egypt. *Alexandria Engineering Journal*, *52*(3), 319-326.

Patel, C., Shah, D., & Patel, A. (2013). Automatic number plate recognition system (anpr): A survey. *International Journal of Computer Applications*, *69*(9), 21-33.

Wady, S. H., Ahmad, F. H., & Ahmed, H. O. (2017), Iraqi Kurdistan Vehicle License Plate Recognition System based on Client-server Network. *Journal of Zankoi Sulaimani*, 19 – 1 (Part-A), 251-262. doi: *https://doi.org/10.17656/jzs.10603*

Research Article

Evaluation of Smartphone's Embedded Sensors Through Applications: A Case Study of Gyroscope and Accelerometer

Nian Khidr Aziz[1, a, *], Champion Justin[2, b] and Ibrahim Ismael Hamarash[1, 3, c]

[1] Department of Electrical Engineering, College of Engineering, University of Salahaddin-Erbil, Erbil, KRI, Iraq
[2] Department of Computing, School of Digital, Technologies, and Arts, Staffordshire University, Stoke-on-Trent, UK
[3] Department of Computer Science and Engineering, School of Science and Engineering, University of Kurdistan Hewlêr, Erbil, Iraq

E-mail: [a] nian.khidr@gmail.com, [b] J.J.Champion@staffs.ac.uk, [c] ibrahim.hamad@ukh.edu.krd

Access this article online		
Received on: March 7, 2021	**Accepted on:** September 27, 2021	**Published on:** December 28, 2021
DOI: 10.25079/ukhjse.v5n2y2021.pp10-17	**E-ISSN:** 2520-7792	

Abstract

Smartphones are used for many daily activities like tele-communication, gaming, web browsing, fitness and health monitoring and traditional office working. Smartphones are equipped with built-in sensors to be able to perform these activities. It is well known that the sensors affect the resolution of the smartphone applications which is very vital in life critical applications (LCA). In this paper, two main sensors, the gyroscope and accelerometer have been studied. All commercial smartphones contain these two sensors and support functions related to them. These two sensors have direct link with the physical measurements which feed the fitness and health applications. A fitness application has been selected and ran under Android and iOS operating systems in two different popular smartphones: Samsung Note5 and iPhone7s smartphones. Statistical methodology has been applied to analysis the data and evaluate the performance of the sensors. The results show that commercial smartphones are not reliable devices for motion-related measurements and they can only be used for general purpose monitoring but not in life critical applications.

Keywords: Smartphone, Gyroscope, Accelerometer,IMU, Sensors

1. Introduction

Smartphones are the most widely electronic device used by individuals in the history of mankind. According to the Statista website the number is 3.5 billion devices worldwide in 2020 (Statista, 2020). Smartphones are multi-purposes devises their main function is in telecommunication, while its utility factor is mainly covered by computer gaming, entertainment, Internet browsing and service applications (Hasan & Hamarash, 2017) (Gao *et al.*, 2017) (Banskota, Healy & Goldberg, 2020).

Smartphones are indispensable in everyday life, the numerous application features and flexibility make smartphones an excellent choice for many applications in many different sectors. Every day, new applications are presented in app stores offering new opportunities. Programmers and developers exploit hardware and software features to build their own applications too. Most of these applications use smartphone built-in sensors to add environmental interactions (Belkhamza & Niasin, 2017)(Iyengar *et al.*, 2020)(Nasution *et al.*, 2020). The built-in sensors measure physical quantities to be fed as inputs directly and indirectly providing powerful tools and data for programmers to build their programs and applications.

Gyroscope and accelerometers are among the most used sensors in modern smartphones (Dzeng, Fang & Chen, 2014) (Jain & Kanhangad, 2018).

Gyroscope measures the angular velocity, i.e. the rate of change of the sensor's orientation (Passaro *et al.*, 2017), while accelerometer measures the external force acting on it. The acceleration creates a force that is captured by the force-detection part of the accelerometer. It measures acceleration indirectly through an applied force to the accelerometer's axes. The applied force consists of two components: the sensor's acceleration and the earth's gravity (Dadafshar, 2014).

The mathematical models for gyroscopes and accelerometers are well established in the literature of dynamics, for detail diagrams and formula see (Passaro *et al.*, 2017) and (Dadafshar, 2014). The orientation and force effects of gyroscopes and accelerometers are fused together to determine the motion activities of the smartphone or any touched object (Kok, Hol & Schön, 2017).

Currently, microelectron-mechanical system (MEMS) technology is used in gyroscopes and accelerometers manufacturing. MEMS elements characterized with light, low energy consume, short start-up time and high accuracy (Edinger *et al.*, 2020). These specifications led to raisin the accuracy and resolution of built-in accelerometers and gyroscopes in smartphones. The equipping of smartphones these two sensors have generated opportunities to incorporate motion activity measurements and healthcare systems in smartphone applications (Ogbuabor & La, 2018). In the electronic industry, gyroscopes and accelerometers are packaged together which is then referred to as Inertial Measurement Unit (IMU). All nowadays smartphones are equipped with at least one IMU. Most smartphone built-in IMUs are commercial general purpose without special consideration of accuracy which is required for serious healthcare and fitness applications. This paper studies the accuracy and performance of these two sensors in two popular smartphones to evaluate their adequacy for healthcare applications.

2. Related Works

The embedment of IMU sensors in smartphones brought up opportunities in the industry of mobile applications, especially in Life Critical Systems (LCS), navigation and physical activities. Ma. *et al.* presented a comparison of different types of IMU in (Zhizhong Ma *et al.*, 2013).The comparison shows the relatively high errors in the commercial IMUs in comparison to special designed counterparts.

Built-in IMU sensors in Google Nexus4 smartphone have been evaluated in (Zhizhong Ma *et al.*, 2013). They researchers curried out a test for the characteristics; accuracy, precision, maximum sampling frequency, sampling period jitter, and energy consumption. They found that the gyroscope and accelerometer have small deviations while the compass has a large notable deviation from the real values.

Francisco et. al. (Duarte, Lourenço & Abrantes, 2014) used Artificial Intelligence (AI) to classify physical activities measured by smartphone's accelerometers. The study presented the combination of Android OS with the built-in sensors to found motion features in both frequency and time domains.

Wang et. al. evaluated the best position for the smartphone sensors to be put for motion recognition (Wang *et al.*, 2016). The study concluded that the gyroscopes and accelerometers are able to take the lead roles individually, depending on the type of activity being categorized, the body position, the used data features and the recognition algorithm employed.

Gikas and Perakis presented a study about the accuracy of iPhone5 and HTC One C smartphones to navigation problems. They showed that there is a good consistency between the two devices while there have been differences in the responding to environment conditions (Gikas & Perakis, 2016).

Sunaryono, et. al. studies Android OS-based smartphones from video and image processing perspectives. They determined that phones have advantage over the others, they found that for capturing images Android phones could be used as a tool(Sunaryono, Siswantoro & Anggoro, 2019).

The aforementioned literature shows that there is relatively little systematic research for finding the accuracy of smartphones when they use their built-in gyroscopes and accelerometers in measuring motion activities. The few existence studies show that the measurements accuracy is still an issue point when smartphones are used in life critical systems and serious applications.

In this paper, two very popular smartphones; Samsung Note 5 (Android OS) and iPhone 7 (iOS) have been used to evaluate the accuracy built-in gyroscopes and accelerometers through an application. A simple and straightforward statistical procedure is proposed to evaluate smartphones before using them in serious motion activities. This study uses quality control approach to evaluates the accuracy performance by looking to the device as a black-box; which is the real case from the end-user's perspective.

3. Methodology and Test Setup

Judging the quality of an entity to perform its function adequately according to standards is called evaluation. There are different approaches for evaluation of equipment ranges from complete device testing to comparing manufacturer's datasheets and specifications. The selection of the method depends on the equipment, function and the work conditions. Most evaluation process use statistical quantitative and qualitative measurements to find the final conclusion. In this study, the testing and comparison evaluation method has been selected. The accuracy of the devices under test are evaluated via comparing the results of many tests to individual device itself and to other devices.

Commercially, there are different smartphone brands in the market. Most of them equipped with built-in gyroscopes and accelerometers. They run different operating systems, mostly iOS and Android systems. In this study two popular smartphones from two different manufacturers have been selected. They are: Samsung Note5 and iPhone 7, they run Android 4.3 and iOS 7 operating systems respectively. Both of them are equipped with a separate built-in gyroscope and accelerometer (Jain & Kanhangad, 2018).

The test is carried out by using the two devices in three motion activities; they are: number of steps, distance and speed. The dataset is the output of the devices and the three activities. To maintain constant speed and motion settings, the two smartphones were held by a person walking on a treadmill machine. The two devices are back glued together and put inside the right pocket of the trouser of a person, this arrangement makes the sensors triggering normally, simulate the condition as naturally as possible and finally creates the same exact testing environment for the two devises at the same time.

During the test, three motion activity attributes have been recorded, they are: (1) number of steps, (2) distance, and (3) speed. These activities are measured by the smartphones using three-layer process, starting with reading data from their built-in accelerometer and the gyroscope, then data is captured by the smartphone's operating system and finally the data is converted to the physical quantity values through a an application.

In smartphone industry, the operating system is responsible for data pre-processing and data cleaning. This research does not consider the data pre-processing layer. It uses the final output of the motion activities using Accupedo 3.1. software application for the evaluation process. Accupedo has been selected because it is run in both Samsung Note 5 and iPhone 7. The application has been downloaded from the manufacturer's online store then locally installed before the test is conducted.

Before the recording process, the person's data was recorded as : age = 50, height = 165 cm, weight = 72 kg, and step span = 45 cm. Accupedo has goal variables to be st, they have been set to: speed = 2 km/h, distance = 1 km, and number of steps = 2000 in both smartphones. Each test practiced for 10 minutes and repeated ten times in five separate days, two tests per day. The model of the Treadmill walking machine was YORK Fitness T500. The test settings and configuration are detailed in Table 1, and the test arrangement is shown in Figure 1.

Table 1. Configuration of the Study Case.

Settings	Participant Gendre, age(years), Height (cm), Weight (kg)	Activity	No. of Times Repeated
Study Case	Man, 50,165,72	Walking on Treadmill machine, Model: York T500	10

Figure 1. Test on Treadmill Machine.

4. Analysis of Results

Once the treadmill walking machine starts running and the person starts walking on it, the smartphone built-in sensors trigger, as a result the measurements of the three motion activities begin, the Accupedo visualizes the readings on the screen both online and record them automatically and simultaneously. Figure 2 shows two screenshots during a test. The screenshots include the three motion activities, calories, and the time / date of the test. Table 2 shows the results of walking on a treadmill machine tests for ten repeating times each for 10 minutes.

The software SPSS - Ver. 20 has been used for the analysis of the results. In the analysis, the best suitable statistical method the test sampling, dependency between the variables, and the variable values have been considered. In the experiment, we have two different devices, the tests are curried out for both devices simultaneously and for the same person, this test configuration means that the datasets are strongly tie to each other. Also, the distribution of the readings is not known initially, the true values of the motion activities for any of the smartphones are not known too which means that none of the test results could be selected as control datasets for statistical analysis. Finally, the data is continuous in manner. According to all the above facts regarding the test and the dataset, the best statistical approach for the evaluation is the paired comparison of the two sample data sets to each other.

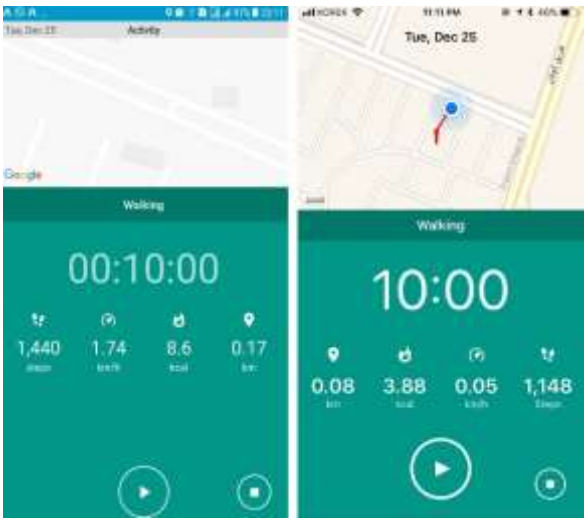

(a) (b)

Figure 2. Screenshots for a) Samsung Note 5, b) iPhone 7.

Table 2. Experimental Results.

Test Number	No. of steps		Distance (m)		Speed (km/h)	
	Note5	***iPhone7***	***Note5***	***iPhone7***	***Note5***	***iPhone7***

1	1492	1177	440	200	2.26	0.28
2	1440	1177	170	800	1.74	0.05
3	1500	1141	900	800	1.44	0.98
4	1551	1141	300	800	0.65	0.98
5	1391	1144	220	750	1.30	0.97
6	1450	1147	400	760	1.60	0.70
7	1436	1141	270	802	1.70	0.88
8	1462	1144	330	790	1.54	0.96
9	1490	1149	450	762	1.45	0.98
10	1462	1141	335	800	1.60	0.89

Continuous data are often summarized by determining their average, minimum, maximum and standard deviation (SD). In the other hand, the paired t-tests are used to compare the means of the two samples of related data. The paired t-test compares the mean difference of the values to zero. It depends on the mean difference, the variability of the differences and the number of data (Seltman, 2018). Two hypotheses have been selected: the null hypothesis and the alternative hypothesis. The null hypothesis has been selected to describe the case that there is no difference between the outputs of the two devices for the same test, while an alternative hypothesis has been selected as the existence of the difference. At the beginning each smartphone has been evaluated individually. The descriptive statistics for each device for the three motion activities (Attributes) have been found. The results are listed in Table 3. The histograms for the three motion activities are given in Figure 3 and 4 for Samsung Note5 and iPhone 7 respectively.

The histograms of Figure 3 and 4 show the data for all motion activities (number of steps, distance and speed) are clustered around a centre however they are not distributed normally. The histogram also shows that there are outliers in the datasets. The descriptive statistics and the histogram show that the two smartphones give different measurement values for the same condition and test.

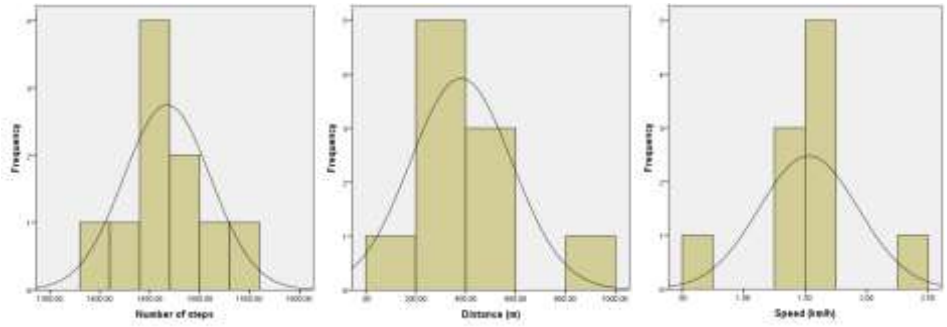

Figure 3. Histogram for Samsung Note 5 Motion Activities.

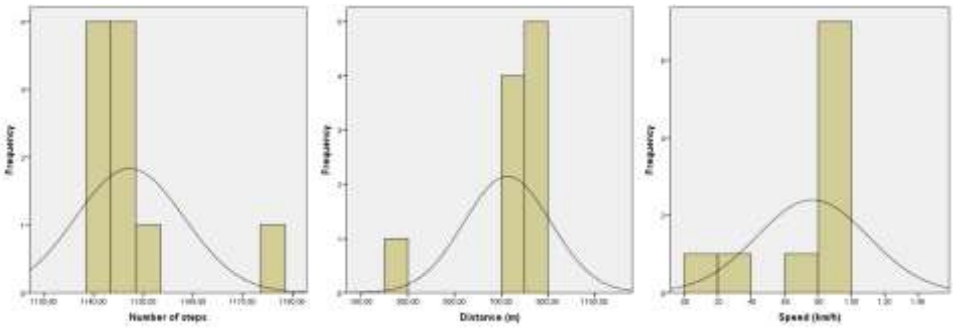

Figure 4. Histogram for iPhone 7 Motion Activities.

Table 3 shows that there are differences between maximum and minimum values for both devices. The ratio between standard deviation to mean is < 0.3 for the number of steps, < 0.5 for the speed and >0.5 for the distance in Samsung

Note 5. The same ratios for the iPhone 7 is <0.01 for the number of steps, < 0.5 for the speed and < 0.3 for the distance. It is clear that the differences are higher in Samsung Note5 than its counterpart in iPhone 7.

Table 3. Descriptive Statistical Analysis.

Parameter	N	Minimum	Maximum	Mean	Std. Dev.
No. of steps (Note5)	10	1391	1551	1467.4	43.59
No. of steps (iPhone7)	10	1141	1177	1147.3	10.88
Distance (m) (Note5)	10	170	900	381.50	203.30
Distance (m) (iPhone7)	10	200	802	726.40	186.03
Speed (km/h) (Note5)	10	.65	2.26	1.5280	.40243
Speed (km/h) (iPhone7)	10	.05	.98	.7670	.33303

The paired t-test is used to compare the means of the readings for the two devices, the t-test determinations are listed in Table 4. Table 4 shows that there are strong evidences (t= 21.401 for number of steps, -5.051 for the distance, 3.524 for the speed) that there are significant differences between the two devices for all motion activities during the same test and condition. The lower and upper limits of the confidence interval 95% shows that we can be 95% confident that the mean difference between the two devices is between 286.26421 and 353.93579 for the number of steps, between 499.36720 and 190.43280 for the distance and between .27245 and 1.24955 for the speed. The p-value (Sig. (2-tailer)) is less than 0.01 for all three motion activities used in the evaluation (see table 4). Therefore, the null hypothesis is rejected with 99% confident and the existence of significant difference between the results of the same test for the same condition is confirmed.

Table 4. SPSS Paired Samples Test.

#	Parameter	Paired Differences					t	df	Sig. (2-tailed)
		Mean	*Std. Deviation*	*Std. Error Mean*	*95% Confidence Interval of the Difference*				
					Lower	*Upper*			
Pair 1	Number of steps (Note5) - Number of steps(iPhone7)	320.10000	47.29917	14.95731	286.26421	353.93579	21.401	9	0.000
Pair 2	Distance (m)(Note5) - Distance (m)(iPhone7)	-344.90000	215.93026	68.28314	-499.36720	-190.43280	-5.051	9	0.001
Pair 3	Speed (km/h)(Note5) - Speed (km/h)(iPhone7)	.76100	.68294	.21597	.27245	1.24955	3.524	9	0.006

5. Conclusions

In this paper, a hypothesis has been set that the smartphones iPhone7 and Samsung Note 5 read accurate motion activities through their built-in gyroscope and accelerometers. To proof the hypothesis, three motion activities have been selected for evaluating the two devices. An application has been used to measure the activities using the data provided by their built-in gyroscopes and accelerometers. The sensor outputs are pre-processed before it is being used by a third party Accupedo software. In our study the two smartphones have been subjected to the exact same test and operating condition. The tests revealed that different smartphones read different results for the same test and the hypothesis is rejected. Results show that there is strong evidence from all activities that the distance, speed and number of steps are changed with the smartphone type and model. Every smartphone gives different reads. Also, there are significant differences between measurements within the same smartphone too. Based on the statistical analysis, we conclude that smartphone motion measurements might be used as guidance only but not in applications which require true measurements like Life Critical Systems (LCS). Smartphones with traditional commercial sensors are not reliable measurement devices for motion activities. The suggestion is that for special measurements, special designed sensors and applications with calibration facilities are required.

References

Banskota, S., Healy, M. & Goldberg, E. M. (2020). 15 smartphone apps for older adults to use while in isolation during the Covid-19 pandemic. *Western Journal of Emergency Medicine*, *21*(3), 514-525. doi: 10.5811/westjem.2020.4.47372.

Belkhamza, Z. & Niasin, M. A. F. (2017). The effect of privacy concerns on smartphone app purchase in Malaysia: Extending the theory of Planned Behavior. *International Journal of Interactive Mobile Technologies*, *11*(5), 178-194. doi: 10.3991/ijim.v11i5.6961.

Dadafshar, M. (2014). Accelerometer and gyroscopes sensors: operation, sensing, and applications. Maxim Integrated. Retrivied from https://www.maximintegrated.com/en/design/technical-documents/app-notes/5/5830.html

Duarte, F., Lourenço, A. & Abrantes, A. (2014). Classification of Physical Activities Using a Smartphone: Evaluation Study Using Multiple Users. *Procedia Technology*, *17*, 239-247 doi: 10.1016/j.protcy.2014.10.234.

Dzeng, R. J., Fang, Y. C. & Chen, I. C. (2014). A feasibility study of using smartphone built-in accelerometers to detect fall portents. *Automation in Construction*, *38*, 74-86. doi: 10.1016/j.autcon.2013.11.004.

Edinger, P. et al. (2020, May). *Compact Low Loss MEMS Phase Shifters for Scalable Field-Programmable Silicon Photonics*. Conference 2020 Conference on Lasers and Electro-Optics (CLEO) (pp. 1-2). IEEE. San Jose, CA, USA. Retrivied from https://ieeexplore.ieee.org/document/9193018

Gao, R. et al. (2017). Smartphone-based real time vehicle tracking in indoor parking structures. *IEEE Transactions on Mobile Computing*, *16*(7), 2023 - 2036. doi: 10.1109/TMC.2017.2684167.

Gikas, V. & Perakis, H. (2016). Rigorous performance evaluation of smartphone GNSS/IMU sensors for ITS applications. *Sensors*, *16*(8):1240. doi: 10.3390/s16081240.

Hasan, D. S. & Hamarash, I. I. (2017). Real time data acquire from multiple Accelerometers and IMU to calculate 3-direction angles and relative orientation. *Zanco for pure and applied sciences*, *29*(2).

Iyengar, K. et al. (2020). COVID-19 and applications of smartphone technology in the current pandemic. *Diabetes and Metabolic Syndrome: Clinical Research and Reviews*, *14*(5), 733-737. doi: 10.1016/j.dsx.2020.05.033.

Jain, A. & Kanhangad, V. (2018). Human Activity Classification in Smartphones Using Accelerometer and Gyroscope Sensors. *IEEE Sensors Journal*, *18*(3), 1169-1177. doi: 10.1109/JSEN.2017.2782492.

Kok, M., Hol, J. D. & Schön, T. B. (2017). Using inertial sensors for position and orientation estimation. *Foundations and Trends in Signal Processing*, *11*, 1-153. doi: 10.1561/2000000094.

Nasution, S. M. et al. (2020). Road information collector using smartphone for measuring road width based on object and lane detection. *International Journal of Interactive Mobile Technologies*, *14*, 42-61. doi: 10.3991/ijim.v14i02.11530.

Ogbuabor, G. & La, R. (2018, February). *Human activity recognition for healthcare using smartphones*. In ACM International Conference Proceeding Series (pp. 41-46). Association for Computing Machinery, New York, NY, United States. doi: 10.1145/3195106.3195157.

Passaro, V. M. N. et al. (2017). Gyroscope technology and applications: A review in the industrial perspective. *Sensors*, *17*(10), 2284. doi: 10.3390/s17102284.

Statista (2020). Retrieved from www.statista.com.

Sunaryono, D., Siswantoro, J. & Anggoro, R. (2019). An android based course attendance system using face recognition. *Journal of King Saud University - Computer and Information Sciences*, *33*(3), 304-312. doi: 10.1016/j.jksuci.2019.01.006.

Wang, A. et al. (2016). A Comparative Study on Human Activity Recognition Using Inertial Sensors in a Smartphone. *IEEE Sensors Journal*, *16*(11), 4566-4578doi: 10.1109/JSEN.2016.2545708.

Zhizhong Ma et al. (2013, June). Experimental evaluation of mobile phone sensors. In *24th IET Irish Signals and Systems Conference (ISSC 2013)*. IET. Letterkenny. doi: 10.1049/ic.2013.0047.

Research Article

Source Identification, Ecological Risk and Spatial Analysis of Heavy Metals Contamination in Agricultural Soils of Tanjaro Area, Kurdistan Region, Iraq

Hayder Mohammed Issa [a,*], Azad H. Alshatteri [b]

Department of Chemistry, College of Science, University of Garmian, Sulaimaniyah, KRI, Iraq

E-mail: [a] hayder.mohammed@garmian.edu.krd, [b] azadalshatteri@garmian.edu.krd

Access this article online		
Received on: March 23, 2021	Accepted on: December 7, 2021	Published on: December 28, 2021
DOI: 10.25079/ukhjse.v5n2y2021.pp18-27	E-ISSN: 2520-7792	

Abstract

The current work accomplished a comprehensive evaluation of heavy metals pollution in soil of agricultural areas from Tanjaro sub-district, Sulaimaniyah province, Kurdistan Region, NE Iraq. Ninety soil samples were collected from thirty different locations. Concentrations of 16 heavy metals were measured by inductively coupled plasma optical emission spectrometry ICP-OES. The pollution index (PI), potential ecological risk index (Er), enrichment factor (EF), and ecological risk index (RI) were used to assess the pollution in soil samples. High levels of Li and Ni, and moderate Ba, Cd, Hg, and Pb according to the results of concentration analysis, pollution index (PI), and potential ecological risk (ERI). High levels of Cd and Hg according to the results of Er. Agglomerative hierarchical clustering (AHC) and principal component analysis (PCA) suggested that heavy metals were generated from different natural and anthropogenic sources like natural weathering, fertilizer application, and transportation. Origins of Hg, Cd, Ni, and Pb are probably from activities like overuse of pesticides and fertilizers, whereas Pb could be exhausted from vehicle exhausts as well. Furthermore, spatial distributions revealed nonpoint source pollution for the studied heavy metals. The obtained results help in the remediation techniques of contaminated soils such as dilution with decontaminated soil or extraction or separation of heavy metals.

Keywords: Heavy Metals Source, Ecological Risk Assessment, Soil Pollution, GIS, Kurdistan Region, Heavy Metals.

1. Introduction

Contamination by heavy metals in soils is greatly considered to be harmful. It is not limited to the lithosphere, but it may spread to other components of the earth system such as the atmosphere, hydrosphere, and biosphere (Haciyakupoglu *et al.*, 2015). Fundamentally for agricultural soils, it is worthy of mention that anthropogenic activities, especially pesticides and fertilizers implementation and irrigation with wastewater, have a major action in increasing heavy metal levels in such soils (Doabi *et al.*, 2018). It is not only the nonbiodegradability nature of heavy metals that make them highly poisonous and dangerous, but also their tendency to accumulate in biomass causing harmful consequences (Kim *et al.,* 2015). Moreover, heavy metal accumulation in cultivated soils has a high possibility of passing into the food chain of humans, animals, and plants, as well as deterioration of land crop productivity (Hu *et al.,* 2018).

It has been observed heavy metals contamination in farmed soils is mainly related to anthropogenic activities (da Silva *et al.*, 2017). However, heavy metal levels in agricultural areas are, in general, lower than that of urbanized areas (Teng *et al.*, 2014).

Even though it is complicated to assess correctly heavy metals contamination correctly, it can be observed various analytical statistics and pollution indices have been applied successfully in issues related to heavy metals pollution in

agricultural soils. Ecological risk index, pollution index, and many other pollution indices are widely considered to be reliable in related issues (Kowalska *et al.*, 2018). Multivariate methods and enrichment factors are usually used to find the origins of heavy metals for studied soil (Pan *et al.*, 2016).

Tanjaro sub-district is one of the main agricultural areas in the north of Iraq and it produces a variety of fruits and vegetables. Limited studies were conducted on the contamination in agricultural soil of Tanjaro sub-district among the studies that have been made to assess heavy metals pollution in rural and agricultural soil in Iraq. Studies on heavy metals in agricultural soils for the area are practically not existing.

The objective of the current study is to conduct a comprehensive environmental evaluation of heavy metals contamination in agricultural soils of Tanjaro sub-district, Sulaimaniyah province, Kurdistan region, Iraq. At present, the study area is a considerably important area for crop production in the north of Iraq. This study also identifies the sources of heavy metals using various assessment indices, and statistical analysis. Moreover, this study tries to explore heavy metals concentrations in the area and to determine its sources, natural or anthropogenic, to protect the life and health of people in this region.

2. Materials and Methods

2.1. The Study Area

The study area of Tanjaro sub-district of 600 km^2 (35° 15' N, 45° 0' E, 35° 35' N, 45° 50' E) is in northern part of Iraq, Arbat city is the center of the sub-district, and it is about 27 km southeast of Sulaimaniyah city. The climate of the area is similar to Sulaimaniyah city, the average annual rainfall in the sub-district is ranging mean annual precipitation is 703.7 mm, average annual air temperature is 19° C with slight precipitation in the summer season (Ahmad & Mustafa, 2008). The area is comprising of plains, hilly, and mountainous areas, the soil is mainly comprised of Quaternary alluvial sediments (Sürücü *et al.*, 2019).

2.2. Soil Samples

In the current study, 90 soil samples have been collected from three depths of 0, 10, and 20 cm for 30 locations within agricultural soils in Tanjaro sub-district for June to July 2019. The sampling sites (S1 to S30), are at least 200 m from the main roads as recommended by previous works (Liu *et al.*, 2015), represent the cultivated soils in Tanjaro area (see Figure 1). Each soil sample is a composite sample composed from the three depths samples. Then samples have been stored closed cup plastic containers and carried to the laboratory of instrumental analytical chemistry (University of Garmian) for analysis.

2.3. Chemical Analysis

Format chemical analysis was performed to quantify the content for the metals of Hg, Al, Cd, As, Ba, Co, Cu, Cr, Fe, Pb, Li, Mn, Ni, Sr, Zn and V in each sample using inductively coupled plasma optical emission spectroscopy ICP-OES. The ICP-OES (Spectro Across, made in Germany) instrumental conditions were consisting of conventional sample preparing procedure using different dilutions using 0.5% nitric acid (pH < 2). A procedure of wet digestion was followed for soil sample analysis (Amjadian *et al.*, 2016). In the analysis, always distilled deionized water and glassware washing were used for the dilutions.

2.4. Evaluation Methods

The performance of the heavy metals concentration analysis method by using ICP-OES was evaluated and confirmed according to the device limits of detection and quantification. The performance assessment was made by analyzing a known quality control standard after each 10 samples analysis (Al-Wabel *et al.*, 2017). The reproducibility of ICP-OES measurements has been verified by 3 repeats of samples taken from each sample location.

2.5. Statistics

Different descriptive and inferential statistics were implemented for analysis of the collected soil samples such as ANOVA, Pearson correlation (PC), principal component analysis (PCA), and cluster analysis (CA). A one-way ANOVA method was used to evaluate the significant variance between sample locations at 95 % level of confidence. Multivariate statistics are usually performed to discover the implied relationships among the heavy metals (Hou *et al.*, 2017). For this reason, PCA is a well-known method to define such relationships, whilst, PCA and CA are used in environmental and risk assessments. CA helps to categorize investigated heavy metals into main categories with individual and distinguishing impacts on the observations (Kaur *et al.*, 2018). PCA distributes the data on several independent factors named principal components. This method displays the loading weight of principle components on the dataset, and the

significance of variables on each principal component. The statistics of multivariate analysis were implemented using the XLSTAT add-in, 2014 for Excel 2016.

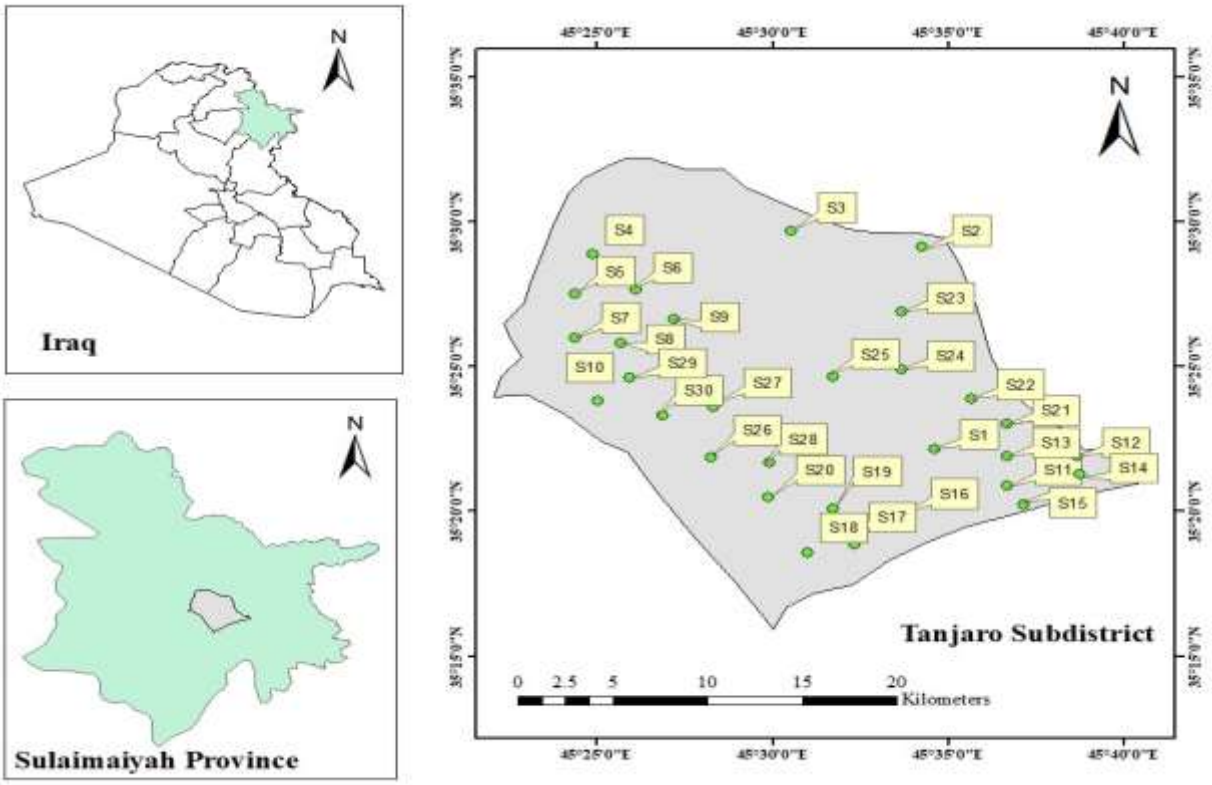

Figure 1. The Tanjaro Area Illustrating Soil Sample Sites.

2.6. Evaluation Parameters

2.6.1. Factor of Heavy Metals Enrichment

Factor of heavy metals enrichment (EF) is a factor defines soil contamination mostly happened by heavy metals and could be implemented to explore the level of anthropogenic impact in the contamination. EF is considered for each heavy metal as a function of a background heavy metal (Baltas *et al.*, 2020). In the current study, Fe has been chosen as a reference for heavy metal. The following EF equation was used.

$$EF = \frac{[\frac{C_i}{C_{ref}}]_{sample}}{[\frac{C_i}{C_{ref}}]_{background}} \quad (1)$$

C_i refers to a measured level of concentration in (mg kg^{-1}) in each sample, C_{ref} is the reference metal concentration (see Table 1) of the same heavy metal (mg kg^{-1}). The subscripts signifying the soil sample and reference values respectively.

EF can be classified into 7 main levels: starts with clean enrichment situation of EF less than 1; slight situation of EF between 1 and 3; moderate situation of EF between 3 and 5; moderate to acute situation of EF between 5 and 10; acute situation of EF between 10 and 25; very critical situation of EF between 25 and 50; extremely acute situation of EF greater than 50 (Esmaeilzadeh *et al.*, 2019). The EF value greater than 1 means anthropogenic sources, while EF less than 1 indicates a natural source for heavy metals (Luo *et al.*, 2015).

Table 1. Illustrative Statistical Analysis of Metal Concentrations (mg/kg - on Dry Weight).

Parameter	Minimum	Maximum	Mean	Standard Deviation	BV	ASV[e]	SGV[f]
Mercury	0.21	0.65	0.48	0.12	0.5[a]	0.056	6.6
Aluminum	3674.0	5003.0	4216.56	325.16	71000[c]	77440	--
Cadmium	0.39	0.60	0.50	0.06	0.35[c]	0.102	1.4

Arsenic	1.05	2.10	1.48	0.31	5[a]	2.0	12
Barium	48.32	72.43	58.07	5.51	62[b]	668	--
Cobalt	2.32	2.76	2.53	0.14	8[c]	11.6	40
Copper	3.12	3.57	3.33	0.14	15[c]	14.3	63
Chromium	10.15	12.95	11.66	0.82	70[c]	35	64
Iron	3365.0	4287.15	3912.54	235.11	4000[e]	30890	--
Lead	5.30	6.30	5.93	0.29	12[c]	17	70
Lithium	29.7	34.65	31.82	1.50	11[b]	22	--
Manganese	109.4	127.80	119.45	4.18	455[b]	527	--
Nickel	18.30	22.95	20.79	1.44	5[c]	18.6	50
Strontium	109.3	126.10	117.07	4.95	175[d]	316	--
Zinc	18.32	29.50	22.51	3.19	60[c]	52	200
Vanadium	8.00	9.75	8.83	0.51	100[a]	53	130
pH*	7.25	7.86	7.46	0.16	--	--	--

BV Background Values; ASV Average Shale Values; SGV Soil Guideline Values; [a] adapted from (Tóth *et al.,* 2016); [b] adapted from (Reimann *et al.*, 2018); [c] adapted from (UNEP, 2013); [d] adapted from (Kabata-Pendias, 2010); [e] adapted from (Wedepohl, 1995); [f] adapted from (Canadian Council of Ministers of the Environment (CCME), 2007); * unit is pH degree.

2.6.2. Index of Pollution

Index of pollution, IP, is employed to evaluate heavy metals contamination in soil that is generated from various sources (Simon *et al.*, 2013). IP is a factor of concentration ratios of the concerned metal and a reference metal. IP has 3 groupings (Sun *et al.*, 2010): a low level of pollution of IP equals or less than 1; mild level of pollution of IP between a and 3; and finally a severe condition of pollution of IP greater than 3.

$$PI = \frac{C_i}{S_i} \quad (2)$$

C_i is metal concentration (mg kg-1) in each sample, and S_i is the reference metal concentration (mg kg^{-1}) of metal (See Table 1).

2.6.3. Index of Ecological Risk

Index of ecological risk RI index was originally established by Hakanson (1980) in order to identify the ecological risk of metals in water modes. Then the index was effectively used for agricultural soil contamination in rural areas (Keshavarzi & Kumar, 2019). This index can associate the potential risk of metals and ecological effects (Trujillo-González *et al.*, 2016), RI equation is as follows

$$RI = \sum_{1}^{n} Er^i \quad (3)$$

$$Er^i = Tr^i * C_f^i \quad (4)$$

$$C_f^i = \frac{C_{o\text{-}i}^i}{C_n^i} \quad (5)$$

C^i_f is pollution parameter, $C^i_{o\text{-}i}$ is metal concentration in the sample (mg kg^{-1}), C_n is reference concentration (mg kg^{-1}), Er^i is the potential index of ecological risk, finally and Tr^i is the toxicity response factor adapted from Zheng-Qi *et al.* (2008). Both RI and Er^i have acquired with eliminating Ba, Al, Fe, and Li since the values of Tr^i are not established in the literature. Ecological risk index is classified into 4 groups: slight risk of RI less than_150; mild risk of RI between 150 and 300; significant risk of RI between 300 and 600; Ultimate considerable risk of RI greater than 600. Likewise, the potential Er was categorized into 4 ranges that are based on Er^i values: less than 40 (clean or light pollution); 40 - 80 (moderate pollution); 80 - 160 (significant pollution); 160 - 320 (extreme pollution).

2.7. Spatio-statistical Analysis

The spatio-statistical analysis is mainly applied using geospatial tools of ArcGIS (version 10.7) was used to determine the sources and pollution intensities of the metals. Like previous works (Ogunkunle & Fatoba, 2014), ArcGIS (IDW interpolation) has been performed to identify the geo-distribution of heavy metals concentration.

3. Results

3.1. Concentrations of Heavy Metal

The illustrative statistical analysis of metal concentrations in concerned samples is presented in Table 1, in which, concentrations of Hg, Al, Cd, As, Ba, Co, Cu, Cr, Fe, Pb, Li, Mn, Ni, Sr, Zn and V were identified. Different

reference values have been employed as illustrated in Table 1 to evaluate the measured concentrations. For example, the maximum concentrations for some heavy metals like Co, Cu, Pb, and V are below the limit of reference values. While, the mean, and maximum values of Cd and Ni exceed the maximum allowable limit of BV, meaning that majority of the sampling sites are polluted by these two metals. For example, the Cd concentration distribution shows the mean and maximum values in soil samples (0.60 and 0.50 mg kg^{-1} respectively) are greater than the reference BV of 0.35 mg kg^{-1}.

3.2. Contamination Assessment

Table 2 shows the contamination levels for studied evaluation factors RI, EF, Er and IP, Er in the studied samples. The EF ranges from no enrichment with the minimum value of aluminum (EF = 0.08) to medium enrichment of nickel Ni (EF is 4.29). The EF mean values for the rest are at minimum. From Table 2, IP values show high pollution rages regarding Ni and Li and moderately polluted regarding investigated metals Pb, Ba, Cd, and Hg. According to IP, minimal ranges were observed for the rest. IP mean values of the tested metals at the thirty sites are ranging from 0.12 to 6.78 of Al and Ni respectively. In general, IP values demonstrate that the soil can be considered reasonably contaminated.

According to EF and PI, the study area is polluted by several heavy metals more than the remaining tested metals. Up to a point, a convergence between the results of EF and Er can be observed (See Table 2). Nevertheless, the outcomes of the potential Er are generally acceptable, mean values range from 0.28 to 81.19 of V and Cd respectively. Er values are demonstrating a high accumulation of the heavy metals of Cd and Hg. Hg displays a different behavior for lower Er mean values of 60.37, which is under 80, referring that Hg is measured at a moderate range. Whilst, the Tr^i value is high-level of 40, the region is ranked to be highly polluted by Hg. As a final point, RI index is 192.36 for the studied soils. This results for such area indicates that the ecological risk condition is moderately polluted.

Table 2. Contamination Levels by Heavy Metals Using Er, EF, and IP Indices.

Parameter	EF			IP			Er		
	Average value	St. Dev.	Condition	Average value	St. Dev.	Condition	Average value	St. Dev.	Condition
Aluminum	0.08	0.01	No enrichment	0.12	0.01	Minor	-		
Arsenic	0.27	0.03	No enrichment	0.43	0.05	Minor	4.31	0.49	Minor
Barium	1.42	0.22	Minor	2.24	0.33	Considerable	-		
Cadmium	1.72	0.20	Minor	2.71	0.26	Considerable	81.19	7.85	Maximal
Cobalt	0.34	0.03	No enrichment	0.53	0.04	Minor	2.66	0.20	Minor
Chromium	0.17	0.01	No enrichment	0.27	0.02	Minor	0.54	0.04	Minor
Copper	0.25	0.02	No enrichment	0.40	0.02	Minor	2.01	0.12	Minor
Iron	-	-	-	1.58	0.09	Considerable	-		
Mercury	1.00	0.24	Minor	1.51	0.37	Considerable	60.37	14.86	Considerable *
Lithium	2.66	0.22	Minor	4.20	0.27	Maximal	-		
Manganese	0.22	0.02	No enrichment	0.35	0.03	Minor	0.71	0.06	Minor
Nickel	4.29	0.31	Considerable	6.78	0.33	Maximal	33.88	1.66	Minor
Lead	0.66	0.05	No enrichment	1.04	0.06	Considerable	5.20	0.29	Minor
Strontium	0.37	0.06	No enrichment	0.59	0.10	Minor	-		
Vanadium	0.09	0.01	No enrichment	0.14	0.01	Minor	0.28	0.02	Minor
Zinc	0.38	0.04	No enrichment	0.61	0.04	Minor	1.21	0.09	Minor

***** is measured as considerable as it is closer to the minimum limit of the considerable level and has a high Tr value.

3.3. Multivariate Statistical Analysis

The outcomes interprets the heavy metals are meaningfully varying with p value less than 0.05. The p value is zero while the F-value is 3754.56, and $F_{critical}$ is 1.689, meaning that a spatial significant divergence exists among the soil sets. One-way analysis of variance (ANOVA) was the method that used to reach this result.

Correlation analysis was achieved in this work as presented in Table 3 to define the relationships among the heavy metals in the area. Therefore Table 3 shows the correlation matrix between the considered heavy metals.

The correlations at p value less than 0.05 for the heavy metals, it is worth mentioning, as indicated in Table 3 positive and negative considerable relationships, higher than 0.3, are existing. The highest positive significant correlations between Ba with Co and Pb were observed. Negative considerable correlation Al with Cu, As with Cu, Ba with V, Ni with Sr, Co with Zn, and V with Zn were noticed as examples.

To gain further insight into the relationships among the remaining heavy metals, CA has been accomplished. CA (with Ward method and Euclidean measuring for similarity) is applied to search for sources of heavy metals and also to reorder the dataset into several main groups.

In Figure 2 significant correlations were observed between Pb and Ba, and Co and Cr, they were related to form a cluster. Cu and Ni showed a significant correlation between them, they were connected at later stages with Cd, Hg, and Mn. A third cluster was established for As, Li, and Zu as they lack significant relationships with the remaining heavy metals in soil samples.

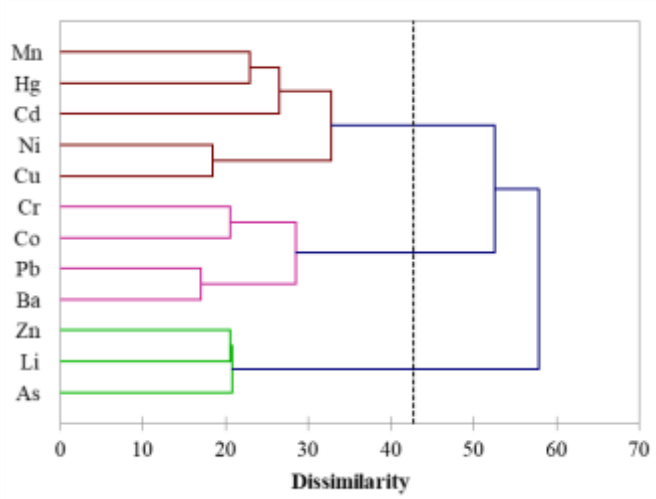

Figure 2. Significant Dissimilarity Relations Among Metals Obtained by CA.

Table 3. Correlation Coefficients Between Tested Metals in Tanjaro Soils.

	Mercury	Aluminium	Cadmium	Arsenic	Barium	Cobalt	Copper	Chromium	Iron	Lead	Lithium	Manganese	Nickel	Strontium	Zinc	Vanadium
Mercury	1															
Aluminium	-0.11	1														
Cadmium	0.10	0.07	1													
Arsenic	-0.28	-0.03	-0.13	1												
Barium	-0.04	-0.04	0.04	0.01	1											
Cobalt	0.03	0.18	0.24	-0.09	0.41	1										
Copper	0.11	-0.40	0.07	-0.43	-0.08	-0.15	1									
Chromium	-0.21	0.17	-0.19	-0.10	0.10	0.29	-0.34	1								
Iron	0.10	-0.25	-0.08	0.10	0.01	0.13	0.00	0.17	1							
Lead	0.29	-0.02	0.18	-0.11	0.41	0.15	0.04	0.08	0.13	1						
Lithium	0.29	0.14	0.05	0.29	-0.08	-0.09	-0.49	-0.03	0.03	-0.09	1					
Manganese	0.21	0.01	0.14	-0.44	0.01	-0.03	0.31	0.17	0.20	0.21	-0.19	1				
Nickel	-0.01	-0.22	-0.11	0.28	-0.03	-0.27	0.36	-0.46	0.09	-0.19	0.07	0.14	1			
Strontium	-0.14	-0.30	-0.05	-0.15	0.16	0.34	0.11	0.31	0.26	0.20	-0.32	0.00	-0.40	1		
Zinc	-0.01	-0.40	-0.22	0.28	0.03	-0.43	-0.12	-0.13	0.00	0.09	0.29	-0.27	0.19	-0.29	1	
Vanadium	-0.12	0.17	-0.11	-0.11	-0.42	-0.01	0.21	-0.0	0.24	-0.47	0.03	-0.12	-0.03	0.14	-0.47	1

* Correlations at significance level 0.05

PCA was applied to figure out the variance of trace metals levels and identify their origins. High scores of eigenvalues are set to be weightier. Varimax rotation with Kaiser Normalization were employed to improve the heavy metals loading and eigenvalue of the sixth factor was achieved after the rotation. Results show that six factor might be the more significant in representing of 80.1% of the results for tested metals difference.

By performing PCA, the dataset was reduced to six main components representing 80.1% of heavy metals concentrations variance. Table 4 shows that six rotated way with eigenvalues more than one that have been extracted. PC1 represents 20.60% of dataset variance, exhibits strong positive loading on Li and strong negative loading on Cu, with a moderate positive loading on As. PC2, which explains 18.00% of dataset variance, is significantly correlated with Cd and Cr, with moderate loading on Hg. This factor agrees with EF results of Cd and Hg, they are 1.72 and 1.00 respectively. PC3, accounting for 13.11% of dataset variance, has strong positive loading on Mn and Hg, with significant negative loading on As. PC4, that refers to 10.92% of dataset variance, exhibits strong loadings to Ba with Pb. PC5, which represents 10.07% of dataset variance, exhibits strong impact of Co with a significant Zn negative with moderate impact of Cd. PC6 accounts for 7.39% of dataset variability, is dominated by Ni.

Table 4. Total Variance for PCA Factors.

Comp.	Initial eigenvalues			Extracted sums for squared loading			Rotation sums of squared loadings		
	Eigenvalue	Variability (%)	Cumulative %	Eigenvalue	Variability (%)	Cumulative %	Eigenvalue	Variability (%)	Cumulative %
F1	2.47	20.60	20.60	2.47	20.60	20.60	1.75	14.61	14.61
F2	2.16	18.00	38.60	2.16	18.00	38.60	1.38	11.46	26.07
F3	1.57	13.11	51.71	1.57	13.11	51.71	1.78	14.90	40.97
F4	1.31	10.92	62.63	1.31	10.92	62.63	1.58	13.20	54.17
F5	1.21	10.07	72.70	1.21	10.07	72.70	1.68	13.98	68.14
F6	0.89	7.39	80.09	0.89	7.39	80.09	1.44	11.95	80.09
F7	0.78	6.47	86.56						
F8	0.55	4.60	91.16						
F9	0.40	3.33	94.50						
F10	0.28	2.31	96.81						
F11	0.22	1.86	98.67						
F12	0.16	1.33	100.00						

Parameter	Loading values						Rotated loading values					
	PC1	**PC2**	**PC3**	**PC4**	**PC5**	**PC6**	**PC1**	**PC2**	**PC3**	**PC4**	**PC5**	**PC6**
Arsenic	0.72	-0.26	0.04	0.31	0.21	0.19	0.43	-0.05	-0.65	0.05	-0.12	0.36
Barium	-0.28	-0.36	0.33	0.68	-0.08	0.14	-0.03	-0.10	-0.12	0.86	0.19	0.11
Cadmium	-0.36	0.00	0.34	-0.07	0.62	-0.17	0.05	0.64	0.10	0.10	0.46	-0.12
Cobalt	-0.50	-0.55	0.03	0.19	0.39	0.17	0.08	-0.02	-0.09	0.38	0.76	-0.16
Chromium	-0.26	-0.63	-0.33	-0.16	-0.43	0.25	0.12	-0.78	0.09	0.10	0.24	-0.38
Copper	-0.38	0.79	-0.10	0.22	-0.01	-0.12	-0.73	0.30	0.34	-0.05	-0.09	0.29
Mercury	-0.23	0.21	0.69	-0.42	-0.07	0.04	0.33	0.39	0.67	0.11	-0.12	-0.09
Lithium	0.49	-0.26	0.53	-0.43	0.10	0.28	0.90	0.11	0.05	-0.09	-0.13	0.07
Manganese	-0.58	0.34	0.05	-0.15	-0.28	0.52	-0.18	-0.24	0.79	0.06	0.20	0.25
Nickel	0.35	0.63	0.10	0.35	0.14	0.51	-0.04	0.12	0.02	-0.06	-0.17	0.94
Lead	-0.41	-0.15	0.59	0.31	-0.34	-0.18	-0.03	0.12	0.29	0.78	-0.14	-0.23
Zinc	0.61	0.07	0.34	0.17	-0.45	-0.23	0.22	0.01	-0.20	0.20	-0.80	0.07

3.4. Spatial Exploration

Figure 3 illustrates the spatial spreading of some important heavy metals of barium, cadmium, mercury, cobalt, lithium, nickel and lead within Tanjaro sub-district. The distribution of investigated metals agrees with statistical and environmental contamination assessments, indicating that these heavy metals originated from natural and anthropogenic sources. In Figure 3 shows high concentrations of nickel in most of the studied soils.

4. Discussion

The results presented in Table 1 reveal potential significant impacts of Al, Ba, Cd, Fe, Ni, and Pb could exist in crops in the study area. Since Ba chemistry is relatively similar to Ca, Ba does not tend to accumulate in living creatures (Adriano, 2001), therefore they could be overlooked. Naturally, Al and Fe appear at abundant levels of the crust, they are free from anthropogenic impact, and thus their high concentrations would be barely considerable. Whilst, high levels of Pb, Ni, Cd, and Hg high concentrations in the studied area reveal more influence of these metals in the reduction of agricultural soil quality with higher potential pollution risk.

From these findings shown in Table 2, it is evident the studied soils are considerably polluted by Ba, Cd, Hg, Li, and Ni, as their mean EF value is equal or/and greater than 1. Origins of Hg, Ni, and Cd were probably industrial actions, however, EF of a value lower than 1 suggests natural sources for the remaining. From Table 2, in general, IP values demonstrate that a moderate pollution. According to EF and IP, the pollution is mainly caused by certain metals. Er levels are suggesting that an ecological risk can be generated due to the accumulation of Hg and Cd, as significant levels are counted to these metals.

CM results of positive correlations propose the origin of tested metals like V or Sr is most probably is the natural composition of studied soils, by means of no important correlations were observed for Hg or any well-known heavy metal from anthropogenic sources, and no anthropogenic activity in the area would contribute to their occurrence.

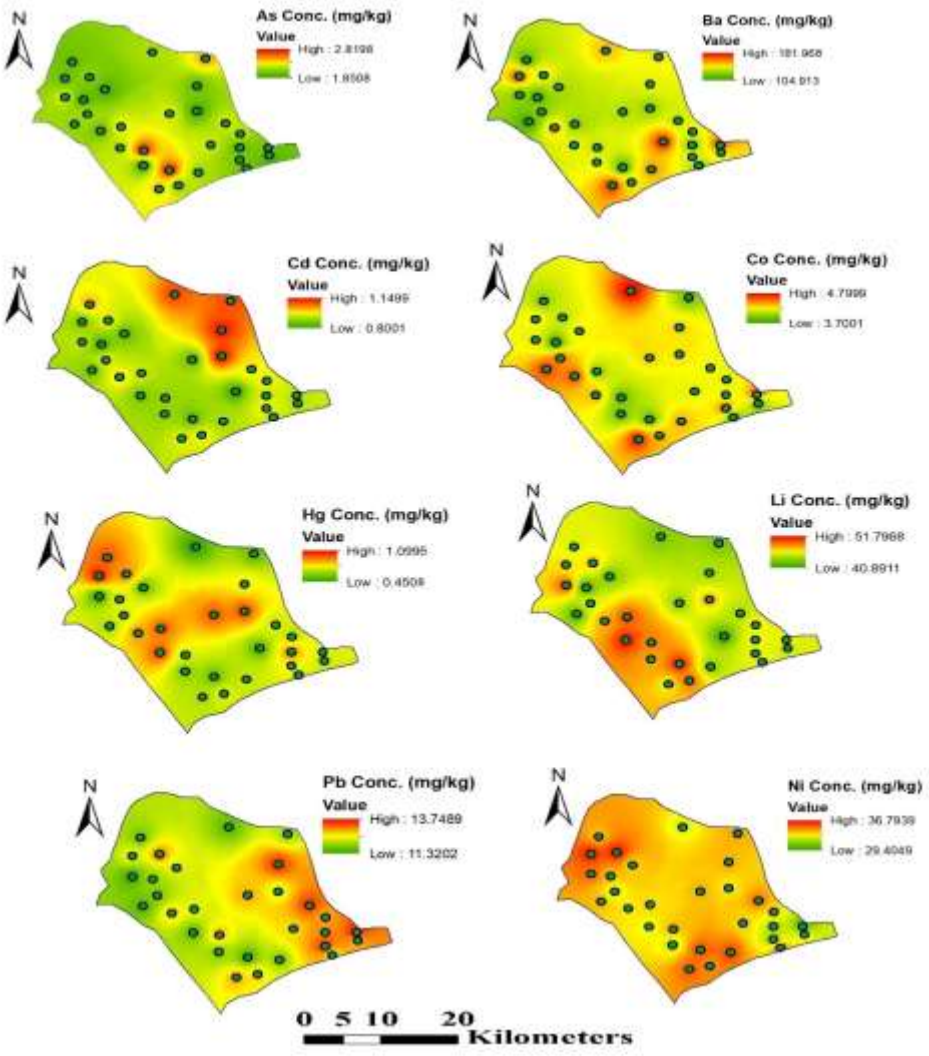

Figure 3. Distribution of Certain Heavy Metals Concentrations in Tanjaro Sub-District.

Significant correlations of Ba with Co and Pb suggest that they have originated most likely because of intensive using of pesticides or fertilizers in the area.

According to AHC analysis, the origin of examined metals in agricultural soil is categorized into three classes. The last cluster of As, Li, and Zn is probably the one that was originated from natural origins in the studied soils. EF values are less than 1 for As and Zn indicating that the area is not contaminated by them.

From PCA analysis, PC1is suggesting that heavy metals Li, Cu, and As have originated from natural sources. EF values of Cu and As in the studied soils are under 1, indicating no enrichment in the soil, and subsequently, their sources are likely to be natural. Although EF values of Li are higher than 1, the source of Li is wholly natural, weathering of parent materials as no known anthropogenic activity originates Li in the area. PC2 is highly correlated to Cd and Cr, with moderate loading on Hg. Based on EF results, the level of Hg and Cd are 1.00 and 1.72 respectively, PC2 suggests anthropogenic sources of these metals, whereas the level of EF for Cr is 0.17, indicating no enrichment levels of soil samples. Compared to Cr background value, Cr concentrations in soil samples are much lower, indicating that Cr concentrations were affected by anthropogenic activities. PC3 of strong loading on Mn and Hg, with significant negative loading on As, signifying origin of these metals comes from mixed sources of natural and anthropogenic. The anthropogenic activities that release As and Hg in agricultural soils are mainly fertilizer and pesticide applications. Mn concentrations in soils, which are mainly controlled by natural sources (Gong *et al.*, 2010), seem to be associated with natural sources (the composition of rocks and soil) in the study area. PC4 is suggesting inputs of Ba and Pb, from anthropogenic activities such as the implementation of fertilizers. Another anthropogenic origin of Pb is atmospheric

deposition from exhausts of vehicles. PC5 suggests mixed lithogenic and anthropogenic sources of Co, Zn, and Cd, similar factor loading was reported by (Huang *et al.*, 2015) for these heavy metals. The component PC6 of Ni is an anthropogenic one with an EF value equals 4.29, indicating a moderate enrichment of soil samples. Excessive Fertilizer applications are usually causing high Ni levels in agricultural soils (Cai *et al.*, 2015). Figure 3 displays an extreme application of manures and pesticides impact in the study area (Zhong *et al.*, 2016).

5. Conclusion

Considerable contamination concentrations of both Ni and Li, and moderate pollution levels for Ba, Cd, Hg, and Pb have been indicated by the results of concentration analysis and PI. ERI results considered Cd, Hg, and Ni at moderate to high ecological risk levels, respectively. CA, PCA and EF show that there are 3 separate origins of examined heavy metals; natural, anthropogenic and mixed contributions. Most anthropogenic contributions were for Hg, Cd, Pb, and Ni. The distribution map showed generally that non-point pollution sources in soils. The valuations and investigation established in the current work will enhance the implication of statistical multivariate and ecological risk analysis as a reliable method for the assessment of heavy metals contamination in agricultural soils for the remaining parts of Kurdistan Region.

Acknowledgment

We thank University of Garmian for providing the necessary laboratories and facilities to achieve the experimental part of this work.

References

Adriano, D. C. (2001). *Trace elements in terrestrial environments: biogeochemistry, bioavailability and risks of metals* (n. edn. Ed.). New York: Springer.

Ahmad, H. S., & Mustafa, O. M. (2008). Nitrate Pollution in Groundwater of Sulaimaniyah City, Kurdistan Region, NE Iraq. *Iraqi Bulletin of Geology and Mining, 4*(2), 73-82.

Al-Wabel, M. I., Sallam, A. E.-A. S., Usman, A. R. A., Ahmad, M., El-Naggar, A. H., El-Saeid, M. H., *et al.* (2017). Trace metal levels, sources, and ecological risk assessment in a densely agricultural area from Saudi Arabia. *Environmental Monitoring and Assessment, 189*(6), 252.

Amjadian, K., Sacchi, E., & Rastegari Mehr, M. (2016). Heavy metals (HMs) and polycyclic aromatic hydrocarbons (PAHs) in soils of different land uses in Erbil metropolis, Kurdistan Region, Iraq. *Environmental Monitoring and Assessment, 188*(11), 605.

Baltas, H., Sirin, M., Gökbayrak, E., & Ozcelik, A. E. (2020). A case study on pollution and a human health risk assessment of heavy metals in agricultural soils around Sinop province, Turkey. *Chemosphere, 241*, 125015.

Cai, L., Xu, Z., Bao, P., He, M., Dou, L., Chen, L., *et al.* (2015). Multivariate and geostatistical analyses of the spatial distribution and source of arsenic and heavy metals in the agricultural soils in Shunde, Southeast China. *Journal of Geochemical Exploration, 148*, 189-195.

Canadian Council of Ministers of the Environment (CCME). (2007). Canadian soil quality guidelines for the protection of environmental and human health.

Esmaeilzadeh, M., Jaafari, J., Mohammadi, A. A., Panahandeh, M., Javid, A. & Javan, S. (2019). Investigation of the extent of contamination of heavy metals in agricultural soil using statistical analyses and contamination indices. *Human and Ecological Risk Assessment: An International Journal, 25*(5), 1125-1136.

Gong, M., Wu, L., Bi, X.-y., Ren, L.-m., Wang, L., Ma, Z.-d., *et al.* (2010). Assessing heavy-metal contamination and sources by GIS-based approach and multivariate analysis of urban–rural topsoils in Wuhan, central China. *Environmental Geochemistry and Health, 32*(1), 59-72.

Hakanson, L. (1980). An ecological risk index for aquatic pollution control.a sedimentological approach. *Water Research, 14*(8), 975-1001.

Hou, D., O'Connor, D., Nathanail, P., Tian, L. & Ma, Y. (2017). Integrated GIS and multivariate statistical analysis for regional scale assessment of heavy metal soil contamination: A critical review. *Environmental Pollution, 231*, 1188-1200.

Huang, Y., Li, T., Wu, C., He, Z., Japenga, J., Deng, M. & Yang, X. (2015). An integrated approach to assess heavy metal source apportionment in peri-urban agricultural soils. *Journal of Hazardous materials, 299*, 540-549.

Kabata-Pendias, A. (2010). *Trace elements in soils and plants* (F. ed. Ed.). Boca Raton, FL, USA: CRC Press: Taylor & Francis Group.

Kaur, M., Kumar, A., Mehra, R. & Mishra, R. (2018). Human health risk assessment from exposure of heavy metals in soil samples of Jammu district of Jammu and Kashmir, India. *Arabian Journal of Geosciences, 11*(15), 411.

Keshavarzi, A. & Kumar, V. (2019). Ecological risk assessment and source apportionment of heavy metal contamination in agricultural soils of Northeastern Iran. *International Journal of Environmental Health Research, 29*(5), 544-560.

Liu, M., Yang, Y., Yun, X., Zhang, M. & Wang, J. (2015). Concentrations, distribution, sources, and ecological risk assessment of heavy metals in agricultural topsoil of the Three Gorges Dam region, China. *Environmental Monitoring and Assessment, 187*(3), 147.

Ogunkunle, C. O. & Fatoba, P. O. (2014). Contamination and spatial distribution of heavy metals in topsoil surrounding a mega cement factory. *Atmospheric Pollution Research, 5*(2), 270-282.

Reimann, C., Fabian, K., Birke, M., Filzmoser, P., Demetriades, A., Négrel, P., *et al.* (2018). GEMAS: Establishing geochemical background and threshold for 53 chemical elements in European agricultural soil. *Applied Geochemistry, 88*, 302-318.

Simon, E., Vidic, A., Braun, M., Fábián, I. & Tóthmérész, B. (2013). Trace element concentrations in soils along urbanization gradients in the city of Wien, Austria. *Environmental Science and Pollution Research, 20*(2), 917-924.

Sun, Y., Zhou, Q., Xie, X. & Liu, R. (2010). Spatial, sources and risk assessment of heavy metal contamination of urban soils in typical regions of Shenyang, China. *Journal of Hazardous materials, 174*(1), 455-462.

Sürücü, A., Ahmed, T. K., Günal, E. & Budak, M. (2019). Spatial variability of some soil properties in an agricultural field of Halabja City of Sulaimani Governorate, Iraq. *Fresenius Environment Bulletin, 28*(1), 193-206.

Tóth, G., Hermann, T., Da Silva, M. R. & Montanarella, L. (2016). Heavy metals in agricultural soils of the European Union with implications for food safety. *Environment International, 88*, 299-309.

Trujillo-González, J. M., Torres-Mora, M. A., Keesstra, S., Brevik, E. C. & Jiménez-Ballesta, R. (2016). Heavy metal accumulation related to population density in road dust samples taken from urban sites under different land uses. *Science of the Total Environment, 553*, 636-642.

UNEP. (2013). Environmental risks and challenges of anthropogenic metals flows and cycles. A report of the working group on the global metal flows to the international resource panel. . In R. Salminen, M. Eckelman, G. Mudd, T. H. R. Norgate & E. Van der Voet (Eds.): UNEP, IRP.

Wedepohl, K. H. (1995). The composition of the continental crust. *Geochimica et Cosmochimica Acta, 59*(7), 1217-1232.

Zheng-Qi, X., Shi-Jun, N., Xian-Guo, T. & Cheng-Jiang, Z. (2008). Calculation of Heavy Metals' Toxicity Coefficient in the Evaluation of Potential Ecological Risk Index [J]. *Environmental Science & Technology, 2*(8), 31.

Zhong, T., Chen, D. & Zhang, X. (2016). Identification of Potential Sources of Mercury (Hg) in Farmland Soil Using a Decision Tree Method in China. *International Journal of Environmental Research and Public Health, 13*(11), 1111.

Research Article

Geochemical Evaluation of Formation Water, Mauddud Reservoir, Khabbaz Oilfield, Kirkuk Area, Northern Iraq

Fouad M. Qader [1, a, *], Basim Al-Qayim [2, b], Fawzi Al-Beyati [3, c]

[1] Department of Geology, College of Science, University of Sulaimani, Sulaymaniyah, KRI, Iraq
[2] Department of Petroleum Engineering, Komar University of Science and Technology, Sulaymaniyah, KRI, Iraq
[3] Survey Engineering Department, College of Kirkuk, North Technical University, Kirkuk, Iraq

E-mail: [a] fuad.qadir@univsul.edu.iq, [b] basim.alqayim@komar.edu.iq, [c] fawzialbiati@ntu.edy.iq

Access this article online		
Received on: June 5, 2021	**Accepted on:** December 8, 2021	**Published on:** December 28, 2021
DOI: 10.25079/ukhjse.v5n2y2021.pp28-35	**E-ISSN:** 2520-7792	

Abstract

In this study, formation-water samples were collected by NOC Staff, during drilling time, from the Mauddud Formation reservoir of the Khabbaz Oilfield, for this reason four samples from four wells; Kz-3, Kz-4, Kz-7, and Kz-23 were selected to geochemical analysis. Analyzed geochemical parameters include TDS and the concentrations of the different dissolved cations and anions present in brines (Ca^{+2}, Mg^{+2}, Na^{+1}, $SO4^{-2}$, Cl^{-1}, $HCO3^{-1}$, and NaCl). Variations among the resulted data are discussed by comparison with other Cretaceous Brines. Geochemical ratios of Na/Cl, (Na-Cl)/SO_4) and (Cl-Na)/Mg^{+2} was calculated for formation water classification following Bojarski, (1970). The calculated geochemical ratios of the studied samples in the studied four wells indicate that all of these waters are "chloride calcium" type under subsurface conditions, this type reflect closed system isolated associations reservoir, which are becoming high hydrostatic in deeper zones without influence by infiltration waters. A major transversal fault cutting the structure at its SE plunge had participated in the dilution of the Mauddud reservoir brine effectively.

Keywords: Formation Water, Mauddud, Khabbaz, Hydrochemistry, Brine, Iraq.

1. Introduction

Geochemical evaluation of formation water is an essential tool of reservoir management especially for fields with little studies such as the Khabbaz Oilfield of Kirkuk area of Northern Iraq. This analysis is used for long period in evaluating formation water chemistry as an approach to understand origin, nature and movement of formation water, which in turn helps in understanding the subsurface environment of the associated hydrocarbons accumulations (Collins, 1975).

The studied oil field is located about 20 km to the SW of Kirkuk City, and it represents a part of the Low Folded Zone of the Iraqi physiographic division. The field is surrounded from the northwest by Bai Hassan and Qara Chauq oil fields, from the southeast by Jambour. The Baba Dome of Kirkuk Oilfield is located to the east of Khabbaz Oilfield (Figure 1a). The length of the structure is about 20 km and its width reaches 4 km. It consists of an asymmetrical sub-domal anticline with northwest-southeast trend (Figure 1b). The northeast limb is steeper than the southwest limb. A major transversal normal fault intersects the structure in its south-eastern plunge (Figure 1c). These faults have important influence on field production and development (Al-Qayim *et al.,* 2010) and influences reservoir performance. The first seismic investigation for the area was done by Iraqi Petroleum Company (IPC) in 1955. They indicated this subsurface structure which is plunged toward northwest. The first well (Kz-1) at Khabbaz was drilled in August 1976, and the North Oil Company brought on stream in March 1994 (Al-Qayim *et al.,* 2010). Production comes from three pay zones: (1) The Tertiary reservoirs; (Middle Miocene Jeribe Formation, and Upper Oligocene-Lower Miocene Anah, Azkand,

and Azkand/ Ibrahim Formations); (2) Upper Cretaceous reservoirs Mauddud (Upper Qamchuqa) Formation; and (3) the Aptian Shu'aiba (Lower Qamchuqa) Formation.

Forty wells have been drilled so far at Khabbaz structure, most of which have targeted the Kirkuk Group (Oligocene) although number wells have penetrated the underlying Cretaceous reservoirs (Qader & Al-Qayim, 2016).

The study aimed at examining the hydrochemistry of water samples collected from the Mauddud reservoir in an attempt to elucidate a possible link between formation water geochemical characteristics and the nature of the subsurface environment of the hydrocarbon accumulation.

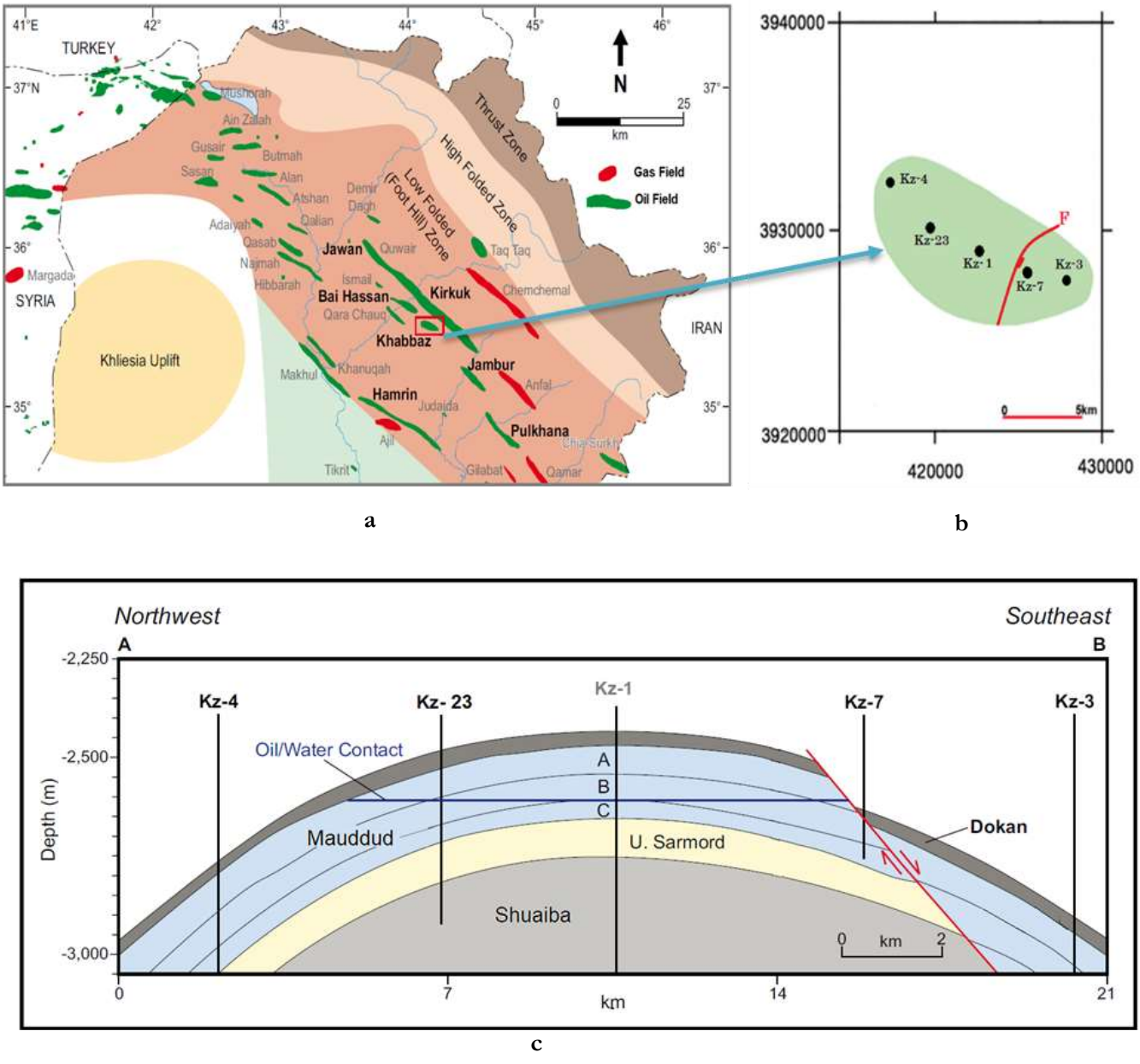

Figure 1. Index Diagram Showing. a) Location Map of Khabbaz Oilfield, b) The Studied Wells Over the Khabbaz Structure, c) Schematic Longitudinal Cross-Section Showing the Mauddud Reservoir Stratigraphy, and the Studied Wells. (Adopted after Al-Qayim *et al.*, 2010).

1.1. Mauddud Reservoir

The Qamchuqa Formation of the mountainous pattern of NE Iraq is formally described by Bellen *et al.* (1959) as a thick section of dolomitic limestone of an extensive distribution of carbonate platform. At Kirkuk area, the formation is stratigraphically better differentiated by Al-Sadooni (1978) into three formations: The Upper Qamchuqa (known as Mauddud Formation in central Iraq), the Upper Sarmord Formation, and the Lower Qamchuqa (known as Shuaiba

Formation in central Iraq) (Figure 2). This subdivision was adopted by most petroleum geologists working in the Kirkuk area and amended by Buday (1980).

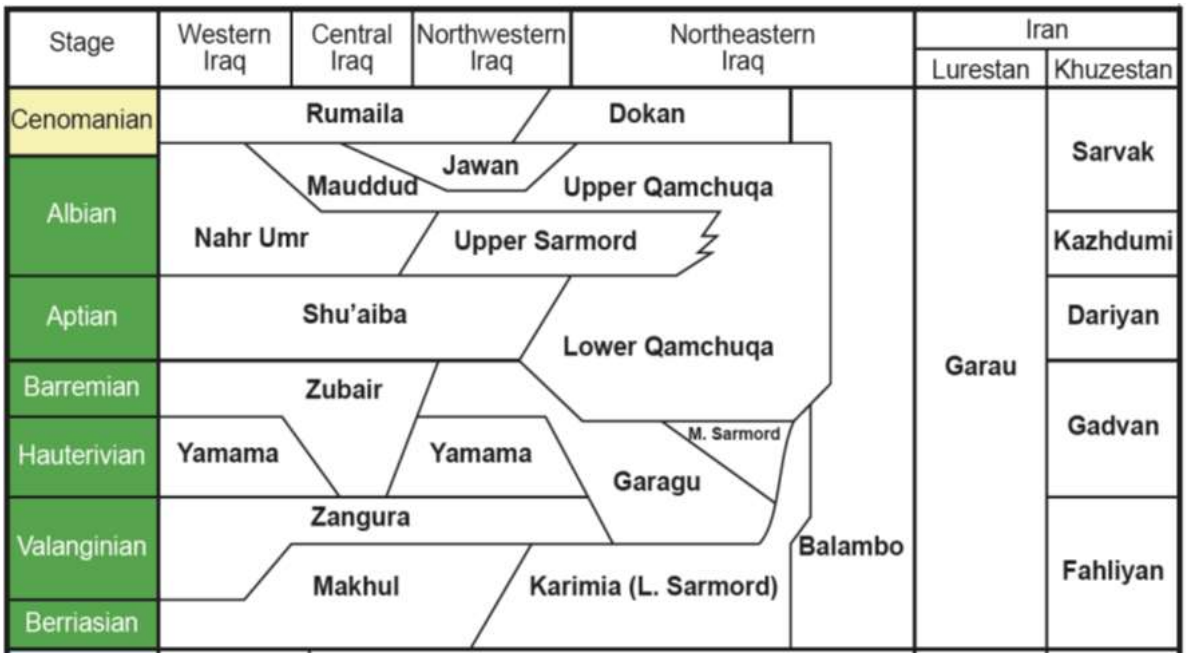

Figure 2. Lower Cretaceous Stratigraphic Chart and Nomenclature for Iraq (Al-Qayim *et al.*, 2010).

The Mauddud Formation is a widespread Late Albian unit, which represents an extensive shallow marine carbonate platform extends over most of the Arabian Platform (Sadooni & Alsharhan, 2003). The average thickness of the formation at Khabbaz Oil Field is around 170 m. The general lithology of the Mauddud Formation is characterized by intercalations (Al-Qayim *et al.,* 2010) of limestone, dolomitic limestone, and dolostone with infrequent marl intercalations. Based on that, the reservoir is subdivided into three units. The upper unit has the best petrophysical properties with potential dolostone horizons having porosities up to 25%. In addition to intercrystalline porosity, vugs and fracturing are also common and enhanced reservoir permeability (Al-Qayim *et al.,* 2010).

Mauddud Formation in Khabbaz Oilfield represents unconformable contact situation with the overlying Dokan Formation; this situation was detected on the **GR** log pattern through abrupt increasing in values at contact within the studied well sections all over the field (Figure 3). Similar case was reported by Al-Peryadi (2002) from Bai Hassan Oilfield, also the sonic transit time (Δt μs/ft) pattern was emphasizing the above indication through recording low values along the limestone rocks of Dokan Formation. The lower contact with underlying Upper Sarmord Formation is conformable which is reflected by a gradational increase of GR from the lower part of the Mauddud Formation toward the upper shale-dominant part Upper Sarmord Formation (Figure 3). The Upper Sarmord Formation is about 120 m, and consists of shale, marl and argillaceous limestone (Qader, 2008).

The Neutron, Density, and Sonic (porosity logs) patterns revealed gradational decreasing in porosity toward the base of the studied formation.

2. Material and Methods

The studied water samples were collected from Kz-3, Kz-4, Kz-7, and Kz-23 wells, which distributed on the stricter of Kabbaz Oilfield during drilling time (Figure 1). Samples were analyzed at the laboratories of the North Oil Company of Iraq (N.O.C.), and resulted data are presented in an internal report (Reports of Petroleum Engineering Department of NOC, 1976-1982). The results of the analysis were calculated first in ppm (Table 1). Analysis includes TDS, Major cations (Ca^{+2}, Mg^{+2}, and Na^{+1}) and anions (SO_4^{-2}, Cl^{-1} and HCO_3^{-1}) in addition to (Na-Cl). The analyzed data is compared to modern seawater chemical composition (after Castro and Huber (2019) and other Iraqi Cretaceous brines with similar hydrochemical analysis were obtained by Awadh *et al.* (2018) and Awadh, *et al.* (2019) in order to highlight variations. This comparison is intended at evaluating general variations in the analyzed samples (Table 1). The resulted analytical values were then recalculated into equivalent per-million (**epm**) values (Table 2), so it can be used later on in the calculation of the percentages of the different parameters (hydrogeochemical ratios) in the water type classification approach. The water type classification is following here Sulin (1946) and its modification by Bojariski (1970) as

presented in Collins (1975). This classification is selected here for the classification and its suitability of the analyzed data.

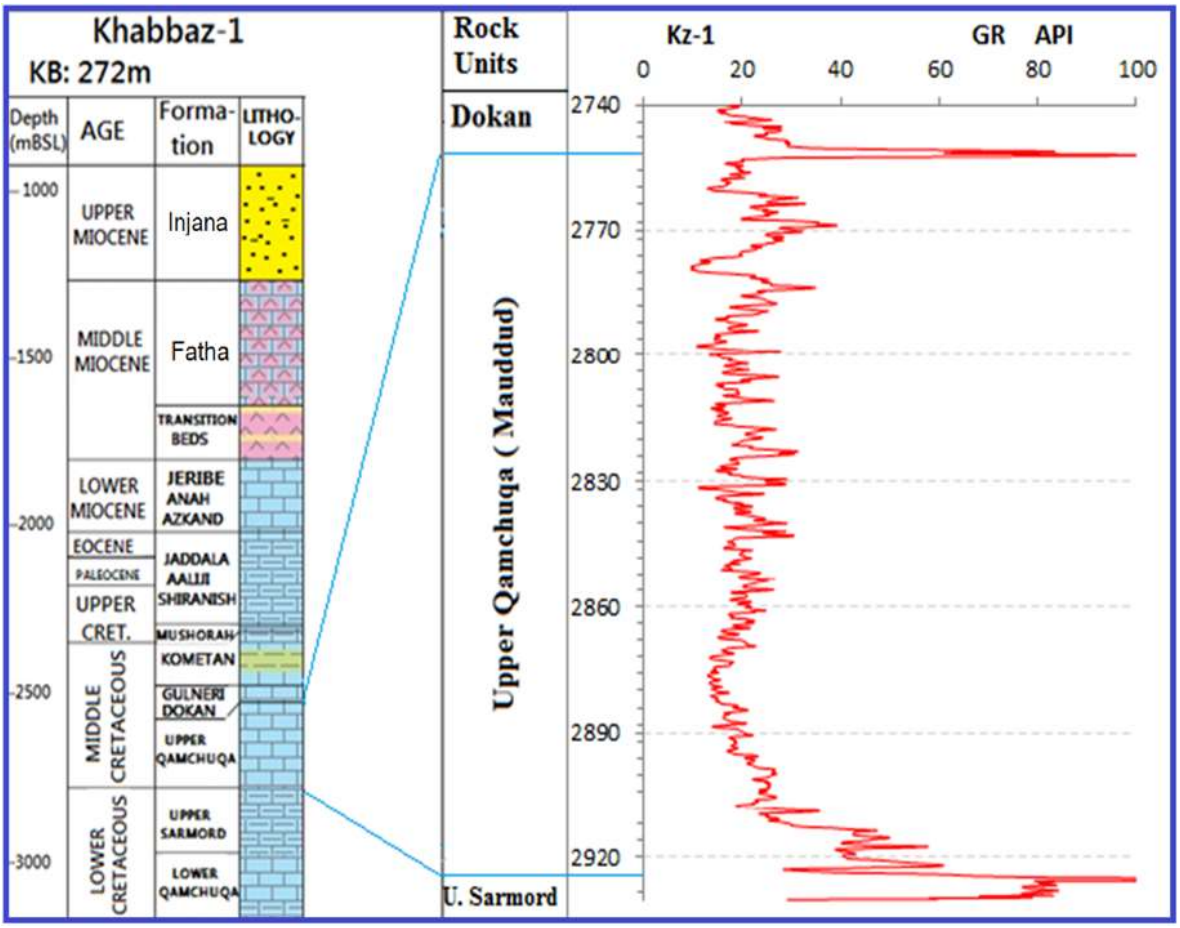

Figure 3. General Stratigraphic Column of the Khabbaz Oilfield at Well Kz -1, Showing Detailed Lithologies and GR log Characters of the Mauddud (Upper Qamchuqa) Formation.

3. Results

The resulted data of the hydrochemical analysis of the selected samples are presented in Table 1. An overall look to the results of the formation water analysis shows sufficiently higher concentration of dissolved salts as compared to the original chemical composition of modern seawater (Table 1). The average TDS value of the analyzed water samples are almost 3 times the TDS value of seawater. This higher concentration is also noticed for most of the cations and anions including Ca^{+2}, Mg^{+2}, Na^{+1}, Cl^{-1}, and HCO_3^{-1}. This high concentration of the formation brine is also noticed in comparison with average values of brines from Cretaceous System in Table 1 (Collins, 1975). The concentration of subsurface brine often related to evaporation during deposition of shallow restricted marine environments such lagoons, pans and subkhas (Collins, 1975), or due to compaction and membrane filtration of clay sediments (Chilingarian & Rieke, 1969 in Collins, 1975). Parker (1969 in Collins, 1975) had studied brines and waters from five aquifers of Cretaceous age in the East Texas Basin. He found that the composition of the waters in the older, more deeply buried aquifers was modified more than waters in younger, less deeply buried formations. The exceptional lower average value of the sulfates (1184 ppm) as compared to seawater value (2701 ppm) is believed to be related to inorganic reduction of sulfate, anaerobic reduction or hydrocarbon reduction of anhydrite (Bush, 1970 in Collins 1975). The relative lower concentration of the subsurface brine of the Mauddud reservoir as compared to the other Cretaceous reservoirs of southern Iraq may be related to dilution by surface water percolated through the master fault deeply intersect the Khabbaz Structure (Figure 1). It is also noticed that despite the high concentration of the Mauddud reservoir brine, it has comparatively, lower total dissolved salts (TDS) as well as most of the analyzed elements than the Cretaceous reservoirs of southern Iraq as shown in Table 1 (Awadh *et al.*, 2018; Awadh *et al,* 2019). It is noticeable that the chemical analysis of the water sample from Kz-7 show relatively low concentration of TDS and other cations and anions

compared to the other studied wells, seawater composition, as well as the Cretaceous reservoirs of southern Iraq (Table 1). The exceptional low concentration of the subsurface brine at well Kz-7 as compared to the other wells, and the low values of the TDS and other cations and anions of the Mauddud reservoir, as compared to other Cretaceous reservoirs may be related to the dilution of the subsurface brine. A process can be developed by surface water percolating down through the master fault which is deeply intersect the Khabbaz Structure at the southeastern plunge (Figure 1).

3.1. Classification of Oilfield Waters

The classification of subsurface water depends on the dominant mineral ions present in solution. The Russian geochemist classification widely used in this context like Sulin (1946, in Collins, 1975). His classification of the subsurface hydrochemical system based upon various combinations of dissolved salts in the waters. The classification revealed four basic water types each one refers to different environments from natural water distribution (Table 3):

1- Terrestrial conditions refer to the genetic type of such sulfate waters as *"sulfate-sodium*".
2- Continental conditions refer to the sodium bicarbonate waters formation. The genetic type is *"bicarbonate-sodium*".
3- Marine conditions allow to formation "*chloride-magnesium*" water type.
4- The deep subsurface conditions within the earth's crust allow to formation of a "*chloride-calcium"* water type.

The first two types are reflected meteoric and/or artesian waters properties, while the third one belongs to marine environments and evaporite sequences, the fourth type represents deep stagnant water conditions.

Sulin's (1946) system was modified by Bojarski (1970 in Collins, 1975). The modification emphasized the redefinition of Sulin's (1946) classification of water types and reinterpretation the environment of each water types as follow:

1- The "*bicarbonate-sodium*" Water type occurs in the upper horizon of sedimentation environment, under hydrodynamic conditions, which promotes to preservation of petroleum and natural gas deposits.
2- The "*sulfate – sodium*" water type, indicates to the sodium reaction with the chloride or sulfate.

Table 1. Formation Water Geochemical Analyses in Khabbaz Oilfield. Comparison with Seawater and Other Cretaceous Brines is Given Below for the Sake of Evaluation (Castro & Huber, 2019; Awadh et al., 2019; Awadh et al., 2018; Collins, 1975).

Wells No.	TDS ppm	Ca^{+2} ppm	Mg^{+2} ppm	Na^{+1} ppm	SO_4^{-2} ppm	Cl^{-1} ppm	HCO_3^{-1} ppm	NaCl ppm
Kz-3	130137	6006	1091	43008	1239	77823	1832	109317
Kz-4	151310	4830	1840	46998	1059	84909	1220	119461
Kz-7	27580	662	458	6302	1654	10295	1220	16018
Kz-23	127937	26588	13220	811	641	86380	Nil	2061
Average	109241	9521	4152	24279	1148	64851	1068	61714
Seawater (1)	35000	416	1295	10752	2701	19345	145	_
Zubair (2) **Reservoir**	215625	14674	3542	59200	417	123679	137	_
Mishrif (3) **Reservoir**	221660	12196	3091	68779	673	131751	223	_
Cretaceous (4) **System**	_	7000	900	31000	280	62000	260	_

Table 2. Formation Waters Geochemical Analysis Data of the Khabbaz Oilfield Converted into epm Values.

Wells No.	TDS ppm	Ca^{+2} epm	Mg^{+2} epm	Na^{+1} epm	$SO4^{-2}$ epm	Cl^{-1} epm	HCO_3^{-1} epm
Kz-3	130137	300	91	1870	26	2192	30
Kz-4	151310	242	153	2043	22	2392	20
Kz-7	27580	33	38	274	34	290	20
Kz-23	127937	1329	1102	35	13	2433	Nil

Waters of the "*chloride – magnesium"* type is characteristic of the transition zone between hydrodynamic areas which is becoming more hydrostatic in the deeper part of the basin.

3- Water of the "*chloride – calcium"* type occurs in deeper zones which is isolated from the influence of infiltration waters, and is hydrostatic.

Large variation in the chemical composition in the chloride – calcium type and subdivided this type was observed by (Bojariski, 1970 in Collins, 1975) as following:

a- Class, **"chloride – calcium I"** with ratio of Na/Cl > 0.85 refers to an active hydrodynamic zone. It is considered as a zone of little prospect for the preservation of the hydrocarbon.

b- Class, **"chloride – calcium II"** with ratio of Na/Cl = 0.85 – 0.75, refers to the transition zone between hydrodynamic zone and stable hydrostatic zone. It is considered as a poor zone for hydrocarbon preservation.

c- Class, **"chloride – calcium III"** with ratio of Na/Cl = 0.75 – 0.65, represents condition for the favorable preservation of hydrocarbon deposits. It is designated as a fairly hydrocarbon preservation environment.

d- Class, **"chloride – calcium IV"** with ratio of Na/Cl = 0.65 – 0.50, represents a complete isolation environment of hydrocarbon accumulation as well as by the presence of residual water. This class represents good zone for hydrocarbon preservation.

e- Class, **"chloride – calcium V"** with ratio of Na/Cl < 0.50, refers to the presence of highly altered residual ancient seawater. This type is one of the most likely indicators for the hydrocarbon accumulation zone.

Table 3. Parameters of Sulin (1946) and Bojarski (1970) Formation Water Classification.

Type of water	Na^+/Cl^-	$(Na^+ - Cl^-) / SO4^{-2}$	$(Cl^- - Na^+)/ Mg^{+2}$
Sulfate – Sodium	> 1	< 1	< 0
Bicarbonate – Sodium	> 1	> 1	< 0
Chloride – Magnesium	< 1	< 0	< 1
Chloride – Calcium	< 1	< 0	> 1

3.2. Classification of Mauddud Formation waters

The resulted epm data of Table 2 were recalculated in percentage to estimate the Sulin's- Bajoriskki basic hydrochemical parameters used in the classification of the formation water. The calculated parameters represent ratios either between (Na^{+1}/Cl^{-1})or between ($Na^{+1} - Cl^{-1})/SO_4^{-2}$), and ($Cl^{-1} - Na^{+1})/Mg^{+2}$) which reflect the chemical composition of the analyzed water, the type, and class of each water samples from each of the studied wells are shown in Table 4.

Table 4. The Mauddud Reservoir Formation Water Type and Classes According to Bojarski (1970) and Sulin's (1946) Classification.

Wells No.	Na^{+1}/Cl^{-1}	$(Na^{+1} - C^{-1})/ SO_4^{-2}$	$(Cl^{-1} - Na^{+1}) /Mg^{+2}$	Water type	Class
Kz-3	0.85	-12.49	3.69	***Chloride calcium***	**II**
Kz-4	0.85	-15.79	2.37	***Chloride calcium***	**II**
Kz-7	0.94	-0.46	0.44	***Chloride magnesium***	**---**
Kz-23	0.01	-179.57	2.27	***Chloride calcium***	**V**

Table 4 shows that three of four analyzed samples are refer to the dominant of "chloride-calcium" type, due to the ratio of $(Cl^{-1}-Na^{+1})/Mg^{+2}$) which represents value more than one among the three analyzed samples. The dominant type of water from studied wells Kz-3, Kz-4, and Kz-23 represents a hydrostatic deeper zone, which refers to the semi - completely isolated environment may be due to the influence by infiltration waters according to Bojarski (1970). The sample from well Kz-7 revealed "chloride magnesium" type $(Cl^{-1}-Na^{+1})/Mg^{+2}$), in order to the value of the ratio was less than one which refer to the situation of transition zone between dominated hydrodynamic areas which was became more hydrostatic at deeper part of the environment.

Some variations were detected among "chloride calcium" water type within their Na^{+1}/Cl^{-1} ratios that were analyzed from the three studied wells, therefore, it must be subjected to subdivision within one classis of Bojarski (1970).

The ratio of Na^{+1}/Cl^{-1} obtained from the two (Kz-3 and Kz-4) wells are equal to 0.85. This value according to Bojarski (1970) classification is return to the subdivision of second class (chloride-calcium II) of formation water that is very close to the first class (chloride-calcium I) as well. The value of 0.85 refers to the transition zone between hydrodynamic and stable hydrostatic zones, and this zone is generally representing poor zone for hydrocarbon preservation. Such variation in the result may be due to the sampled wells locations. The wells Kz-3 and Kz-4 are located at the extreme ends of the studied field structure (Figure 1), and thus affected by the transitional nature of the marginal waters of the pool. The Na^{+1}/Cl^{-1} ions ratio obtained in the well Kz-23 was 0.01, this value belongs to the fifth class (chloride-calcium V), which represents a good zone for hydrocarbon preservation.

The location of Kz-23 Well nearest to the central part of studied field (Figure 1) probably represents the typical formation water that associated with the assemblies of oil pool within the studied reservoir of Khabbaz Oilfield. The formation water represents the ancient residual sea water, and most likely represents an area of hydrocarbon accumulation (Bojariski, 1970 in Collins, 1975)

The well Kz-7 revealed ratio of Na^{+1}/Cl^{-1} equals to 0.94, this value return to the class I of chloride-calcium formation water type, and this value close to the value of class III chloride – magnesium formation water type. The interpretation may be probably related to the location of the well Kz-7 which affected by the intersecting a major fault (Figure 1) (Qader, 2008). The fault plays a key role in creating a hydrodymic condition at the well Kz-7 and may cause intermixture of the formation water with other type of water passes through the fault plane.

4. Discussion

The location of studied oilfield within the Low Folded Zone, which is characterize by the domain of intense hydrodynamic effect as a result of the culminating tectonic deformation of the Zagros Orogenic Belt. The intensive fracturing and faulting of the Mauddud reservoir is characteristic in many fields of northern Iraq such as Khabbaz Oilfield (Al-Qayim *et al.*, 2010), Bai Hassan Oilfield (Al-Peryadi, 2002), Jambour Oilfield (Al-Shakiry, 1977), and Miran Oilfield (Rashid *et al.,* 2020). It is conceivable, thus, to see some intermixing of the Khabbaz formation water with other type of water from shallower depth including meteoric water percolating through fractures and faults, namely, the master fault at the southeastern plunge of the structure (Figure 1). The invasion by surface water will lead to dilution of the salinity of the original brine as compared to other Cretaceous formation waters. While the greater resistance to the invasion was existence, multi layers from clay and anhydrite succession above the studied reservoir rocks, which helped the site faraway from hydrodynamic effect and contributed to enhance the close system (Al-Mashadani, 1986). Also due to high pressure reported from the Mauddud reservoir which was reached 4364 psi at depth of 2685m (Reports of Petroleum Engineering Department, 1976-1982), this pressure is indicates to an anomaly situation from hydrodynamic condition when compared with either interstitial fluid pressure or theoretically estimated hydrostatic pressure. The estimated pressure gradient of a formation of 0.48 psi/ft or 1.50 psi/m (Serra, 1986), will be 4028 psi at the same depth (2685m). The resulted relatively high-pressure condition of the Mauddud reservoir represents isolated and close system within the Khabbaz Oilfield. These coincides with the dominant "chloride calcium" water type as inferred by Sulin-Bajoriski classification. This type indicate to the occurrence in the deeper zones which refer to relatively isolated, stagnant, and hydrostatic conditions (Sulin, 1946).

However, the wells with marginal location with respect to reservoir (Kz-3 and Kz-4) of "chloride calcium" type within Class II group are characterizes by the transition zone between an active hydrodynamic and stable hydrostatic zone, which is generally considered as a poor hydrocarbon preservation zone (Bojariski, 1970). Location of the well Kz-23 is on the apex of the structure passing through the central part of the oil zone (Figure 1). The water type of this well is of "chloride calcium" type but of class V group (Table 4). This type of water according to Bojarski (1970) is characterized by the presence of ancient residual seawater, which has been highly altered since original deposition, and considered as one of the most likely areas where hydrocarbons are accumulated.

The noted relatively diluted dissolved salts values of Kz-7 (TDS and other cation and anion) as compared to the other wells and its different water type (chloride magnesium) can be explained in term of location of the well close to the master fault of the structure. Such lower values are seemingly influenced by water infiltration through the fault zone, which is directly diluted its water salinity greater than the other wells.

5. Conclusions

The hydrogeochemical analysis of the formation water of the Mauddud reservoir at Khabbaz Oilfield reveals variable water types dominated by "chloride calcium "group which is in general indicates a relatively deep, isolated, and stagnant subsurface environment of transitional hydrostatic to hydrodynamic conditions. The noticed variability among the details of the analyzed water samples; however, are related to the location of the studied wells with respect to the water pool area (oil zone), and the position of the wells with regard to the master fault of the structure.

Acknowledgements

The North Oil Company (NOC), Kirkuk, to whom the authors express their gratitude, provided data and research materials of this study.

References

Al-Qayim, B., Qader, F. & Al-Biaty, F. (2010). Dolomitization and porosity evaluation of the Cretaceous Upper Qamchuqa (Mauddud) Formation, Khabbaz Oilfield, Kirkuk area, northern Iraq. *GeoArabia*, *15* (4), 49-76.

Al-Mashadani, A. (1986). Hydrodynamic Framework of the Petroleum Reservoir and Cap Rocks of the Mesopotamian Basin of Iraq. *Journal of Petroleum Geology*, *9* (1), 89-110.

Al-Peryadi, K. H. K. (2002). Sedimentological Study and Reservoir Characterizations for Upper Qamchuqa and Jawan Formations to Determine the Effective Porosity in Bai-Hassan Field. MSc thesis (in Arabic), University of Bagdad, Baghdad, Iraq.

Al-Sadooni, F. N. (1978). Sedimentology and Petroleum prospects of the Qamchuqa group – Northern Iraq. Unpublished PhD thesis, University of Bristol, Bristol, England.

Al-Shakiry, A.J. (1977). The Petrology of part of the Upper Qamchuqa Formation in Jambur Oil Field Iraq. MSc thesis, University of Bagdad, Baghdad, Iraq.

Awadh, S., Al-Mimar, H. & Al-Yaseri, A. (2018). Salinity mapping model and brine chemistry of Mishrif reservoir in Basrah oilfields, Southern Iraq. *Arabian Journal of Geosciences*, *11* (18), 551–563.

Awadh, S., Al-Auweldy, M. & Al-Yaseri, A. (2019). Hydrochemistry as a tool for interpreting brine origin and chemical equilibrium in oilfields: Zubair reservoir southern Iraq case study. *Applied Water Science*, 9 (65), 64-76.

Bellen, R.C. Van, Dunnington, H. V., Wetzel, R. & Morton, D. (1959). Lexique Stratigraphique International. 3. Retrieved from http://paleopolis.rediris.es/LEXICON/IRAQ/.

Buday, T. (1980). *The Regional Geology of Iraq, Vol 1: Stratigraphy and Paleogeography*. Baghdad, Iraq: Publications of Geological Survey of Iraq. pp. 445.

Castro, P. & Huber, M. (2019). *Marine Biology* (11th edition). New York, NY, USA: McGraw Hill Education.

Collins, A. (1975). *Geochemistry of oil field waters*. Amsterdam, Netherlands: Elsevier Scientific Publishing.

McCain, D. Jr. (1990). *The properties of Petroleum Fluids* (2nd edition). Tulsa, Oklahuma, USA: Penn Well Publishing Company.

Qader, F. (2008). *Formation Evaluation of Upper Qamchuqa Reservoir, Khabbaz Oil Field, Kirkuk Area, Northeastern Iraq*. Unpublished PhD thesis, University of Sulaimani, Sulaymaniyah, Iraq.

Qader, F. & Al-Qayim, B. (2016). Petrophysical and Sedimentological Characterization of the Aptian Shu'aiba (Lower Qamchuqa) Formation reservoir at the Khabaz Oil Field, Northern Iraq. *Journal of Petroleum Geology*, *39*(4), 375-392.

Rashid, F., Hussein, D., Lawrence, J. & Khanaqa, P. (2020). Characterization and impact on reservoir quality of fractures in the Cretaceous Qamchuqa Formation, Zagros folded belt. *Marine and Petroleum Geology*, *113*(3). doi: 10.1016/j.marpetgeo.2019.104117.

Reports of Petroleum Engineering Department (1985). North Oil Company, During the years 1976-1982.

Sadooni, F. N. & Alsharhan, A. S. (2003). Stratigraphy, microfacies, and petroleum potential of the Mauddud Formation (Albian-Cenomanian) in the Arabian Gulf basin. *AAPG Bulletin*, *87*(10), 1653-1680.

Serra, O. (1986). *Advanced Interpretation of Wireline Logs*. Schlumberger book.

Research Article

Preliminary Evaluation of Quality and Rank of Banik Coal, Zakho, Duhok Governorate, Kurdistan Region, Iraq

Govand H. Sherwani *

*Department of Civil Engineering, College of Engineering, Cihan University-Erbil, Erbil, KRI, Iraq
E-mail: govand.sherwani@cihanuniversity.edu.iq

Access this article online		
Received on: July 6, 2021	**Accepted on:** September 6, 2021	**Published on:** December 31, 2021
DOI: 10.25079/ukhjse.v5n2y2021.pp36-46	**E-ISSN:** 2520-7792	

Abstract

This study aims to evaluate the rank (or grade) and economic value of the so–called coal horizon/bed outcropping in the vicinity of Banik and Shiranish-Islam villages of Zakho District, Duhok Governorate, Iraq. These coal-like beds (locally known as Banik Coal) make up few meters within the upper part of the Jurassic Naokelekan Formation. The evaluation was mainly based on standard chemical tests of coal (proximate and ultimate analyses) achieved in foreign and local laboratories. The test results were assessed according to the standard coal tests introduced by the American Society for Testing and Materials (ASTM).

The latest stratigraphic studies revealed that the presumable coal horizon was thin beds of limestone and dolomitic limestone alternated with frequent shales all intensively impregnated with bituminous materials, mostly of hydrocarbon source. The bituminous beds were observed in both upper and lower parts of Naokelekan Formation. The standard proximate coal analysis has shown low percent of fixed carbon and high percent of volatiles and ash which support the hydrocarbon source of these bituminous beds. The high values of mineral matter display the dominance of minerals rather than the carbon in the local samples. Consequently, it would be difficult to classify these bituminous beds similarly to the standard coal ranks of ASTM. However, the Gross Calorific Value (heating value) of these beds would imply that they can be used as relatively poor quality source of fuel. Besides, the exploitation of Banik coals would be influenced by the cost of extraction (or mining), the expected prices of produced coal, and the prices of alternative sources of energy.

Keywords: Banik Coal, Duhok, Kurdistan Region, Naokelekan, Shiranish.

1. Introduction

1.1. Preface

By the early 1950s, and possibly earlier, the pioneer geologists of Iraq Petroleum Company (IPC) had launched programs of geologic survey of wide areas over Northern Iraq. Their efforts were originally stimulated by earlier discoveries and production of huge Tertiary oil accumulation in Kirkuk and other oil fields. Consequently, many geologic formations were named and given formal description for the first time. These newly described formations included some older units of the Triassic and Jurassic Periods, followed by others belonging to the Paleozoic Era.

The first stratigraphic description of the Jurassic Naokelekan Formation was presented by Morton and Wetzel (1950 in Bellen *et al.,* 1959), from a village called Naokelekan, located in the Imbricated Zone of Iraq, in the vicinity of Rawanduz town (Figure 1). The description of that section indicated the presence of the so-called Coal Horizon in its lower part of the Naokelekan Formation. That stratigraphic description, with further details, were presented with further geologic information by Jassim and Buday (2006).

Figure 1. Satellite image showing the location of the studied sections.

For several decades, exploration activities and plans for Northern Iraq had focused on seeking for hydrocarbons in areas away from the Imbricated and Thrust Zones that were believed to have poor petroleum potential. Consequently, little attention was paid to these presumed coal beds of the Naokelekan Formation.

1.2. Aim of the Study

The present study aims to highlight some of the geological and chemical aspects of the so-called Coal Horizons (or beds) described in the lower part of Naokelekan Formation. The current prospect attempts to offer the reply of questions such as:

- Are these beds real coal? If so, what is their grade or rank ?
- Have they any economic value or benefit to make a new source of energy ?

1.3. Study Area

In the present study, two locations/sections of the Naokelekan Formation, were selected. These locations involve outcrops of this formation near Banik village (locally known as Banik Haji Ghazi) and Shiranish-Islam village in Zakho District, Duhok Governorate, Iraqi Kurdistan Region (Figure 1). Once the Tectonic Subdivision of Iraq is considered, the study area of both sections lie in the Imbricated Zone of Northern Iraq (Fouad, 2015). The selection of these two sites was intended to facilitate comparison between the results of the lab tests of local samples with those of a samples in the vicinity of Silopi, the closest Turkish town.

2. Geologic Setting

2.1. Naokelekan Formation

The first stratigraphic description of the Jurassic Naokelekan Formation, presented by Morton and Wetzel (1950 in Bellen *et al.,* 1959), is briefed in a columnar section (Figure 2) which demonstrates several lithologies, with total thickness of 14m. This section displays that the lower and the upper parts, either the shale or carbonate fraction are dominantly

bituminous. The middle part of the Naokelekan Formation (called Mottled Bed) is fossiliferous dolomitic limestone with traces of ammonites.

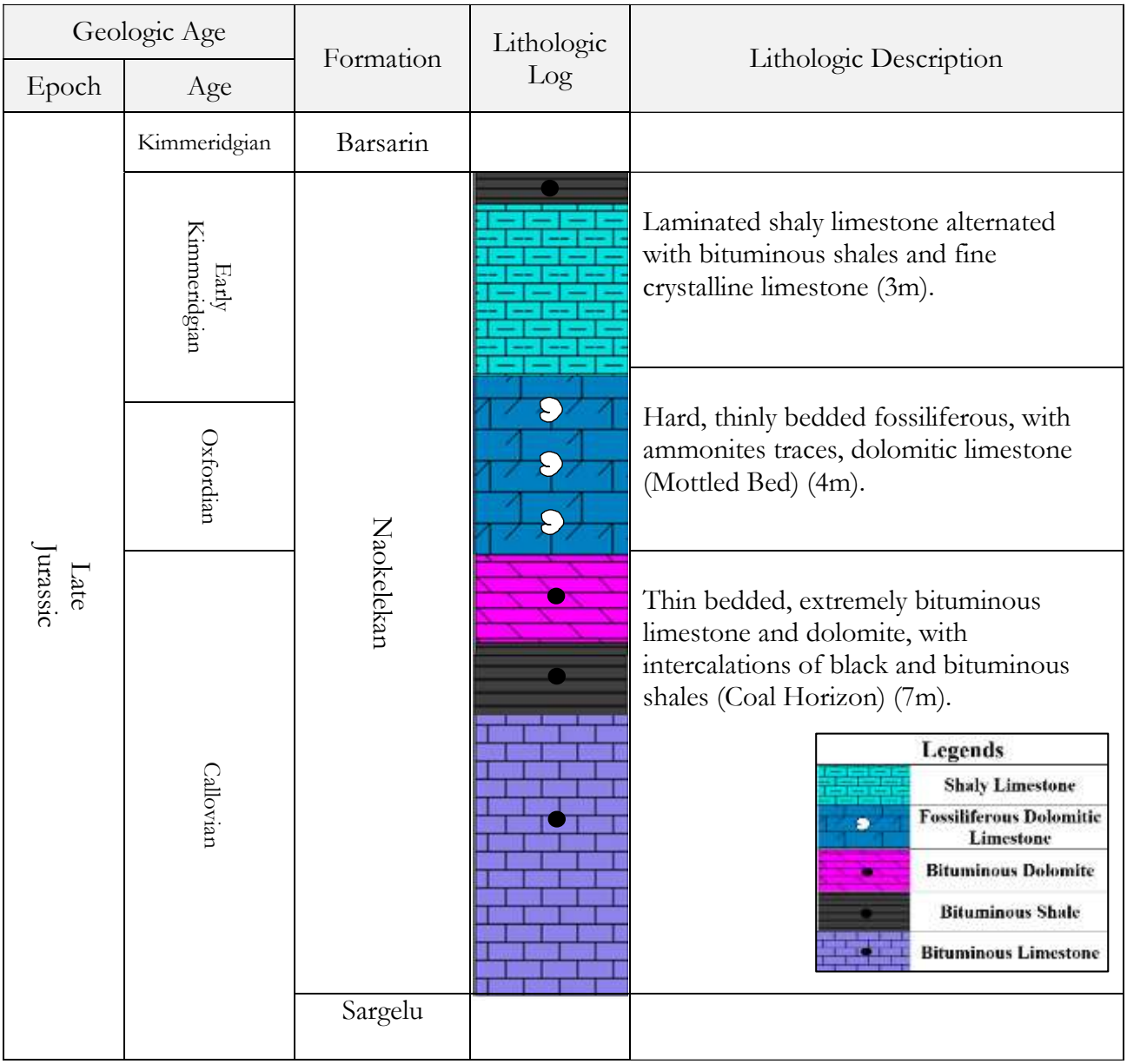

Figure 2. A Stratigraphic column manifesting the first formal description of Naokelekan Formation in its type section at Naokelekan Village, Erbil. (outlined from Morton and Wetzel 1950 in Bellen *et al.*, 1959)

No vertical Scale. The whole section is 14 m.

The lower unit of the Naokelekan Formation is composed of thin bedded, extremely bituminous limestone and dolomite, with beds of black bituminous shales. Influenced by its distinctive black color, the earlier geologic texts had referred to the lower unit as Coal Horizon, which was an informal field nomenclature.

The text prepared by Jassim and Goff (2006) stands as a comprehensive display concerning all disciplines of Geology of Iraq. That text added outlines of depositional environment and the sedimentary cycles of all Jurassic rock units, including the Naokelekan Formation. Salae (2001), in a post-graduate dissertation, contributed to depositional environment and diagenetic events of the Naokelekan Formation. Balaky (2015), in a sequence stratigraphic approach, believed that the Naokelekan Formation can be divided into two third-order sequences, the upper and lower parts of the Naokelekan Formation belong to two HST (Highstand Systems Tract), separated by a TST (Transgressive Systems

Tract) in the middle. Later, Abdula (2016) contributed to stratigraphy of the Naokelekan Formation and believed that its age in Iraqi Kurdistan is Callovian-Upper Oxfordian. Recently, Al-Atroshi *et al.* (2019) and Abdula *et al.* (2020) assessed the type and thermal maturity of organic matter, and the petroleum generation potential of the Naokelekan Formation, across the Kurdistan Region of Iraq, by applying organic petrographic methods and Rock Eval Pyrolysis.

2.2. Organic Matter in the Naokelekan Formation

The organic matter of the Naokelekan Formation was recognized as Types II and III kerogen (Othman, 1990; Al-Atroshi *et al.,* 2019), or Types III and IV (Abdula *et al.,* 2020). This kerogen was described as mature and within the oil generation window in Sargelu locality (Baban and Ahmed, 2014). Salae (2001) believed that the dark colored rocks of the Naokelekan Formation are due to kerogenous rather than bituminous material as was reported earlier by Bellen *et al.* (1959). Whereas Abdula (2016) stated that these rocks seem to be a mixture of kerogen and bitumen.

Salae (2001) and Balaky (2015) agreed that the succession of the Naokelekan Formation bears no evidences of the existence of real coal, and that the presumed coal horizon is absent and replaced by argillaceous limestone in Hanjera and Barsarin sections. Whereas, Abdula (2018) argued that the coal horizon/bed is existing in Barsarin section. Al-Badri (2012), in a different perspective, stated that the lower part of the formation at Banik section (only 7m thick), is composed of alternating calcareous siltstone and shale, dark grey to black brittle coal and coaly calcareous mudstone, overlain by 4m-thick, brittle, and dark carbonaceous calcareous mud rock and dolosiltite.

In some cases, where bituminous material is filling the fractured sedimentary rock, the emplacement of bitumen into the fractures occurs under high pressure causing brecciation and impregnation (Parnell *et al.,* 1998). The sequence stratigraphic setting exposed by Balaky (2015), placing the upper part of the Naokelekan Formations as HST, would secure a suitable condition for impregnation of bitumen in the limestone and dolomite strata. The evaluation of organic matter presented by Abdula *et al.* (2020) implied that the bitumen in the Naokelekan Formation is mainly migrated (migra-bitumen) and partly formed through heating (pyro-bitumen) of ancestor organic matter during maturation stages.

As for the current case, it is believed that bitumen injection into the Naokelekan Formation followed fracturing of deeply seated hydrocarbon reservoir that received hydrocarbon from early Jurassic or older source rocks.

2.3. Coal Occurrence in the neighboring Countries

2.3.1. Iran

The black coal deposits of Iran refer to Jurassic age in the Alborz area, with some Tertiary Lignite of Khorasan area. The Alborz Jurassic coal is bituminous with high ash and sulphur content (Thomas, 2002). These coals are utilized for local need of energy and limited metallurgical industries. Considering the geologic age and the geographic location, the bituminous coal of Alborz is likely correlatable with the Iraqi Banik coal that is included within the Jurassic Naokelekan Formation.

2.3.2. Turkey

Considerable coal deposits are found in Carboniferous and Tertiary rocks of Turkey. The Carboniferous coals (Zonguldak coalfields) are found in the north and are of bituminous type with low ash and sulphur. The Tertiary Lignite coals are found in western and central Turkey (Thomas, 2002). The largest open-cast coal mine of Turkey is Afsin-Elbistan mine (central Turkey) where Pliocene deposits are targeted for Lignite.

3. Methodology

The current prospect included site investigation of the Naokelekan Formation and its bituminous (coal-like) beds, particularly in the vicinity of Banik and Shiranish villages (Figure 1), near Zakho town, Iraqi Kurdistan Region. This was followed by collecting fresh representative rock samples of the highly bituminous beds (Coal Horizon). Later, the coal samples were tested through the standard coal tests of American Society for Testing and Materials (ASTM): (Proximate Analysis - D3172-13, and Ultimate Analysis D3176-15) in chemical labs in a local university and abroad. The evaluation of mineral content, rather than carbon, in the analysed samples were performed via mathematical calculation of a newly introduced coal quality parameter called Mineral Matter (MM) (Thomas, 2002). The study terminates with evaluation of coal properties and rank (or grade) of the local samples through comparing the percent of their chemical components and properties with the standard tables of coal ranks. The comparison was additionally visualized by explanatory charts.

4. Results and Discussion

4.1. Standard Coal Analysis

The analysis of coal has a decisive role in designating the rank (or grade) of coal, hence, its economic value as a source for energy. The common analytical approaches for coal are based on either the British Standards (BIS) or the American Standards (ASTM D3172-13 and ASTM D3176-15). It is imperative to understand that all these analyses would clarify how the different chemical components of coal (moisture, ash, volatile, and fixed carbon) are related to each other and how they change among the various coal ranks (Thomas, 2012). Out of all analytical systems, two standard sets of analyses are performed:

4.1.1. Proximate Analysis (ASTM Standards D3172-13)

This is the first standard test performed on coals (or coal-like samples), and is intended to identify the quantity (percent) of the main chemical components (Moisture, Ash, Volatiles, and Fixed Carbon) of a coal sample. The most reliable Proximate Analysis Table is that presented by ASTM (Table 1). Most of specialized labs would add the calculated heat (or calorific) value to the table of Proximate Analysis.

4.1.2. Ultimate Analysis (ASTM Standards D3176-15)

This analysis is considered as the final test on the coal samples. It is performed to determine the percentage of Carbon and Hydrogen released in form of gaseous products after complete combustion of coal (Thomas, 2002). It also determines of the remaining Sulphur, and Nitrogen. In the Ultimate Analysis, the percentage of Oxygen, which is a component of many organic and inorganic compounds in coal, is estimated as well (Table 2). This test is recommended, once the results of Proximate Analysis were encouraging and indicative to rich coal bearing strata.

Table 1. Standard Proximate Analysis of coal (ASTM standards D3172-13).

The two charts below display the increase of Carbon Percent and Calorific Values, starting from Lignite (lowest grade) to Anthracite (highest grade).

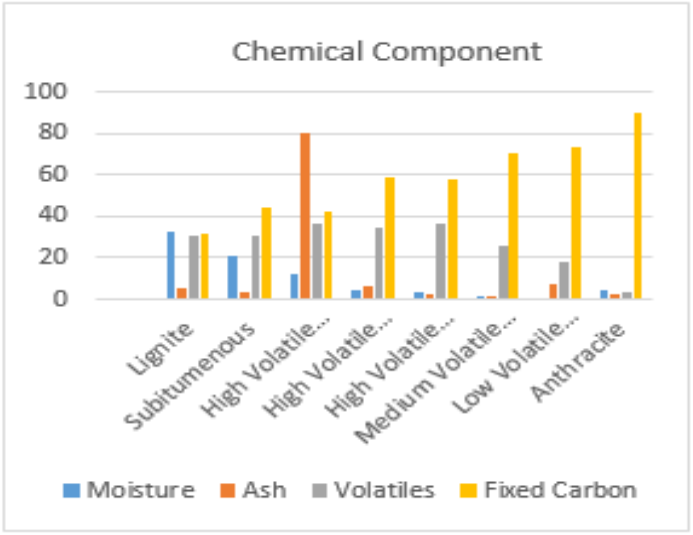

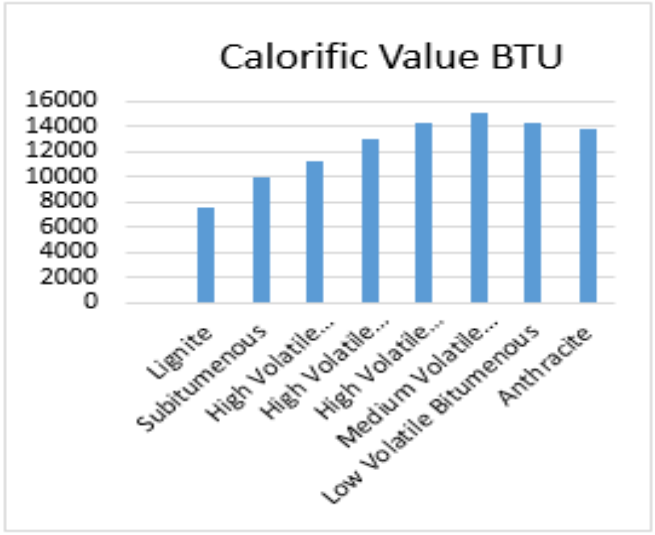

Coal Rank	Moisture	Ash	Volatiles			

(Coal Grade)	%	%	%	Fixed Carbon %	Calorific Value BTU/lb	Calorific Value cal/gm
Lignite	32.5	5.0	30.8	31.7	7626	4237
Sub-Bituminous	20.7	3.9	30.7	44.7	10029	5572
High Volatile Bituminous– C	11.9	8.5	36.9	42.7	11282	6268
High Volatile Bituminous- B	4.2	6.4	34.6	58.8	13105	7281
High Volatile Bituminous- A	3.0	2.4	36.3	58.3	14326	7959
Medium Volatile Bituminous	1.4	1.8	26.0	70.8	15091	8384
Low Volatile Bituminous	0.6	7.4	18.2	73.8	14380	7989
Anthracite	4.2	2.4	3.1	90.3	13791	7662

4.2. Analysis of Local Coal Samples

The main Proximate Analysis of samples from the coal horizon of the Naokelekan Formation was executed in a specialized lab in Turkey (Table 3). This table displays the main chemical contents of the samples. An extra test, to estimate the Gross Calorific Value (GCV) and effect of sample dryness, was conducted in the Labs of Department of Chemistry, College of Science, Salahaddin University, Erbil (Table 4).

Table 2. Standard Ultimate Analysis of coal (ASTM standards D3176-15)

The chart below displays that the element carbon increases with the increase in coal grade (from Lignite to Anthracite).

Coal Rank (Coal Grade)	C %	H %	N %	S %	O %
Lignite	72.4	5.3	1.1	0.7	20.5

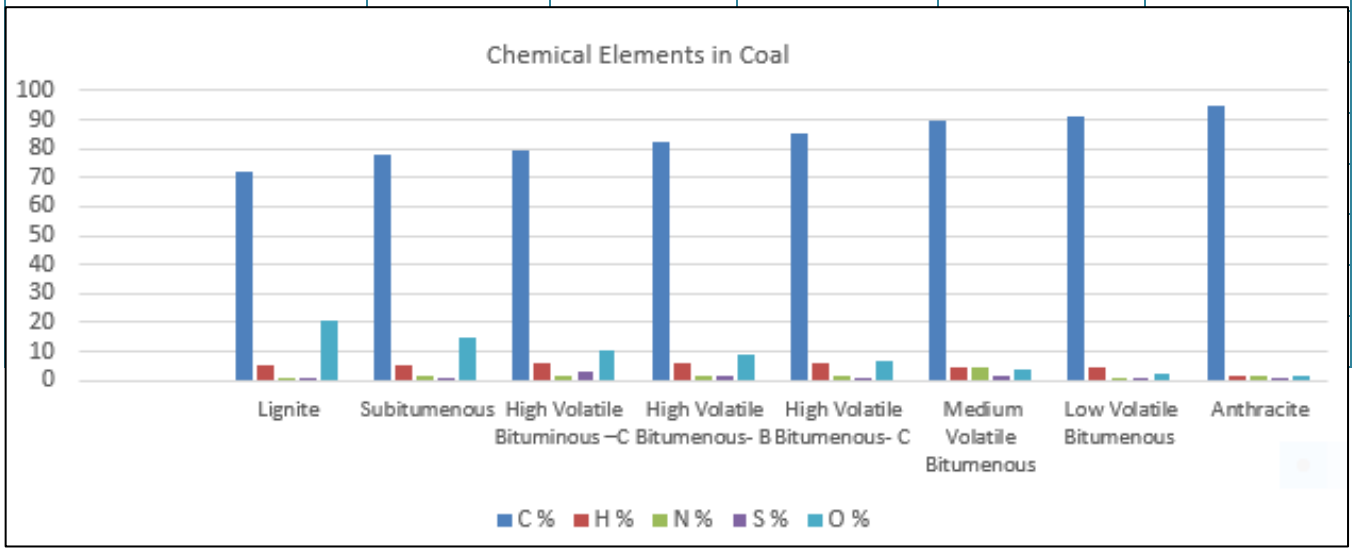

Table 3. Proximate Analysis of Coal samples from the Naokelekan Formation, in Banik and Shiranish sections, compared with one sample from Silopi section, Turkey

Section – Sample No	Moisture %	Ash %	Volatile %	Fixed Carbon %
Banik – 1	0.4	54.7	35.5	9.4
Shiranish - 1	0.4	50.5	39.8	9.3
Shiranish - 2	6.2	37.7	46.2	9.9
Shiranish - 3	0.6	44.6	45.9	8.9
Silopi	0.9	30.9	56.7	11.5

Table 4. Standard Proximate Analysis of Naokelekan coal samples – Shiranish site, executed at the Chemistry Labs of Salahaddin University, Erbil.

Samples	Moisture %	Ash %	Volatile %	Fixed Carbon %	Gross Calorific Value (GCV)	
					BTU / lb	cal / gm
Shiranish Sample	0.45	45.80	41.90	11.85	4194 - 4478	2330 – 2488
					average: 4336	average : 2409
Dry Sample	-	46.02	42.07	11.91	4498 - 6217	2343 – 2499
					average: 5357	average: 2921
Sulfur (S) %	in Original Sample		1.96 %			
	in the Ash		0.92 %			
	Total Sulfur		2.88 %			

4.3. Assessment of Analysis Results

4.3.1. Moisture Content

The moisture content is well considered in the coal industry, as it increases with decreasing rank of the coal (Thomas, 2002). Practically, the high moisture content is not desirable because it would consume some of the heat (calories) during burning and adds extra weight during transport (Thomas, 2002). However, the moisture content in the tested samples of Banik coal (Table 3) is extremely low and ranges between 0.4 to 0.9 %, with one anomalous figure in the sample of Shiranish-2. Drying coal samples results in increase of Gross Calorific Values for 21% (using cal/gm units) and 23% (using BTU units) (Table 4).

4.3.2. Ash Content

This component refers to the inorganic ingredients left post combustion of coal**.** The ash percent does not indicate the whole mineral matter in the coal, but those remained after losing volatiles (CO_2, SO_2, and H_2O) that are derived from carbonates, sulphides and clays (Nicholls, 1968). In a similar manner to moisture content, the high ash content would reduce calorific value of the coal. The favorite percent of ash for general usages would be around 20% (Thomas, 2002), whereas in the local samples, the average is around 50%, which is high and clearly and indicates the dominance of carbonate matters (Table 3). However, the sample from Silopi, Turkey has 30.9% Ash, which is still high (Table 3).

4.3.3. Volatile Percent

The amount of volatiles refers to gaseous constituent of coal that is released after air-free burning of coal at high temperature (Farhaduzzaman *et al.,* 2015). It belongs to mainly organic matter with lesser mineral content (Thomas, 2002). The recommended range of volatiles in coal or coal-like rocks is 20-40% (Thomas, 2002). Whereas, in the selected

samples, at Shiranish and Banik sites, their values were slightly above and below this range (Tables 3 and 4), as they were between 35 and 46%, which makes no obstacle for domestic and most of industrial usages.

4.3.4. Fixed carbon

Fixed carbon refers to the percent of remaining carbon in the residue left after complete burning of coal. It is calculated by subtracting the volatile, moisture, and ash from the total percentage of 100% (Thomas, 2002). In the studied samples, the fixed carbon percent was notably low (8.9 - 9.9%) (Table 3). T he selected sample from the neighboring Turkish location (Silopi) had similar score of (11.9%). These figures are similar to those obtained from the test performed at Salahaddin University, Erbil (about 11.85 – 11.91 %) (Table 4). However, in the standard table of ASTM Standards (D3172-13), the lowest grade of coal (Lignite), shows over 30% of fixed carbon (Table 1).

4.3.5. Calorific Value (CV) of Coal

The Gross Calorific Value (GCV) is an important parameter that refers to the amount of heat for mass unit of coal after complete burning. The GCV is often called heating value or specific energy in some countries (Thomas, 2002). The calorific values of the dry sample from the Naokelekan Formation (Table 4) were determined through lab process at Salahaddin University-Erbil, as 4498 – 6217 BTU/lb (or 2343 – 2499 cal/gm). These samples would be considered within the range of Brown Coal – Peat according to tables introduced by Nicholls (1968). Whereas the ASTM standard tables (Table 1) would suggest a rank below Lignite which is the lowest coal rank. Since, the values of the significant parameters of Proximate Analysis (Fixed Carbon and Gross Calorific Value) were notably low (Table 3); as compared to all standard coal ranks listed at ASTM (Table 1), hence the local samples would not indicate any rich coal-bearing rocks. Therefore, the Ultimate Analysis was not recommended for the samples of Banik coal.

4.4. Mineral Matter (MM) in Coals

In many coals or coal-like deposits, the issue of mineral content or mineral matter (MM) and its calculation were concerned for industry institutes and researchers (Vorres, 1986). Several formulae were established aiming the calculation of MM. One of the latest, possibly with figures very similar to experimentally estimated ones, was introduced by Saini *et al.* (2015); as follow:

Mineral Matter (MM) = 0.74 (Moisture %) + 1.17 (Ash %)

Using this formula, the MM values of the standards coal ranks would count for less than 6 (in Anthracite) to less than 30 (in Lignite) (Table 5). It is obvious that the contribution of mineral matter is reversely related to carbon content. Whereas, the calculated MM for the local coal-like rocks (shown in Table 6), ranged from 36.81 (in the sample of Silopi) to 64.29 (in sample from Banik). The high MM in local samples is expected with their low carbon percent (Table 6).

Table 5. Mineral Matter (MM) in Standard Coal Ranks (using formula of Saini *et al.*, 2015).

The chart below displays that Mineral Matter is reversely related to carbon content in the different coal grades.

Coal Rank (Coal Grade)	Moisture (%)	Ash (%)	Fixed Carbon (%)	Mineral Matter (0.74 Moist + 1.17 Ash)
Lignite	32.5	5.0	31.7	29.9
Sub-bituminous	20.7	3.9	44.7	19.9
H.V. Bituminous –C	11.9	8.5	42.7	18.8
H.V. Bituminous- B	4.2	6.4	58.8	10.6
H.V. Bituminous- A	3.0	2.4	58.3	5.0
M.V. Bituminous	1.4	1.8	70.8	3.1
L.V. Bituminous	0.6	7.4	73.8	9.1
Anthracite	4.2	2.4	90.3	5.9

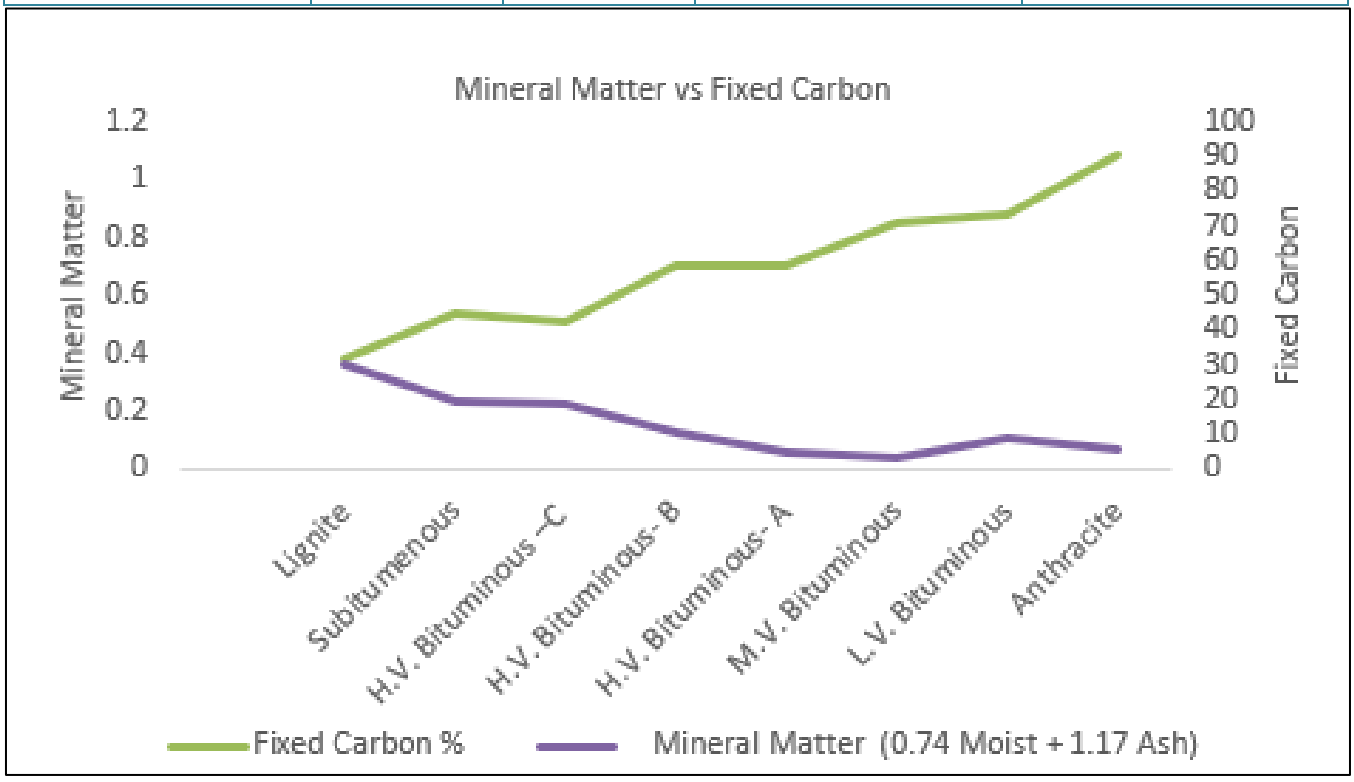

Table 6. Mineral Matter (MM) in Coal Samples (using the formula of Saini *et al.*, 2015).

The chart below displays that Mineral Matter is reversely related to carbon content in the different coal samples.

Local Coal Samples	Moisture (%)	Ash (%)	Fixed Carbon (%)	Mineral Matter (0.74 Moist + 1.17 Ash)
Banik – 1	0.4	54.7	9.4	29.9
Shiranish - 1	0.4	50.5	9.3	19.9
Shiranish - 2	6.2	37.7	9.9	18.8
Shiranish - 3	0.6	44.6	8.9	10.6
Silopi - Turkey	0.9	30.9	11.5	5.0

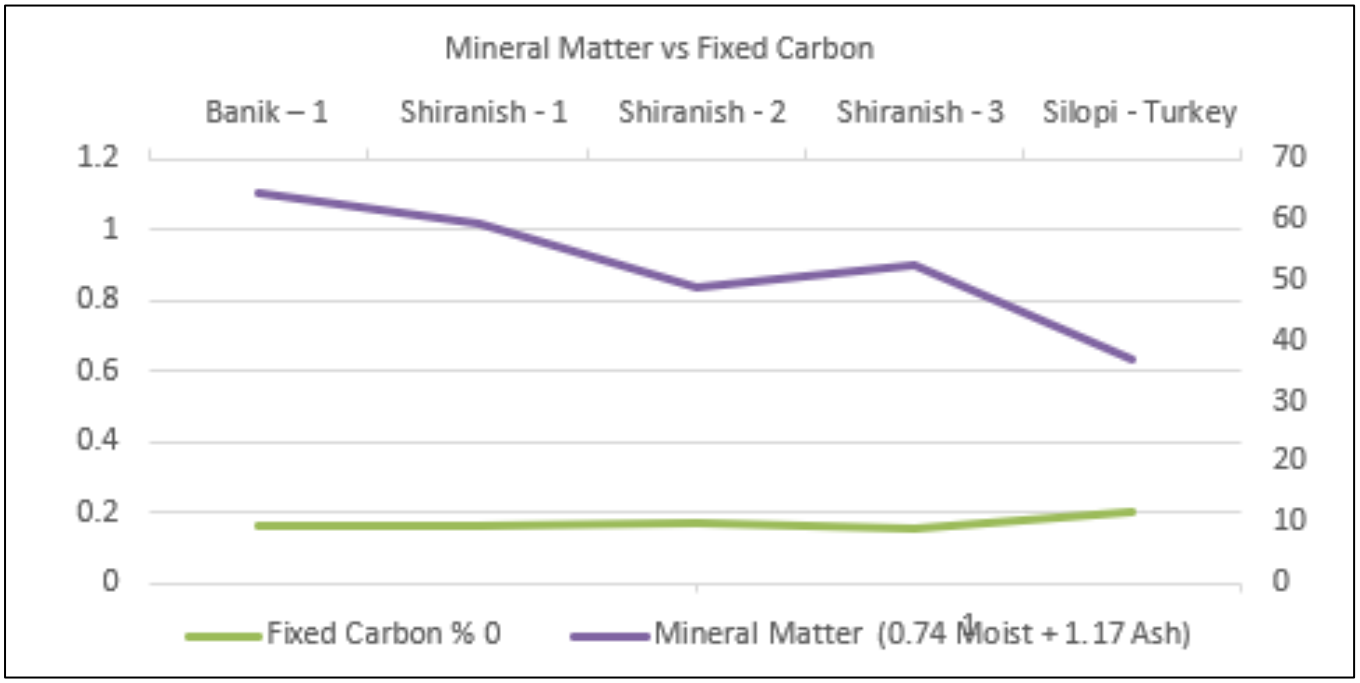

5. Conclusions

The following conclusions were reached by the present study:

1-The previous studies related to the so-called Coal Horizon in the lower part of the Naokelekan Formation referred to different terminologies such as; bitumen (migra-bitumen, pyro-bitumen), kerogen, mixture of bitumen and kerogen. These debatable components were awarded to different petrology/rock terms; bituminous carbonates (limestone and dolomite), black shale, black coal, and coaly mudstone. Some researchers also argued about the location and/or the presence of the coal horizon within the section of the Naokelekan Formation. The current study, skipping all these arguments, has focused on the chemical assessment of the concerned coal horizon using standard coal tests of ASTM.

2- The Standard Proximate Analysis of tested coal samples has displayed low fixed carbon (less than 10%), low calorific value (average: 4336-5357 BTU), and high ash content (44-54 %) indicating properties below the lowest coal rank (Lignite). These values resemble those of very poor coal types (Peat or Brown Coal).

3- The values of the main components of Proximate Analysis impose limitation on using Banik coal as an alternative source for energy, particularly when the cost of this presumed coal is compared with the rather cheap hydrocarbons (Natural Gas and Petroleum) in local energy markets.

4-The calculated Mineral Matter (MM), a new parameter for coal assessment, displayed high values (52-64 %) which are much higher than values of MM of all traditional coal ranks (5-29 %). This reflects the dominance of minerals (mainly from carbonates) associated with low carbon content.

5-The newly exposed quantitative chemical criteria (Proximate Analysis) for samples from the Coal Horizon of the Naokelekan Formation, suggest that this term should be replaced by a more realistic alternative term, such as Coal-Like Horizon. The concerned horizon resembles normal coal in appearance not in the content and heating value. Nevertheless, further studies, covering broad standard testing of samples in other sections of the Naokelekan Formation is highly recommended. This can be extrapolated to many other bitumen-rich rocks, as bitumen may have significant role even in the traditional coal grades or ranks.

Acknowledgment

The author expresses his gratitude to Ministry of Natural Resources-KRG and the former Kurdistan Geological Society for facilitating some of the tests in external labs in Turkey and Salahaddin University, Erbil, Iraq. Thanks are extended to Mr. Varoujan Sissakian from the University of Kurdistan Hewler (UKH) for reviewing the manuscript.

References

Abdula, R.A. (2016). Stratigraphy and Lithology of Naokelekan Formation in Iraqi Kurdistan-Review. *The International Journal of Engineering and Science (IJES), 5*(8), 07-17.

Abdula, R.A. (2018). *Organic petrography, mineralogy and rock-eval pyrolysis of Naokelekan Formation and generation history in the Upper Triassic-Jurassic sequences in Kurdistan Region, Iraq*. PhD thesis, Soran University, Soran, Iraq. pp. 243.

Abdula, R.A., Kolo, K., Damoulianou, M., Raftopoulou, V., Khanaqa, P. & Kalaitzidis, S. (2020). Rock-Eval analysis and organic Petrographical characterization of the Upper Jurassic Naokelekan Formation, Northern Mesopotamian Basin, Kurdistan Region-Iraq. *Bulletin of the Geological Society of Greece, 56*, 187-203.

Al-Atroshi, S.J., Sherwani, G.H. & Al-Naqshbandi, S.F. (2019). Assessment of the hydrocarbon potentiality of the Late Jurassic formations of NW Iraq: A case study based on TOC and Rock-Eval pyrolysis in selected oil-wells. *Open Geosciences* 2019; 11: 918-928.

Al-Badry, A.M.S. (2012). *Stratigraphy and geochemistry of Jurassic formations in selected sections – North Iraq*. PhD dissertation, Science College, University of Baghdad, Baghdad, Iraq. pp. 183.

ASTM (2013). ASTM D3176-15 : *Standard Practice for Ultimate Analysis of Coal and Coke.* https://www.astm.org/d3176-15.html

ASTM (2015). ASTM D3172-13 : *Standard Practice for Proximate Analysis of Coal and Coke.* https://www.astm.org/d3172-13.html

Baban, D.H. & Ahmed, S.M. (2014). Vitrinite reflectance as a tool for determining level of thermal maturity for the Upper Jurassic Naokelekan and Barsarin formations in Sargelu location, Kurdistan Region, NE Iraq: *Arabian Journal of Geosciences*, *7*(6), 2269-2277.

Balaky, S.M. (2015). Sequence stratigraphic analyses of Naokelekan Formation (Late Jurassic), Barsarin area, Kurdistan Region- Northern Iraq. *Arabian Journal of Geosciences*, 8(8), 5869–5878.

Bellen, R.C. van, Dunnington, H.V., Wetzel, R. & Morton, D.M. (1959). Lexique stratigraphique international: Paris, v. III, Asie, Fascicule 10a Iraq, pp. 333.

Farhaduzzaman, M.D. Abdullah, W.H., Aminul Islam, M.D. & Sia, S.G. (2015). Quality assessment of the Permian coals from Dighipara basin, Bangladesh based on proximate, ultimate and microscopic analyses. *Journal of Bangladesh Academy of Sciences*, 39(2), 177-194.

Fouad, S.F. (2015). Tectonic Map of Iraq, Scale 1:1000000, 3rd edition. *Iraqi Bulletin of Geology and Mining*, 11(1): 1- 8.

Jassim, S.Z. & Buday, T. (2006). Late Toarcian – Early Tithonian (Mid-Late Jurassic) Megasequence AP7. Chapter 10 in Jassim, S.Z., and Goff, J. (eds.) *Geology of Iraq*. Dolin, Prague and Moravian Museum, Brno, Czech Republic, pp. 117-123.

Nicholls, G.D. (1968). The geochemistry of coal-bearing strata. In Murchison, D. and Westoll, T.S. (editors). *Coal and coal-bearing strata*. Oliver and Boyd, Edinburgh, pp. 269-307.

Othman, R.S. (1990). *Generation, migration, and maturation of the hydrocarbons, Northern Iraq (Upper Jurassic-Lower Cretaceous)*. MSc thesis, University of Salahaddin, Erbil, Iraq, pp. 208.

Parnell, J., Ruffel, A.H., Monson, B. & Mutterlose, J. (1996). Petrography and origin of deposits at the Bentheim bitumen mine, northwestern Germany. *Mineralium Deposita,* 31, Springer–Verlag, pp. 104-112.

Saini, M.K., Srivastava, P.K. & Choudhury, N. (2015). Development of Moisture and Ash Based Correlation for the Estimation of Mineral Matter in High Ash Indian Coal. *International Journal of Clean Coal and Energy*, 4, 33-42

Salae, A.T. (2001). Stratigraphy and Sedimentology of the upper Jurassic succession, Northern Iraq. MSc thesis, University of Baghdad, Baghdad, Iraq, pp. 95.

Thomas, L. (2002). *Coal Geology*. West Sussex, England: John Wiley and Sons Ltd., pp. 384.

Vorres, K.S. (1986). Chemistry of mineral matter and ash in coal, an overview. *ACS Symposium Series, American Chemical Society*. Washington, DC, USA. Retrieved from https://pubs.acs.org/doi/pdf/10.1021/bk-1986-0301.ch001.

Review Article

A Finite-Time Speed and Direction Control for Four-Wheel Drive System

Sarkar Jawhar M Shareef [a,*], Fadhil T. Aula [b]

Department of Electrical Engineering, College of Engineering, Salahaddin University-Erbil, Erbil, KRI, Iraq

E-mail: [a] sarkar.mohammed@su.edu.krd, [b] fadhil.aula@su.edu.krd

Access this article online		
Received on: August 10, 2021	**Accepted on:** November 7, 2021	**Published on:** December 28, 2021
DOI: 10.25079/ukhjse.v5n2y2021.pp47-55	**E-ISSN:** 2520-7792	

Abstract

With the rapid use of the Four-Wheel Drive System (FWDS) worldwide, the necessity of having an adequate control system to control speed and direction in FWDS is extremely required. For this purpose, several control schemes are available in the literature to control the speed and direction in FWDS which should be fast convergence of the control, continuous control performance, and solving external disturbances. In latest years, finite-time controllers (FTC) have gained more consideration from many researchers in the control area, who have expressed applications in several procedures and systems. This research provides a major review of the FTC approaches via both input and output feedbacks for controlling FWDS.

Keywords: Finite-Time Controller, FTC, Four-Wheel Drive System, FWDS, Speed and Direction Control.

1. Introduction

The concern of the global warming issues for using fossil fuels is very high. The combustion engines in cars that use these traditional fossil fuels make major car manufacturers transfer to produce electrical vehicles (EV). EVs are considered clean and friendly to the environment. EV is required not just to operate on batteries but also is needed to be smart. Four-wheel drive systems (FWDS) are considered smart vehicles which include many complex controllers to drive them more efficiently and safely on the roads.

The major problems of FWDSs are the need for advanced control systems to control the speed and direction of their four wheels continuously. Several control methods have been used in recent years to achieve the best control solutions.

The core point of the designed control method is the assurance of the rapid convergence of the system reactions to zero with a finite settle downtime. When a bad controller is used, the required range of the controlled speed for FWDS may be more than the velocity or acceleration upper bound limitations that the motors can produce. Then the control's instruction is not reliable, which leads to poor act and the system will be unstable(Runhua Wang et al., 2021).

One of the control methods used in a four-wheel drive system is a smooth control method, but the convergence performance is not perfect, and the smooth control method is not an optimal time controller (Ariff et al., 2015; Shuai et al., 2014; Rongrong Wang et al., 2015). On the other hand, a slide mode control has anti-disturbance performance and fast convergence. But it is asymptotically stable and not continuous. This may lead to being chatter in a closed-loop feedback system (Ginoya et al., 2014; Li et al., 2017). Due to the simplicity of the Proportional Integral Derivative (PID) structure, it is one of the most used control methods for FWDSs. But PID controller has limitations when they are tuned to deal with specific conditions and if these conditions are changed, the performance will be affected. Also, the PID controllers do not work for nonlinear systems (Jeong et al., 2017; J. Wang, 2020; Zhou et al., 2018). Artificial Neural networks (ANN) are the forming of the human mind which are used widely in control fields. The major difficulty of ANN is working as a black box. It does not explain the way that the solution was done, and hence, decreases the belief

in the network. (Chen et al., 2020; Kortylewski et al., 2021; Kraft et al., 2019; Tu, 1996). In contrast, the finite-time controller in comparison to the mentioned controllers promises better performance.

The FTC is popular due to its excessive tracking precision, fast convergence, and powerful disturbance refusal. Due to advantages of Finite-time controllers over other controllers in which they have excessive tracking precision, fast convergence, and powerful disturbance refusal, lead them to a widely being used in different control areas. In latest years, FTCs have gained more consideration from many researchers in the control area, who have expressed applications in several procedures and systems (Fang et al., 2019; Meng et al., 2018; F. Wang et al., 2019)

This research aims to review previous works in the concept of finite-time approaches in the area of the controller performance of FWDSs. This paper includes the following sections: The introduction is presented in section one. Section two covers the four-wheel drive system mathematical model. Finite-time controller details in section three and section four covers finite-time controllers in different areas of applications. Finally, the conclusion is given in section five.

2. Four-Wheel Drive System Mathematical Model

FWDS has insignificant benefits in terms of dynamic performance, energy effectiveness, and active safety. Additionally, the torque of the FWDS EV can be individually controlled and easily determined. Because the EV's velocity is an essential variable in dynamics control and stability, the estimation of EV's velocity is done in general. Thus, there is no doubt that estimating the accuracy of the EV's velocity is necessary for reaching the high performance of the EV controller(Xin et al., 2017) (Meng et al., 2019).

In FWDS, when a car steers, all four wheels turn at the same time. The lateral motion and the yaw of the FWDS can be controlled by both front and rear wheels, which also decreases the steering force delay and controls the motion trajectory (Meng et al., 2019). Figure 1 demonstrates the FWDS dynamic model.

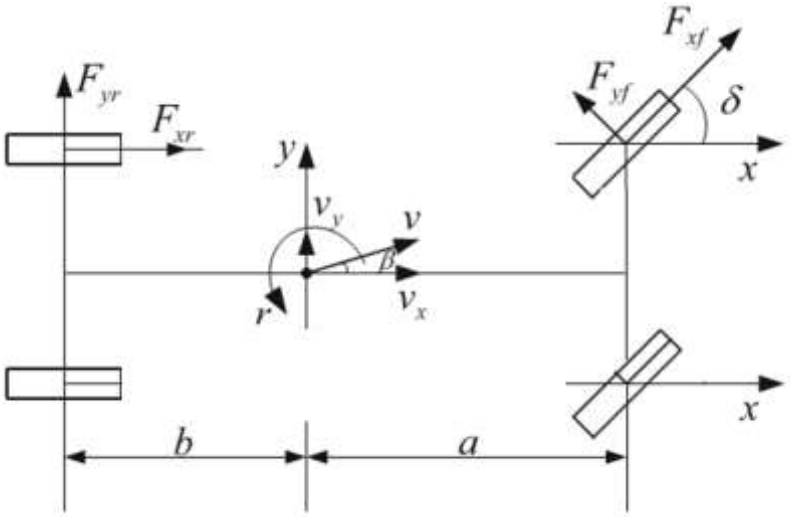

Figure 1. FWDS Dynamic Model (Ding & Sun, 2017).

Where δ is the steering angle ($\delta \geq 0$ for anticlockwise and $\delta < 0$ for clockwise), β is the EV sideslip angle; a and b are the distances between the center of gravity and the front axle and rear axle. V is the velocity of EV; v_x represents the longitudinal velocity of EV; v_y indicates the lateral velocity of EV. Fxf, Fyf, Fxr and Fyr are the front and rear wheels tire forces.

The controlling of the speed and direction by both the front and rear wheels and controlling the motion trajectory can be done with the use of FWDS.

The lateral motion can be described as:

$$m\left(\dot{v}_y + r.v_x\right) = -\frac{2}{v_x}(aK_f - bK_r)r + 2K_f\delta - 2(K_f - K_r)\beta \quad (1)$$

and the motion of yaw stated as:

$$I_z\dot{r} = 2aK_f\delta - \frac{2}{v_x}(a^2K_f - b^2K_r)r + 2(aK_f - bK_r)\beta \quad (2)$$

where K_f and K_r denotes the front and rear wheels cornering stiffnesses respectively (Ding & Sun, 2017).

3. Finite-Time Controller

The idea of finite-time control dates back to the Fiftieth of last century when the idea of finite-time stability (FTS) was introduced by Kamenkov (Kamenkov, 1953). In 1965, Weiss and Infante (Weiss & Infante, 1965) published a very comprehensive analysis of FTS for nonlinear systems, with the perception of finite-time stability. Soon thereafter, Weiss and Infante published an addition of FTS to nonlinear systems in the presence of perturbation signals and developed the idea of Bounded Input and Bounded Output (BIBO) finite-time stability (WEISS & INFANTE, 1967). Nowadays, generally BIBO known as finite time-bounded (FTB) stability (F. Amato et al., 2015). (Wu, 1969) protracted several of the present analysis outcomes on Finite-Time Stability for continuous-time to discrete-time systems.

In 1997, Dorato, Abdallah, and Famularo (Dorato et al., 1997) presented a study on the strong Finite-Time Stability proposal for linear systems. They used linear matrix variations to find state-feedback control rules. Additional linear matrix variations based on design outcomes for linear systems were existing in Amato *et al.* (F. C. D. Amato, 2003). In 2002, Abdallah *et al.* proposed methods which are depending on statistic learning for Finite-Time Stability design with static output feedback. Lately, discrete-time FTS design methods was used in the control of ATM nets and systems with net-control (Mastellone et al., 2006).

(Sun et al., 2017) suggested a new control strategy to unify the structure of Lyapunov utilities for a finite-time stability statement. The design of an FTC was done for steering of four-wheel of an EV to improve the stability of the EV (Meng et al., 2018). A finite-time controller was designed to stabilize the electric vehicle in case a tire had blown out (Meng et al., 2019). (Lin et al., 2019) examined the bounded finite-time of a neutral type switched systems with delay in time-vary.

A system is thought to be finite-time stable when bounded with the initial condition, its state does not overdo a definite threshold during an identified period (Osiris et al., 2018). The finite-time control problem concerns the design of a linear controller which guarantees the FTS of the closed-loop system. (Francesco Amato et al., 2006)

The next explanations deal with several FTC difficulties.

The definition of FTS: Given positive scalars c_1, c_2, T, with $c_1 < c_2$, and a positive definite symmetric matrix function $\Gamma(t)$ is between $[0, T]$, the time-varying linear system:

$$\dot{x}(t) = A(t)x(t), \qquad x(0) = x_0 \tag{3}$$

is supposed to be finite-time stable (FTS) with respect to $(c_1, c_2, T, \Gamma(t))$, if

$$x_0^T \Gamma(0) x_0 \leq c_1 \Rightarrow x(t)^T \Gamma(t) x(t) < c_2 \ \forall t \in [0, T] \tag{4}$$

3.1. FTC via State Feedback:

For the time changes the linear system

$$\dot{x}(t) = A(t)x(t) + B(t)u(t) + G(t)w(t), x(0) = x_0 \tag{5}$$

where $w(t)$ is the disturbance, $u(t)$ is the control input. A state feedback controller in the form

$$u(t) = K(t)x(t) \tag{6}$$

The closed-loop system is found by connecting (3) and (4)

$$\dot{x}(t) = \big(A(t) + B(t)K(t)\big)x(t) + G(t)w(t), \ x(0) = x_0 \tag{7}$$

3.2. FTC via Output Feedback:

Assume the system with linear time-varying

$$\dot{x}(t) = A(t)x(t) + B(t)u(t) + G(t)w(t), x(0) = x_0 \tag{8}$$

$$y(t) = C(t)x(t) + H(t)w(t) \tag{9}$$

A dynamic output feedback controller in the form

$$\dot{x}_c(t) = A_K(t)x_c(t) + B_K(t)y(t) \tag{10}$$

$$u(t) = C_K(t)x_c(t) + D_K(t)y(t) \tag{11}$$

where $x_c(t)$ has the similar dimension of $x(t)$, such that the closed-loop system is initiated by connecting (8), (9), (10), and (11).

4. Finite-Time Control: Approaches and Review

This section discusses serval papers that show the use of finite-time controllers in different areas of applications.

Starting from the spacecraft area; A finite time neural scheme control is used by (Tao et al., 2021) for spacecraft with attitude tracking presentation using finite-time performance function to guarantee parametric uncertainty, external disturbance, unmeasurable flexible vibration, and the saturation of actuator. The finite-time controller guarantees that errors of tracking can be converged to a given range within a determined time, which is not dependent on the initial conditions. The resultant control is then protracted by a neural network compensator to remove the disturbance and

overcome the unlimited actuator saturation. Finally, the results and the numerical simulations prove the stability, effectiveness, and robustness of the used controller.

For motor control; the authors of (Du et al., 2021) designed a finite-time controller to resolve the speed regulation control problem of a permanent magnet synchronous motor under the control input constraints. The work of this paper was in two aspects. First, abounded finite-time feedback control method is designed to develop the scheme and sidestep the saturation limitation problem. The second part is to develop the scheme's disturbance rejection capability. The proposed finite-time control-based speed regulation controller scheme is shown in Figure 2. The authors claimed that their results show the effectiveness in disturbance rejection.

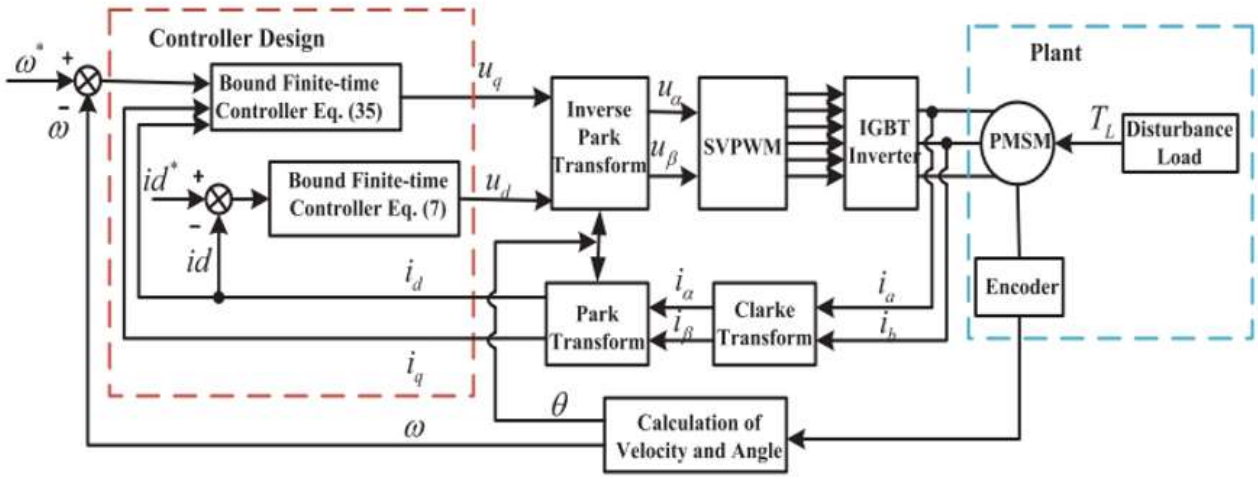

Figure 2. Finite-Time Control Based Speed Regulation Controller (Du et al., 2021).

An adaptive recursive terminal sliding mode (ARTSM) controller was recommended in (Shao et al., 2020). The recommended controller assured that the tracking error converges to zero in a finite time. Additionally, by choosing a suitable initial value for the integral controller component, the proposed controller was forced to begin on the sliding surface at the starting time such that the completion time is decreased. Analysis of stability was also showed the verification of the convergence of finite-time and without error of tracking of the closed-loop scheme in the suggested control system. Experiment outcomes demonstrated the efficiency of the proposed control system in terms of reduction of tracking errors and fast disturbance refusal as authors claimed in their work.

The main aim of the work (González-García et al., 2021) was to reduce the power that was consumed by the controller of the Unmanned Underwater Vehicles BlueROV2 model. The reduction was done by implementing a model-free high-order sliding-mode finite-time controller as shown in Figure 3. Results showed that the finite-time convergence to zero faster than other controllers such as PID, Feedback Linearization, and Lyapunov-Based. So, the proposed finite-time controller was up to 50% in the power consumption reduction when compared to other mentioned controllers.

The authors of (Mei et al., 2020) have improved an FTC for various integrator nonlinear systems that are subjected to saturated input control of an agricultural vehicle straightforward line tracking scheme. A saturated FTC with an adaptable saturation level was considered by imposing a series of saturation tasks on the unsaturated control system as shown in Figure 4. The mathematical evidence indicated that with the presence of the control system, the states of the system will be determined to a specified region which was driven by the level of saturation. The outcomes from simulations of the paper showed that the saturated output could be adjusted by using this finite-time controller when it is unsaturated.

In (Liang et al., 2021) an FTC was suggested for turbo-generators in the existence of limited disturbances and unidentified scheme dynamics. The constant boundaries on the system states and multi-terminal sliding mode were suggested to improve the transient performance. Then, the uncertainties of the scheme were solved by the neural network. Similarly, the essential free of chatter property can be reached by the margin layer. In conclusion, the output of the finite-time stability in the system was verified by using Lyapunov analysis, and simulation outcomes had exposed that the suggested control system could improve both stable accuracy and transient stability in the existence of unidentified external disturbances.

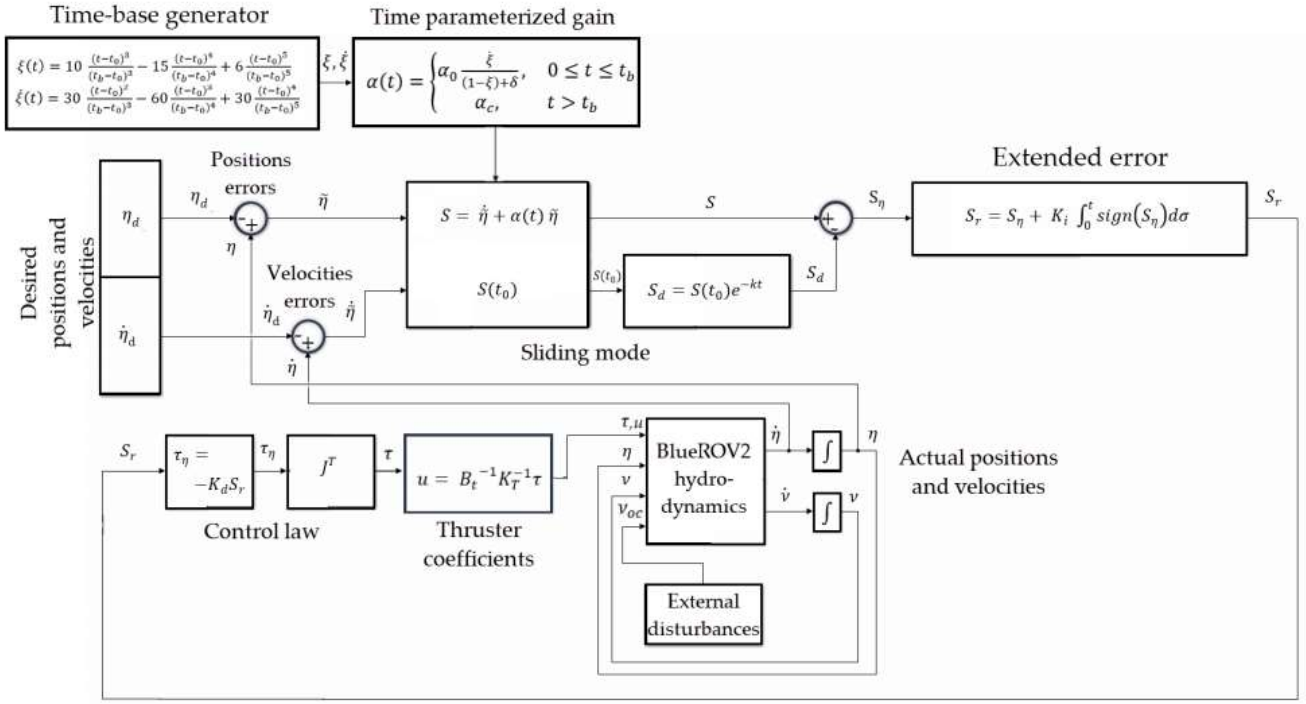

Figure 3. Model-Free High-Order Sliding-Mode Finite-Time Controller (González-García et al., 2021).

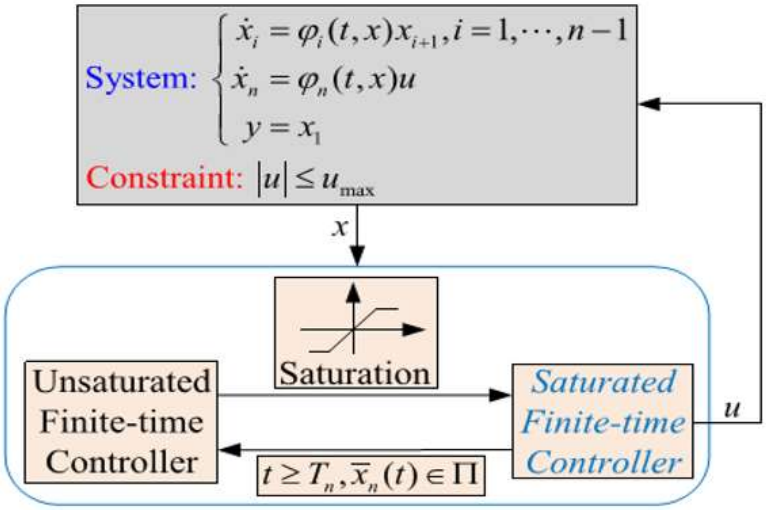

Figure 4. Block Plan Of Control System (Mei et al., 2020).

The article (Nguyen et al., 2019) demonstrated a fuzzy problem of crane structure and boundedness FTS via the sliding mode control technique. Because of the robust coupling of control input, the fuzzy method was applied to linearize the crane structure. Swinging of crane plates and hook which were due to the outer disturbances of the friction and air resistance were solved by using boundedness FTS sliding mode control technique. The simulation results showed the effectiveness of the sliding mode controller technique with finite-time procedure over other present procedures such as similar proportional integral differential (PID) controller, developed neural network procedure, and linear quadratic regulator (LQR).

The authors in (Runhua Wang et al., 2021) proposed an adapted visual tracking control for a mobile robot using a single attached camera and by choosing proper control parameters for both speed and accelerate saturation limitations could be certain. The authors proposed a first-order filter speed control system to guarantee the speed halts at the upper boundary. By using the FTC theory, the acceleration-level control system was improved to track the speed input in a certain time. The control block diagram is shown in Figure 5. In this work, the authors used a Pioneer-3DX type mobile

robot, a DMK23G618 model camera for testing the proposed controller. Experimental outcomes showed the efficiency of the suggested control system in saturation limitations.

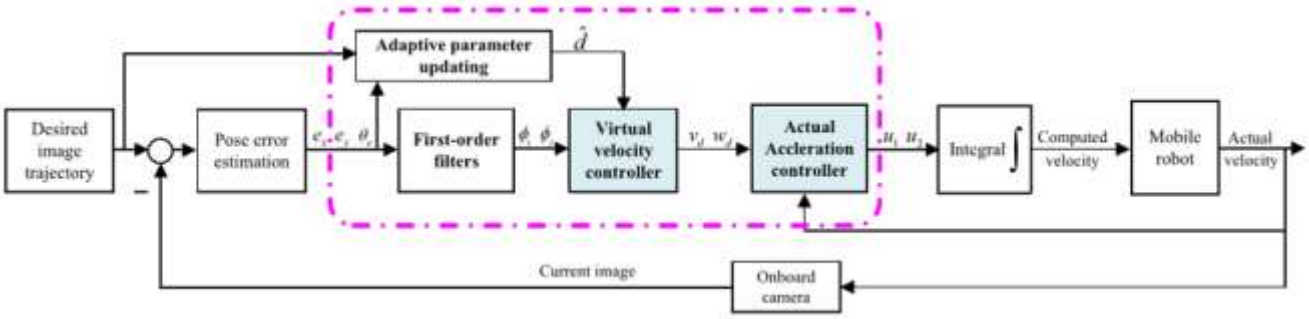

Figure 5. Tracking Control Diagram (Runhua Wang et al., 2021).

A control scheme combining impedance and finite time was proposed by (Hu et al., 2020) in which they used position tracking for robot movement in uncertain environments. The control structure was separated into two integral loops: an outer loop was for controlling the impedance force in order to remove the error of force tracking, while an inner loop was for controlling the position tracking. A control strategy for controlling the robot environment is shown in Figure 6. The Matlab/Simulink simulation results showed that the proposed control can achieve a good tracking effect in all uncertain environments.

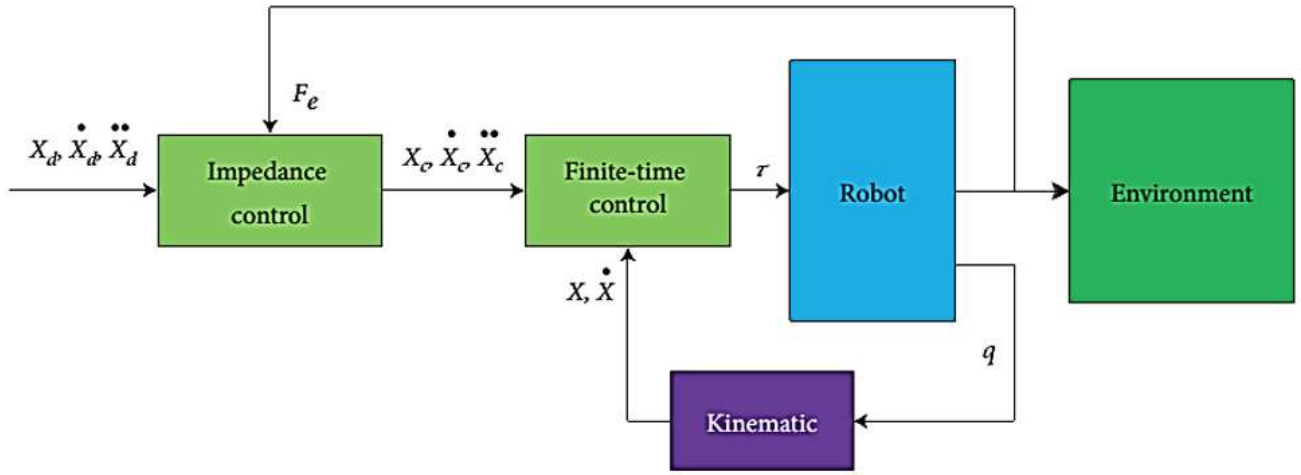

Figure 6. Control Block Diagram (Hu et al., 2020).

The article (Zheng et al., 2019) proposed an analysis of the stability and an improved robust FTC for a mobile robot system with problems of undefined angular and linear speeds and time-changing limited disturbance. The article (Zheng et al., 2019) proposed an analysis of stability and an improved robust FTC for a mobile robot system which had problems of the unmeasurable angular and linear velocities, and time-varying bounded disturbance. They also proposed a solution for solving these problems by using state feedback control laws with a reduction in a sharp change of initial values in state variables. The closed-loop scheme was asymptotically stable and the state errors were converged to modifiable limits by using the Lyapunov–Krasovskii approach. The simulation was done to illustrate the efficacy of the suggested approach.

In four-wheel drive systems, several researchers have discussed them. The authors in (Meng et al., 2018) designed a finite-time convergence controller to control an EV run by four-wheel motors to eliminate uncertainties and keep the sideslip angle to be zero value. The simulation was done by the Carsim software and MATLAB/Simulink to prove that the considered Four-Wheal System (FWS) finite-time convergence control system could track the chosen model, reduce some uncertainties, and retain the sideslip angle to be zero value. The simulation results and from the comparison to the slide mode controller technique showed that the proposed technique has a good control result for the active FWS

of an electrical vehicle. The article (Meng et al., 2021) recommended a lane-tracking controller using a non-smooth finite-time control technique. A lane-tracking control prototype was built and a tracking scheme and error weight superposition technique to track error computing for the lane-tracking control were suggested by depending on the given information of the used lane line. The construction of the lane-tracking control is demonstrated in Figure 7. A non-smooth FTC was built for the lane-tracking with the use of the direct Lyapunov technique. The simulations outcomes exposed that the suggested controller is better than the PID controller to keep the vehicle moving in the wanted lane with the different kinds of roads (straight, constant curvature, varied curvature, and S-bend). The work (Meng et al., 2019) studied the problem of a tire blowout controller via output feedback for an EV that is driven by four-wheel motors. To report the problems in approximating the unmeasurable state, unidentified factors, and disturbances for the electric vehicle, a finite-time observer was presented. The tire blowout simulation was done for vehicle speeds: 60 km/h, 80 km/h, and 120 km/h, respectively, to show the validity of the designed controller. The simulations results showed that the validation of the proposed finite-time output feedback controller for the Electric Vehicle Driven by Four Wheels Independently (EV-DFWI) tire blowout control.

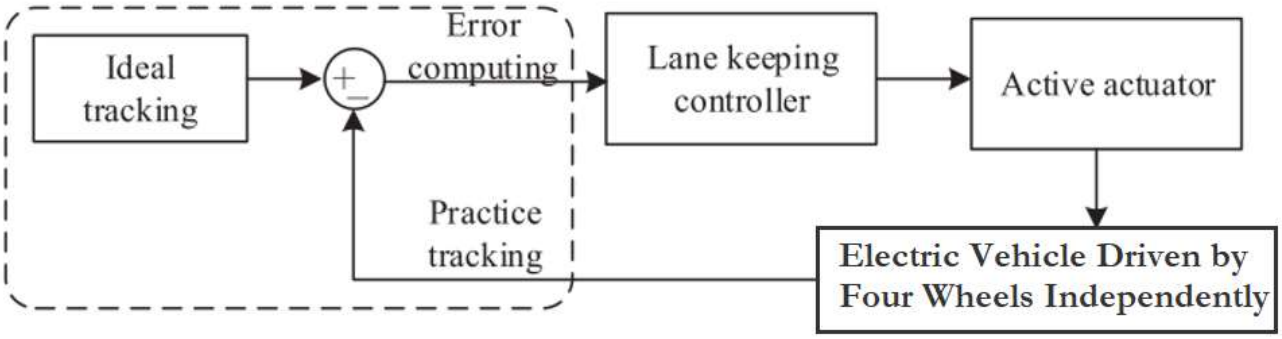

Figure 7. Construction of the Lane-Tracking Control (Meng et al., 2021).

5. Conclusion

To control the speed and direction of the four-wheel drive system serval controller schemes are available to implement. The smooth control method is one of the good methods but its convergence act is not faultless and not an optimal time controller. While the slide mode control has anti-disturbance performance and fast convergence. But the slide mode is asymptotically stable and not continuous that could cause the chattering in the closed-loop feedback system. The PID control is one of the most applied controlling strategies for FWDSs due to their simple structure. But the PID controller does not work for nonlinear systems. ANN is also used widely in control fields but it works as a black box. It does not give an explanation of the way how the solution has been done. The controller techniques for controlling the speed and direction of the four-wheel drive system should be fast convergence of the control, continuous control performance, and solve the external disturbances. These can be done by using the Finite-time controller approach.

References

Amato, F., Ariola, M., Abdallah, C.T., Dorato, P. (August-September 1999). *Dynamic output feedback finite-time control of LTI systems subject to parametric uncertainties and disturbances*. 1999 European Control Conference (ECC). IEEE. Karlsruhe, Germany. doi: 10.23919/ecc.1999.7099716.

Amato, F., Ariola, M., Abdallah, C. T., & Dorato, P. (2015). Dynamic output feedback finite-time control of LTI systems subject to parametric uncertainties and disturbances. *European Control Conference, ECC 1999 - Conference Proceedings*, *37*, 2596–2601. https://doi.org/10.23919/ecc.1999.7099716

Amato, F. C. D. (2003). Necessary and Sufficient Conditions for. *Integration The Vlsi Journal*, *174*, 544–548.

Amato, Francesco, Ariola, M., Carbone, M., & Cosentino, C. (2006). Finite-time control of linear systems: A survey. *Systems and Control: Foundations and Applications*, *9780817643836*, 195–213. https://doi.org/10.1007/0-8176-4470-9_11

Ariff, M. H. M., Zamzuri, H., Nordin, M. A. M., Yahya, W. J., Mazlan, S. A., & Rahman, M. A. A. (2015). Optimal control strategy for low speed and high speed four-wheel-active steering vehicle. *Journal of Mechanical Engineering and Sciences*, *8*(June), 1516–1528. https://doi.org/10.15282/jmes.8.2015.26.0148

Chen, J., Su, J., & Li, J. (2020). Self-Coupling Black Box Model of a Dynamic System Based on ANN and Its Application. *Mathematical Problems in Engineering*, *2020*. https://doi.org/10.1155/2020/5724831

Ding, S., & Sun, J. (2017). Direct yaw-moment control for 4WID electric vehicle via finite-time control technique. *Nonlinear Dynamics*, *88*(1), 239–254. https://doi.org/10.1007/s11071-016-3240-0

Dorato, P., Abdallah, C. T., & Famularo, D. (1997). Robust finite-time stability design via linear matrix inequalities. *Proceedings of the IEEE Conference on Decision and Control*, *2*(December), 1305–1306. https://doi.org/10.1109/cdc.1997.657637

Du, H., Wen, G., Cheng, Y., & Lu, J. (2021). Design and Implementation of Bounded Finite-Time Control Algorithm for Speed Regulation of Permanent Magnet Synchronous Motor. *IEEE Transactions on Industrial Electronics*, *68*(3), 2417–2426. https://doi.org/10.1109/TIE.2020.2973904

Fang, L., Ma, L., Ding, S., & Zhao, D. (2019). Finite-time stabilization for a class of high-order stochastic nonlinear systems with an output constraint. *Applied Mathematics and Computation*, *358*, 63–79. https://doi.org/10.1016/j.amc.2019.03.067

Ginoya, D., Shendge, P. D., & Phadke, S. B. (2014). Sliding mode control for mismatched uncertain systems using an extended disturbance observer. *IEEE Transactions on Industrial Electronics*, *61*(4), 1983–1992. https://doi.org/10.1109/TIE.2013.2271597

González-García, J., Narcizo-Nuci, N. A., García-Valdovinos, L. G., Salgado-Jiménez, T., Gómez-Espinosa, A., Cuan-Urquizo, E., & Cabello, J. A. E. (2021). Model-free high order sliding mode control with finite-time tracking for unmanned underwater vehicles. *Applied Sciences (Switzerland)*, *11*(4), 1–22. https://doi.org/10.3390/app11041836

Hu, H., Wang, X., & Chen, L. (2020). Impedance with Finite-Time Control Scheme for Robot-Environment Interaction. *Mathematical Problems in Engineering*, *2020*. https://doi.org/10.1155/2020/2796590

Jeong, J. H., Lee, D. H., Kim, M., Park, W. H., Byun, G. S., & Oh, S. W. (2017). The study of the electromagnetic robot with a four-wheel drive and applied I-PID system. *Journal of Electrical Engineering and Technology*, *12*(4), 1634–1640. https://doi.org/10.5370/JEET.2017.12.4.1634

Kamenkov, G. (1953). Stability of motion over a finite interval of time. *Journal of Applied Math. and Mechanics*, *17*(2), 529–540.

Kortylewski, A., Liu, Q., Wang, A., Sun, Y., & Yuille, A. (2021). Compositional Convolutional Neural Networks: A Robust and Interpretable Model for Object Recognition Under Occlusion. *International Journal of Computer Vision*, *129*(3), 736–760. https://doi.org/10.1007/s11263-020-01401-3

Kraft, S., Causse, J., & Martinez, A. (2019). Black-box modelling of nonlinear railway vehicle dynamics for track geometry assessment using neural networks. *Vehicle System Dynamics*, *57*(9), 1241–1270. https://doi.org/10.1080/00423114.2018.1497186

Li, H., Shi, P., & Yao, D. (2017). Adaptive Sliding-Mode Control of Markov Jump Nonlinear Systems with Actuator Faults. *IEEE Transactions on Automatic Control*, *62*(4), 1933–1939. https://doi.org/10.1109/TAC.2016.2588885

Liang, Q., Yang, Q., Meng, W., & Li, Y. (2021). Adaptive finite-time control for turbo-generator of power systems with prescribed performance. *Asian Journal of Control*, *February*, 1–12. https://doi.org/10.1002/asjc.2553

Lin, X., Yang, Z., & Li, S. (2019). Finite-time boundedness and finite-time weighted L2-gain analysis for a class of neutral type switched systems with time-varying delays. *International Journal of Systems Science*, *50*(9), 1703–1717. https://doi.org/10.1080/00207721.2019.1622816

Mastellone, S., Dorato, P., & Abdallah, C. T. (2006). Finite-time stability for nonlinear networked control systems. *Systems and Control: Foundations and Applications*, *9780817643836*, 535–553. https://doi.org/10.1007/0-8176-4470-9_29

Mei, K., Ma, L., He, R., & Ding, S. (2020). Finite-time controller design of multiple integrator nonlinear systems with input saturation. *Applied Mathematics and Computation*, *372*. https://doi.org/10.1016/j.amc.2019.124986

Meng, Q., Qian, C., & Sun, Z. Y. (2019). Finite-time stability control of an electric vehicle under tyre blowout. *Transactions of the Institute of Measurement and Control*, *41*(5), 1395–1404. https://doi.org/10.1177/0142331218780967

Meng, Q., Sun, Z. Y., & Li, Y. (2018). Finite-time Controller Design for Four-wheel-steering of Electric Vehicle Driven by Four In-wheel Motors. *International Journal of Control, Automation and Systems*, *16*(4), 1814–1823. https://doi.org/10.1007/s12555-017-0509-0

Meng, Q., Zhao, X., Hu, C., & Sun, Z. Y. (2021). High velocity lane keeping control method based on the non-smooth finite-time control for electric vehicle driven by four wheels independently. *Electronics (Switzerland)*, *10*(6). https://doi.org/10.3390/electronics10060760

Nguyen, V. T., Yang, C., Du, C., & Liao, L. (2019). Design and implementation of finite time sliding mode controller for fuzzy overhead crane system. *ISA Transactions*. https://doi.org/10.1016/j.isatra.2019.11.037

Osiris, O., Villegas, V., Nandayapa, M., & Soto, I. (2018). Advanced topics on computer vision, control and robotics in mechatronics. In *Advanced Topics on Computer Vision, Control and Robotics in Mechatronics*. Springer Verlag. https://doi.org/10.1007/978-3-319-77770-2

Shao, K., Zheng, J., Huang, K., Wang, H., Man, Z., & Fu, M. (2020). Finite-Time Control of a Linear Motor Positioner Using Adaptive Recursive Terminal Sliding Mode. *IEEE Transactions on Industrial Electronics*, *67*(8), 6659–6668. https://doi.org/10.1109/TIE.2019.2937062

Shuai, Z., Zhang, H., Wang, J., Li, J., & Ouyang, M. (2014). Lateral motion control for four-wheel-independent-drive electric vehicles using optimal torque allocation and dynamic message priority scheduling. *Control Engineering Practice*, *24*(1), 55–66. https://doi.org/10.1016/j.conengprac.2013.11.012

Sun, Z. Y., Yun, M. M., & Li, T. (2017). A new approach to fast global finite-time stabilization of high-order nonlinear system. *Automatica*, *81*, 455–463. https://doi.org/10.1016/j.automatica.2017.04.024

Tao, J., Zhang, T., & Liu, Q. (2021). Novel finite-time adaptive neural control of flexible spacecraft with actuator constraints and prescribed attitude tracking performance. *Acta Astronautica*, *179*, 646–658. https://doi.org/10.1016/j.actaastro.2020.10.010

Tu, J. V. (1996). Advantages and disadvantages of using artificial neural networks versus logistic regression for predicting medical outcomes. *Journal of Clinical Epidemiology*, *49*(11), 1225–1231. https://doi.org/10.1016/S0895-4356(96)00002-9

Wang, F., Liu, Z., Zhang, Y., & Chen, C. L. P. (2019). Adaptive finite-time control of stochastic nonlinear systems with actuator failures. *Fuzzy Sets and Systems*, *374*, 170–183. https://doi.org/10.1016/j.fss.2018.12.005

Wang, J. (2020). Application of pid algorithm in drive fault-tolerant control of four-wheel drive electric vehicle. *International Journal of Mechatronics and Applied Mechanics*, *1*(8). https://doi.org/10.17683/ijomam/issue8.29

Wang, Rongrong, Hu, C., Wang, Z., Yan, F., & Chen, N. (2015). Integrated optimal dynamics control of 4WD4WS electric ground vehicle with tire-road frictional coefficient estimation. *Mechanical Systems and Signal Processing*, *60*, 727–741. https://doi.org/10.1016/j.ymssp.2014.12.026

Wang, Runhua, Zhang, X., & Fang, Y. (2021). Visual tracking of mobile robots with both velocity and acceleration saturation constraints. *Mechanical Systems and Signal Processing*, *150*, 107274. https://doi.org/10.1016/j.ymssp.2020.107274

Weiss, L., & Infante, E. F. (1965). on the Stability of Systems Defined Over a Finite Time Interval. *Proceedings of the National Academy of Sciences*, *54*(1), 44–48. https://doi.org/10.1073/pnas.54.1.44

WEISS, L., & INFANTE, E. F. (1967). Finite Time Stability Under Perturbing Forces and on Product Spaces. *IEEE Transactions on Automatic Control*, *AC-12*(1), 54–59. https://doi.org/10.1109/TAC.1967.1098483

Wu, S. H. (1969). Stability of discrete systems over a finite interval of time. *International Journal of Control*, *9*(6), 679–693. https://doi.org/10.1080/00207176908905789

Xin, X., Zhang, W., Shen, C., & Zheng, H. (2017). Control strategy of four-wheel independent drive electric vehicle based on vehicle velocity estimation and switchover. *Transactions of the Institute of Measurement and Control*, *39*(7), 965–975. https://doi.org/10.1177/0142331215625767

Zheng, W., Wang, H., Sun, F., Li, X., & Wen, S. (2019). Finite-time control of mobile robot systems with unmeasurable angular and linear velocities via bioinspired neurodynamics approach. *Applied Soft Computing Journal*, *85*. https://doi.org/10.1016/j.asoc.2019.105753

Zhou, H., Jia, F., Jing, H., Liu, Z., & Güvenç, L. (2018). Coordinated Longitudinal and Lateral Motion Control for Four Wheel Independent Motor-Drive Electric Vehicle. *IEEE Transactions on Vehicular Technology*, *67*(5), 3782–3790. https://doi.org/10.1109/TVT.2018.2816936

Research Article

The Status of Mosul Dam, NW of Iraq

Varoujan K. Sissakian [1, a, *], Nasrat Adamo [2, b], Nadhir Al-Ansari [3, c], Jan Laue [3, d], Aayda D. Abdulahad [4, e]

[1] Department of Natural Resources Engineering and Management, School of Science and Engineering, University of Kurdistan Hewlêr, Erbil, KRI, Iraq.
[2] Dam Engineering Consultant, Lulea, Sweden
[3] Department of Civil, Environmental and Natural Resources Engineering, Lulea University of Technology, Lulea, Sweden
[4] Retired Chief Geologist, Erbil, KRI, Iraq

E-mail: [a] f.khajeek@ukh.edu.krd, [b] nasrat.adamo@yahoo.com, [c] nadhir.alnnsari@ltu.se, [d] Jan.laue@ltu.se, [e] iyda1955@yahoo.com

Access this article online		
Received on: August 30, 2021	**Accepted on:** September 27, 2021	**Published on:** December 28, 2021
DOI: 10.25079/ukhjse.v5n2y2021.pp56-61	**E-ISSN:** 2520-7792	

Abstract
Mosul Dam is located in the northwestern part of Iraq impounding the Tigris River; about 60 km north of Mosul city. This project is multipurpose project; to provide water for irrigation, flood control and hydropower generation. The dam is 113 m high and 3650 m long including the spillway. The dam is earth fill type with a mud core. The dam was designed to impound 11.11 km^3 because it is based and underlain by gypsum beds alternated with limestone and marl. Therefore, it is planned to use continuous grouting to fill the karst caverns. The used quantity exceeded 95000 tons of solid grouting materials since 1986 up to 2014. After all, is the dam safe? The details are given in the current article.

Keywords: Foundation, Grouting, Gypsum, Karstification, Mosul Dam.

1. Introduction

Mosul dam is an Earth-fill dam constructed to impound the Tigris River in the northwestern part of Iraq, 60 km northwest of Mosul city (Figure 1a). It is the largest dam in Iraq with clay core, its height is 113 m and length is 3650 m (Iraqi Ministry of Water Resources, 2012). The total cost of the dam was 2.6 billion US$. A general view of the dam is shown in Figure 1b. The maximum, normal and dead storage levels of its reservoir are 335, 330 and 300 m (a.s.l.), respectively. The dam was designed to impound 11.11 x10 ^{9} m of water at normal operation level. The construction of the dam started on January 25th, 1981 and completed on 24th July 1986 (Al-Ansari *et al.*, 2015a).

The aim of this article is to give a brief review about Mosul Dam and to discuss its safety. The authors are well acquainted with the history of Mosul dam; they have contributed in an International Conference held in Stockholm, Sweden in 2016 by the Luleå University of Technology (https://www.ltu.se/cms_fs/1.148962!/file/Very%20Final%20Mosul%20Dam%20Workshop.pdf).

2. Geological Setting

The geological setting of Mosul Dam site and reservoir area is briefed hereinafter based on Sissakian and Fouad (2012). Mosul Dam is constructed parallel to the axis of Butmah East anticline which has E – W trend with steep southern limb. Karst forms are well developed, especially in gypsum rocks in form of sinkholes. The exposed rocks in the dam site and reservoir area belong to two main formations, these are:1) Euphrates Formation (Lower Miocene) consists of limestone and dolostone beds with soft marl beds, and 2) Fatha Formation (Middle Miocene) consists of two members

(Lower and Upper). Both members consist of cyclic sediments starting with soft green marl, hard limestone, and hard gypsum (Figure 2).

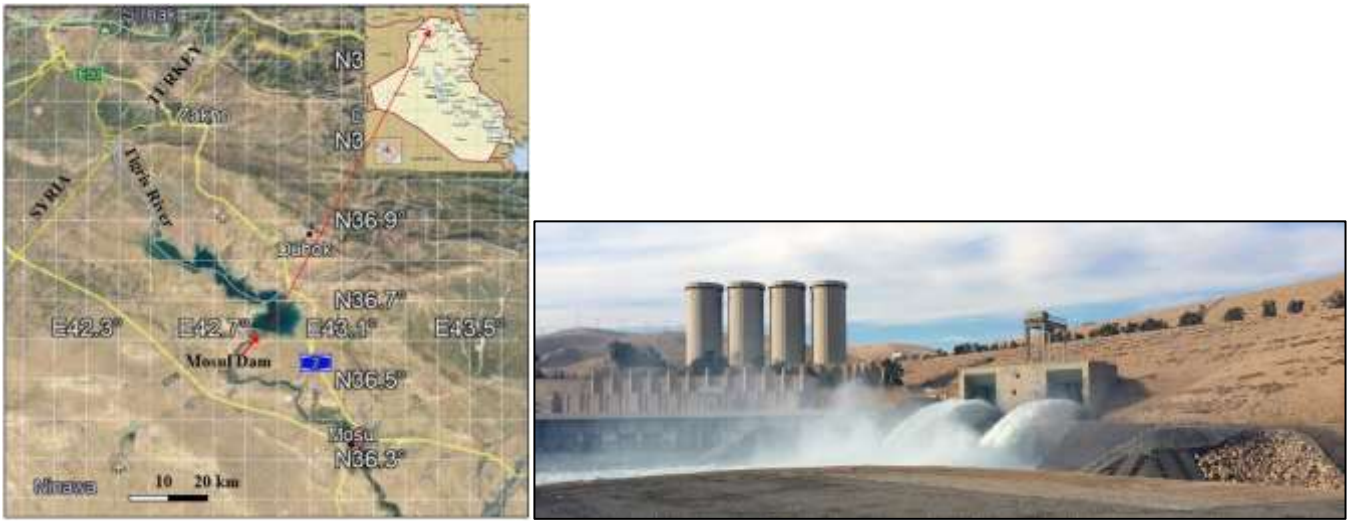

a b

Figure 1. Mosul Dam a) Satellite Image Showing Location Of Mosul Dam, b) General View of the Mosul Dam.

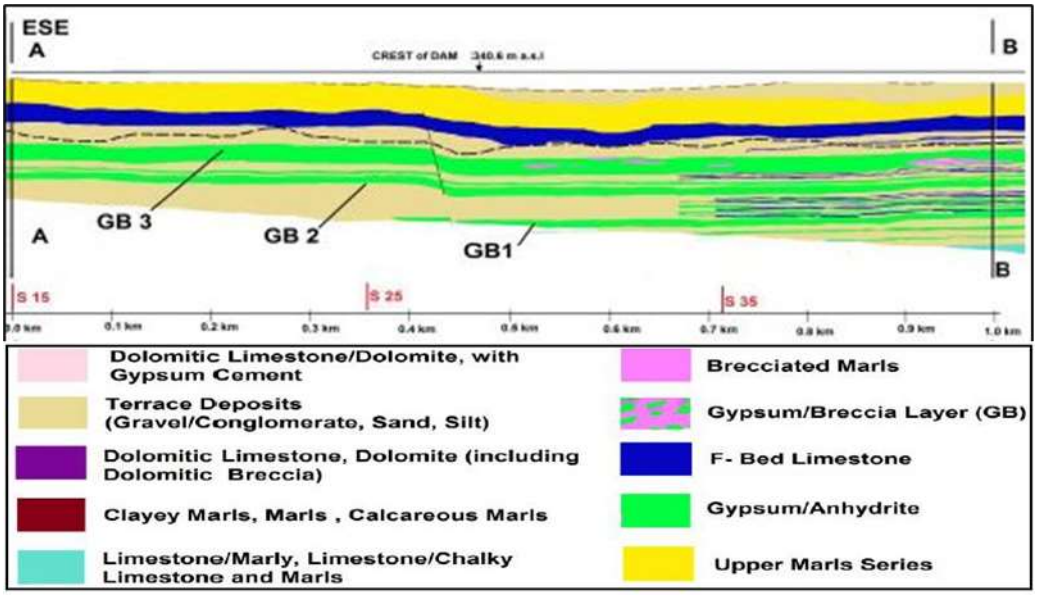

Figure 2. Cross Section on Mosul Dam Axis Showing the Cyclic Sediments of the Fatha Formation. The dashed line represents karstification level, GB = Gypsum bed (Al-Ansari *et al.*, 2015c).

3. The Main Problem of Mosul Dam and Indications

Karstification is the main dangerous problem in the dam site and reservoir area. Due to existence of thick gypsum beds at the dam site, Swiss Consultants (1979) designed the foundations to be grouted since construction until decommissioning of the dam to minimize the karstification. At the end of the 1986, the reservoir level reached 316.4 m (a.s.l.). The reservoir was filled to the normal operation water level of 330 m (a.s.l.) for the first time in 1988. Accordingly, the first sign of trouble appeared at the first filling in the spring of 1986 (Adamo & Al-Ansari, 2016). New sinkholes were observed downstream of the dam (Figure 3); many other seepages were observed too with high sulphate water which indicates dissolution of the gypsum. Moreover, many grouting boreholes along the foundation of the dam were found to be empty which means the grouting materials had disappeared. However, the dam body was inspected in different time intervals and found to be free of cracks, settlement, and dislocation (Mark & Wheeler, 2004; Milillo *et al.*, 2016).

It is worth mentioning that Othman *et al.* (2019) conducted remote sensing study to check the stability of Mosul Dam and they found that "Maximum deformation rate was found to be about 7.4 mm/ year at a longitudinal subsidence area extending over a length of 222 m along the dam axis. Whereas the mean subsidence was about 6.27 mm/ year and lies in the center of the dam.

Figure 3. A Recent Developed Sinkhole (Down-Stream) After Filling of the Reservoir (Al-Ansari *et el.*, 2015b).

After the first impounding of the reservoir in 1986, the dynamic of the groundwater was changed. The new created groundwater dynamic with the operation of the reservoir has accelerated the dissolution of the gypsum beds not only under the foundation but even in the reservoir area; accordingly, the development of the sinkholes was accelerated. Moreover, seepages and springs were observed downstream of the dam, as well as deterioration of the deep grout curtain under the dam. The curtain, during construction was suffering from deficiencies due to inability of closing certain areas in the curtain within the gypsum brecciated layers (Adamo *et al.*, 2015a).

To check and follow up the dissolution of gypsum beds, water samples were chemically analyzed continuously; moreover, seepage rates were monitored and found an increase from 500 l/ sec on February 10, 1986, to 1400 l/ sec on August 16, 1986; with increase in water head from 49 m to 65 m. The chemical analyses of the sampled water showed that the dissolution intensity increased from 42 to 80 t / day.

Issa et al. (2003) conducted bathymetrical survey in the reservoir of Mosul Dam to show the changes in the reservoir bottom morphology with time (1983 – 2001) due to erosion and sedimentation processes. Accordingly, an erosion and sedimentation map was generated (Figure 4). The erosional areas with maximum depth of 9.6 m are believed to represent sinkholes and gypsum dissolved areas (Kelley et al., 2007 ; Wakeley et al., 2007). Some of these sinkholes are about 15 m in diameter and more 15 m in depth (Washington Group International, 2005).

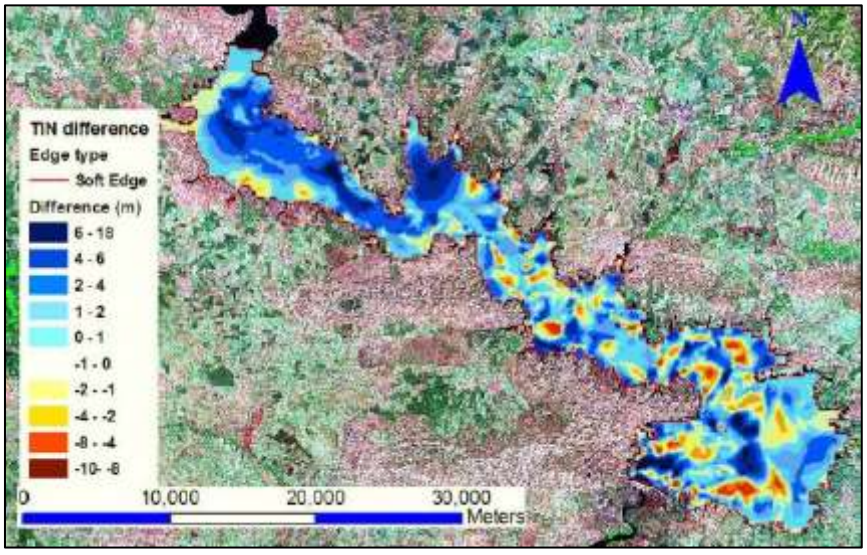

Figure 4. TINs for Survey 2011 and 1983 of Mosul Reservoir (Issa et al., 2003).

4. Protective Actions

Due to the mentioned observed cases and to avoid any possibility of the dam failure, extensive grouting program was performed in 1987 to strengthen the right bank grout curtain extension and to elongate the curtain further to the right side, while re-grouting continued in the river channel section as repair work. It is worth to mention that the grouting is continuous hitherto. The following actions were carried out and part of them is still ongoing.

4.1. Grouting Works

The treatment of the Mosul dam foundations as per design consists of two main elements: a) Blanket grouting, and b) Deep grout curtain. The deep grout curtain construction was completed on February 6th, 1988. But maintenance and repair work which were started in the end of 1986 continues up to now (Adamo *et al.*, 2015b).

4.1.1. Blanket Grouting

This grouting was performed under the core of the main dam. The purpose of this grouting is to close the openings originally existing in the foundation rocks due to dissolution of gypsum beds (karstification). It was planned and designed to seal any seepage paths at the contact of the core with the foundation. To find out later efficiency of the blanket grouting, permeability tests were conducted using Lugeon test in exploratory holes before starting the grouting. Accordingly, high permeability zones were recognized with values 28.7 and 54.5 Lu on the right and left banks, respectively.

4.1.2. Deep Grout Curtain

This grouting was planned and designed to create a barrier to stop the seepage in the foundations under the dam, also to reduce the permeability of the grouted zone. The aim was to stop the dissolution of gypsum beds. Moreover, to seal all types of cavities; accordingly, to reduce the seepage flow in the foundations.

4.1.3. Massive Grouting

This was used in repair works of the grout curtain. Piezometric observation were carried out for checking of the conditions of the grout curtain and the detection of problematic areas where additional treatment was required. Piezometric observation continued and resulted in the repeated application of both normal and massive grouting works up to now, where the grout used from 1986 to 2014 reached 95657.43 tons.

4.2. Lowering Water Level

After 2006, where all grouting processes were almost in vain, an action was suggested to keep the safety of Mosul Dam. This was lowering the maximum normal operation water level in the reservoir to 319 m (a.s.l.) instead of 330 m (a.s.l.) (Adamo and Al-Ansari, 2016). However, this means the dam will operate in all its planned and designed aims to about 60%; including: 1) Water supply for irrigation, 2) Flood control, and 3) Electric power generation. Nevertheless, lowering the water level will decrease: 1) The dissolution rate of gypsum due to lowering the water head, 2) The exerted forces on the dam due to decrease of the water volume.

4.3. Works of the Italian Company

In June 2014, ISIS controlled Mosul Dam for about 2 weeks, during their control; the grouting processes were terminated, and all grouting equipment and materials were destroyed. After the ISIS was dismissed, the dam returned under the control of the Ministry of Water Resources. Accordingly, a new grouting attempt was restarted by an Italian Company named "Trevi". The task was performed and Trevi left the site in March 2018 after training of local engineers. Accordingly, the grouting processes were continued up to the most recent techniques.

5. Discussion

The safety of Mosul Dam is still a matter of debate. Keeping the dam from collapsing is a never-ending task (IWPDC, 2011). Although, the Italian company completed the task of the grouting in March 2018; however, the normal operation water level is still not 330 m (a.s.l.). In 2019, the Ministry of water Resources ventured to reach level 323 m (a.s.l.) but the level was lowered back quickly to level 319 m (a. s. l). This is a good indication that the dam's safety is still doubtful.

Grouting of the karstified rocks in dams can give reverse results when is not correctly performed (Bonaci et al., 2009) or when performed by using missinterpreted data (Sissakian *et al.*, 2017). Hereinafter are some missinterpreted data which led to an endless successful grouting.

5.1. Missinterpreted karstification line

Figure 2 shows the karstification line which was used to indicate the depths of the grouting boreholes, and it shows that there are many gypsum layers below the line. Those gypsum beds will dissolve, and voids and caverns will be developed, and the grouting materials will go down in the developed caverns below the karstification lines.

5.2. Miss Interpreted Terra Rossa

In some of the boreholes, bauxite is described. Actually, it is not bauxite; it is reddish brown clay called Terra Rossa; a good indication for karst (Merino *et al.*, 2006). But it was not considered as karst indication by the site geologists of the construction companies (GIMOD), and consequently no grouting was performed.

5.3. Dam Safety

From reviewing the missinterpreted data which was used in planning the depths of grouting boreholes and/or areas which need to be grouted, the grouting process will not be effective and will not be able to seal the caverns developed due to the karstification of gypsum and/or limestone beds because the karstification is an ongoing process. Accordingly, the seepages will continue from the foundations. Moreover, keeping the water level in the reservoir lower than the designed elevation (330 m, a.s.l.) means that the dam is still not completely safe.

Recently, the grouting operation is carried out using new technique. The area is connected with a grouting network that is computerized. It should be mentioned however, that the water level is kept at 319 m (a. s. l..). At this level the dam is stable.

6. Conclusions

From the reviewed and reinterpreted data, it is clear that the safety of Mosul Dam is still a matter of debate, and the dam requires continuous technical monitoring. It is very difficult and suspicious to conclude that Mosul Dam is in a safe status or otherwise. For this reason, the water level is kept at or lower than 319 m (a. s. l.).

References

Adamo, N. & Al-Ansari, N. (2016). Mosul Dam the full Story*:* Engineering Problems. *Journal of Earth Sciences and Geotechnical Engineering*, *6*(3), 213–244. Retrieved from www.researchgate.net/publication/306586473_Mosul.

Adamo, N., Al-Ansari, N., Sissakian, V., Issa, E.I. & Knutsson, S. (2015). Mystery of Mosul Dam the most Dangerous Dam in the World: Problems Encountered During and After Impounding the Reservoir. *Journal of Earth Sciences and Geotechnical Engineering*, *5*(3), 47–58. Retrieved from *www.researchgate.net/publication/275949182*.

Al-Ansari, N., Issa, E.I., Sissakian, V.K., Adamo, N. & Knutsson, S. (2015a). Mystery of Mosul Dam the most Dangerous Dam in the World: The project. *Journal of Earth Sciences and Geotechnical Engineering*, *5*(3), 15–31. Retrieved from www.academia.edu/12458385/ Mystery_of_Mosul_Dam.

Al-Ansari, N.A., Adamo, N., Issa, I.E., Sissakian, V. & Knutsson, S. (2015b). Mystery of Mosul Dam the Most Dangerous Dam in the World: Karstification and Sinkholes. *Journal of Earth Sciences and Geotechnical Engineering*, 5, 33–45. Retrieved from www.scienpress.com/Upload/GEO/Vol 5_3_3.pdf.

Bonacci, O., Gottstein, S. & Roja- Bonacci, T. (2009). Negative impacts of grouting on the underground karst environment. *Echohydrology*, *2*(4), 492–502. Retrieved from www.nat-hazards-earth-syst-sci.net/13/2041/2013/nhess-13-2041-2013.pdf.

Iraqi Ministry of Water Resources (2012). Water Resources, Mosul Dam. Retrieved from https:// *www.mowr*. gov.iq/en.

Issa, E.I., Al-Ansari, N.A. & Knutsson, S. (2013). Changes in Bed Morphology of Mosul Dam Reservoir. *Journal of Advanced Science and Engineering Research*, *3*(2), 86–95. Retrieved from www.researchgate.net/publication/246545981.

IWPDC (International Water Power and Dam Construction) (2011). An unprecedented task 3 November 2011. Retrieved from https://www.waterpowermagazine.com/features/featurean-unprecedented-task.

Kelley, J. R., et al. (2007). Geologic Setting of Mosul Dam and its Engineering Implications. USACE, Engineering Research and Development Center. Retrieved from https://apps.dtic.mil/dtic/tr/fulltext/u2/a472047.

Mark & Wheeler (2004). Mosul Dam Assessment. Task Order No. 8, Report on Site Visit. Mosul Dam Library, 3–7 September, 2004.

Merino, E., Banerjee, A. & Dworkin, S. (2006). Dust, terra rossa, replacement, and karst: serendipitous geodynamics in the critical zone. *Geochimica et Cosmochimica Acta*, *70*(18), A416. Retrieved from *www.deepdyve.com/lp/elsevier/dust-terra-rossa*.

Milillo, P. et al. (2016). Space Geodetic Monitoring of Engineered Structures: The Ongoing Destabilization of the Mosul Dam, Iraq. Scientific Reports, 6, Article No. 37408. doi: https://doi.org/10.1038/srep37408. Retrieved from *http://www.nature.com/articles/srep37408*.

Sissakian, V.K. & Fouad, S.F. (2015). Geological Map of Iraq, scale 1:1000000 (4th ed.). *Iraqi Bulletin of Geology and Mining*, *11*(1), 9–16.

Sissakian, V., Adamao, N., Al-Ansari, N., Knutsson, S. & Laue, J. (2017). Defects in Foundation Design Due to Miss-Interpretation of the Geological Data. A Case Study of Mosul Dam. *Scientific Research, Engineering*, *9*(7), 1–15. Retrieved from http://file.scirp.org/Html/5-8102857_78053.htm.

Swiss consultants (1979). Mosul Dam Project-planning report. State Organization of Dams, Republic of Iraq, Ministry of Irrigation, Vol. 1. Report Library of Mosul Dam.

Wakeley, L.D., Kelley, J.R., Talbot, C.A., Pearson, M.L. & Broadfoot, S.W. (2007). Geologic Conceptual Model of Mosul Dam. U.S. Army Engineer Research and Development Center. 61pp. Retrieved from *https://www.researchgate.net/publication/235070116_Geologic_Conceptual_Model_of_Mosul_Dam*.

Washington Group International, Black & Veatch, J. V. (2005). Mosul Dam Study. Final Report, Task Order No. 8. Republic of Iraq Project Contracting Office, Provisional Coalition Authority.

Research Article

Industrial Assessment of Limestone Beds of the Qamchuqa Formation for Cement Industry, Kurdistan Region, North Iraq

Varoujan K. Sissakian [1, a,*], Ala A. Ghafur [1, b], Sarhang A. Omer [2, c], Diyar S. Khlail [3, d]

[1] Department of Natural Resources Engineering and Management, School of Science and Engineering, University of Kurdistan Hewlêr, Erbil, KRI, Iraq
[2] Mineral Resource Engineer, Erbil, KRI, Iraq
[3] Mineral Resource Engineer, Sulaimani, KRI, Iraq

E-mail: [a] f.khajeek@ukh.edu.krd, [b] ala.abdulla@ukh.edu.krd, [c] sarhang.ahmed88@gmail.com, [d] d.m.khalil1@gmail.com

Access this article online		
Received on: September 16, 2021	**Accepted on:** November 23, 2021	**Published on:** December 28, 2021
DOI: 10.25079/ukhjse.v5n2y2021.pp62-71	**E-ISSN:** 2520-7792	

Abstract
The Qamchuqa Formation is widely exposed in Iraqi Kurdistan Region (IKR); north of Iraq. The formation along with the Bekhme Formation form the bulk of the main mountains (anticlines) in the IKR. Among those anticlines is the Ranya anticline, which has a NW–SE trend, where the Qamchuqa Formations has a thickness of about 700 m. The main lithological facies of the formation are: limestone, dolomitic limestone and dolomite. We have sampled the upper most 89 meters of the northeastern limb, by collecting 10 samples of different sampling intervals that range from (3–12) m. The ten rock samples were tested by an XRF to measure the concentration of the oxides in each sample. The XRF results showed that the 10 rock samples are limestone with different percentages of oxides. The weighted averages of the oxides in the collected samples have been calculated, and the results showed that the limestone beds along the studied section in the upper part of the Qamchuqa Formation are suitable for cement industry. The average concentration of CaO and MgO is 55.13% and 0.26%, respectively.
Keywords: Qamchuqa Formation, Limestone, Cement industry, Reserve Estimation, IKR.

1. Introduction

Generally, the exposed rocks in IKR are not well evaluated for industrial uses; this is attributed to the fact that the rocks are not well studied and investigated, as carefully as all other metallic and non-metallic minerals" (Sissakian, 2018). However, there are very few studies which were carried out, dealing with different metallic and nonmetallic minerals and industrial rocks. Five cement plants are concentrated in the Bazian vicinity; southwest of Sulaimaniyah city (Figure 1).

There are six cement plants in the IKR; 5 of them are located in the Sulaimaniyah Province and only 1 in the Erbil Province (Figure 1). Those cement plants which are located in the Sulaimaniyah Governorate use the limestone from the Sinjar Formation (Eocene age), whereas the one in Erbil Governorate uses limestone from the Anah and Euphrates formations (Upper Oligocene and Lower Miocene, respectively). It is known that the limestone of the Sinjar Formation is better than those of the Anah and Euphrates formations; as far as the cement industry is concerned. This is attributed to the low thickness of the Anah and Euphrates formations and high MgO content as compared to the rocks of the Sinjar Formation (Al-Bassam, 2012).

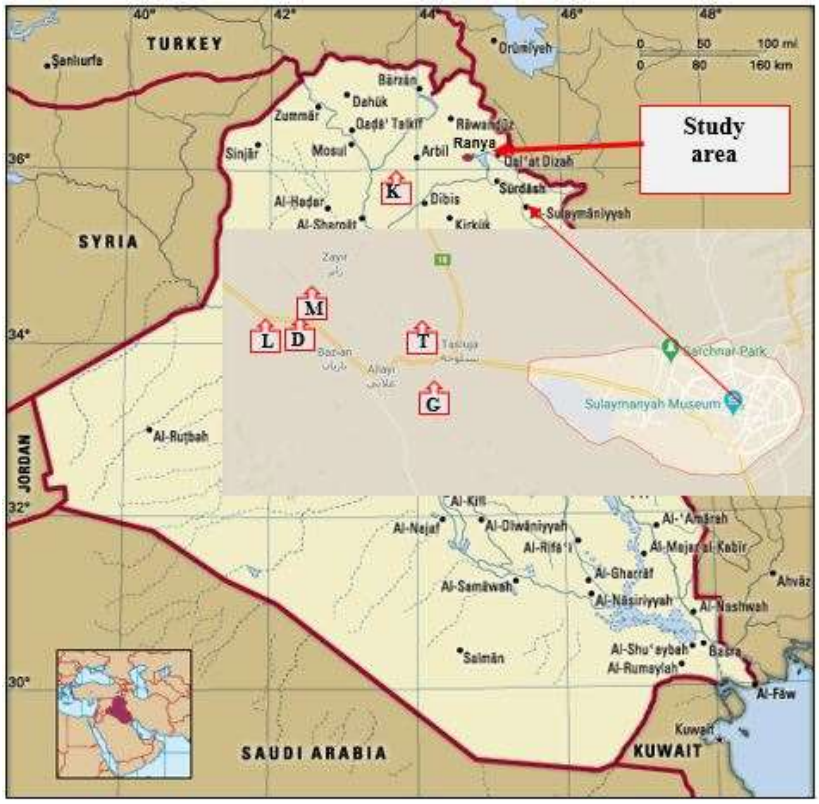

Figure 1. Location Map of the Six Existing Cement Plants In IKR. Plants' Names: K= KAR, T= Tasluja, M= Mass, L= Lafarge, D= Delta, and G= Gasin. The location of the study area also is shown, NE of Ranya town.

1.1. Previous Work

The Iraq Geological Survey (GEOSURV) has conducted different researches to indicate the suitability of the limestone beds within different formations in the whole Iraqi territory including the IKR. Majority of the constructed cement plants in IKR have used the data of the carried out work by GEOSURV. The achieved results from the scientific reports were presented by the owners of those companies to the Ministry of Natural Resources (Erbil) to get licenses, which were used either to construct a new cement plant or to keep the license for future use.

Sissakian *et al.* (2019) studied the limestone beds of the Pila Spi Formation in Permam anticline, near Al-Maseef and mentioned about very good quality and quantity of rocks, suitable for cement industry. Sissakian *et al.* (2020) studied the exposed rocks of the Pila Spi Formation (Upper Eocene) at Haibat Sultan Mountain, 17 km east of Koya town and concluded on the existence of excellent deposit for the cement production. Ghafur *et al.* (2021) studied the limestone beds of the Bekhme Formation (Upper Cretaceous) at Galley Ali Beg gorge and reported on some excellent deposits, which can be used for the cement production.

1.2. Location

The studied section is located northeast of Ranya town (Figures 1 and 2), in a long mountain range, which forms the northeastern limb of the Ranya anticline. The mountain is called Kiwa Rash, and is located east of Dukan Lake. The section is accessible by many roads from Sulaimaniyah city or Erbil city, via Ranya. We have found the location to be suitable for the construction of a cement plant. The location is against the main wind direction toward the Ranya town and about 10 km far from the city. The only inhabitants which are in the affected area is a small village called Sarsian (Figure 2) which will be affected by wind and the fallen cement dust. This village can be relocated because it is located within a large alluvial fan that is covered by clayey soil which is very suitable for the cement production to be mixed with the limestone as the main raw mix (Sissakian et al., 2021).

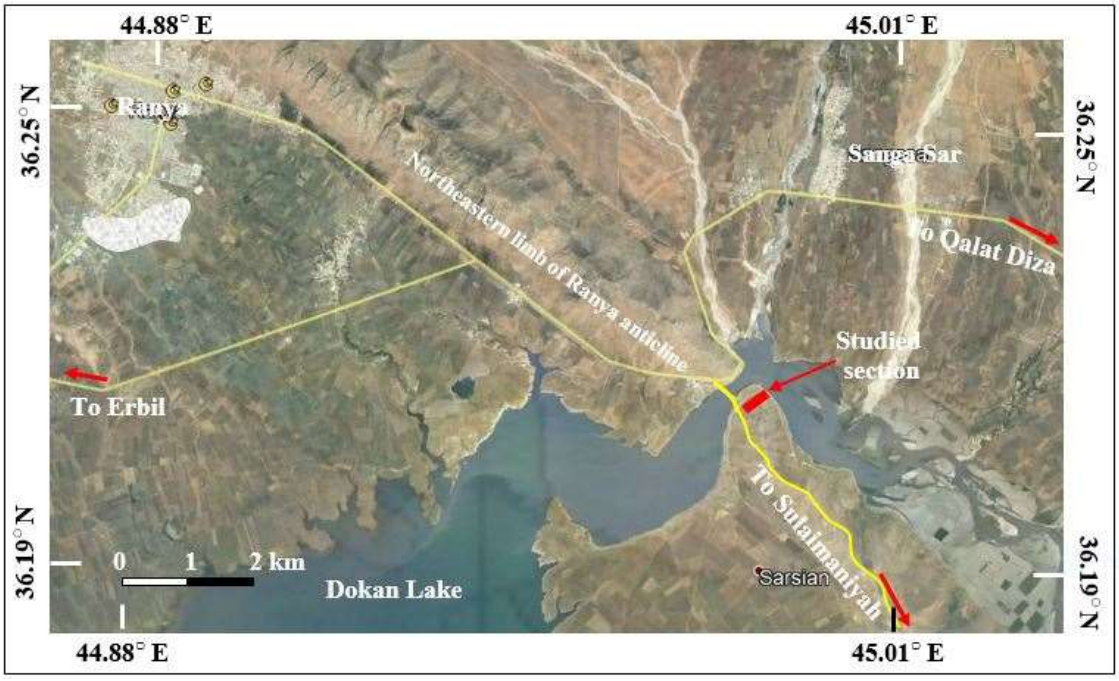

Figure 2. Satellite Image Showing the Studied Section and the Surrounding Area.

1.3. Aim

The aim of this study is to indicate the suitability of the rocks of the Qamchuqa Formation in the Ranya vicinity, in Ranya anticline for cement industry. The preliminary evaluation depends on the acquired results, from subjecting the collected rock samples to a XRF test. The indicated concentrations of the main oxides were used to perform an industrial assessment for the exsiting beds in the upper part of the Qamchuqa Formation, through the collected 10 samples which represent the upper 89 m of the formation. This was achieved by comparing the results, with the standard specification for cement industry.

2. Data Used and Methodology

In order to conduct this research work, different materials have been used; like a geological map at a scale of 1:100000 and satellite imagery, which were used to indicate the exposures of the Qamchuqa Formation in the vicinity of the Ranya town. Moreover, the maps were used to select a relevant area; not only for sampling but also to make sure that the selected area is far from inhabited centers such as the Ranya town, and that there is relevant space for any industrial sites; such as a cement plant.

We collected 10 samples from the upper exposed 89 m of the Qamchuqa Formation in different sampling intervals; where ever there was a major lithological change. The samples were tested in the field by a hand lens for description and then checked by diluted (5%) Hydrochloric acid (HCl) (Table 1). The samples were numbered and kept in proper sample bags; then they were sent to the chemical laboratory of the University of Kurdistan Hewler and were tested by XRF. The results were used for industrial assessment as the cement industry is concerned. The sampling interval was measured by a measuring tape, whereas the hardness was measured by the hammer blows (Hack & Huisman, 2002).

The collected 10 samples were crushed, ground, powdered, and then divided into 4 parts using a mechanical splitter. From one of the four divided parts of each sample, 200 gm was dried using an electrical oven for 24 hours. The dried sample was prepared as a pellet then mounted in the XRF equipment (Figure 3) to be analyzed. The acquired data from the XRF test are presented in Table (2). Six oxides (CaO, MgO, SiO_2, Fe_2O_3, Al_2O_3, Na_2O) and L.O.I. were analyzed for the collected samples, and the results are shown in Table (2).

Table 1. Field Description of the Samples.

Sample No.	Rock type	Color	Hardness	Thickness (m)	Reaction with HCl	Notes
1	Limestone	Grey	Hard	3	Slight	Bedded
2	Limestone	Light Grey	Hard	3	High	Bedded
3	Limestone	Grey	Hard	9	Slight	Well Bedded
4	Limestone	Light Grey	Very Hard	10	High	Thickly bedded to massive
5	Limestone	Greyish brown	Hard	10	Very High	Thickly bedded to massive
6	Limestone	Grey	Very Hard	10	Slight	Thickly bedded to massive
7	Limestone	Light Grey	Hard	12	High	Thickly bedded to massive
8	Limestone	Greyish brown	Hard	10	Very High	Thickly bedded to massive
9	Limestone	Grey	Very Hard	12	Slight	Thickly bedded to massive
10	Limestone	Light Grey	Hard	10	High	Thickly bedded to massive

Figure 3. The Used XRF Equipment.

Table 2. The Concentrations of Main Oxides Within the 10 Rock Samples.

Sample No.	CaO %	MgO %	SiO_2 %	Fe_2O_3 %	Al_2O_3 %	Na_2O %	L.O.I. %
1	54.52	1.33	0.37	0.31	0.18	0.07	43.97
2	54.77	1.19	0.28	0.31	0.17	0.06	43.56
3	54.43	1.37	0.31	0.31	0.22	0.07	43.85
4	54.57	1.39	0.19	0.30	0.16	0.10	43.82
5	53.79	1.35	0.94	0.35	0.21	0.06	43.60
6	53.99	1.31	0.76	0.32	0.31	0.09	53.71
7	54.52	1.32	0.29	0.30	0.19	0.10	43.70
8	54.82	1.22	0.13	0.30	0.13	0.10	43.92
9	54.80	1.22	0.16	0.30	0.14	0.09	43.30
10	54.94	1.15	0.13	0.30	0.13	0.14	53.65

The results from the XRF test (Table 2) were compared with the standards for cement industry, as shown in Table (3).

Table 3. Iraqi Standards No.5 for Cement Production, 1984 (ISQC, 2016).

Iraqi Standard	
CaO	> 45 %
MgO	< 2 %
SO_3	< 1 %
Cl	0.5 – 1.0 %
$K_2O + Na_2O$	0.05 %
Fe_2O_3	< 0.1% *

* For white cement only

3. Geology of the Studied Site

The concerned site lies along the northeastern limb of the Ranya anticline, north east of Ranya town. The main geological aspects (Geomorphology, Tectonics and Structural Geology, and Stratigraphy) are briefed hereinafter, depending on Sissakian *et al.* (2014), Fouad (2015), and Sissakian & Al-Jeburi (2014), respectively.

3.1. Geomorphology

The studied site lies physiographically within the High Mountainous Province. The following geomorphological units are developed:

Structural Geological Units: The anticlinal ridges extend longitudinally surounding the anticline. They exist within the Qamchuqa Formation and are potential areas to locate quarries.

Structural – Denudational Units: The flatirons are the main units, they exist within the Qamchuqa Formation; along with the fault and erosional scarps.

Alluvial Units: The alluvial fans are the main geomorphological unit which cover vast areas (Figure 4), and they can be used as a good source for clay deposit, besides being suitable areas for locations of industrial sites. The colluvial deposits exist along the foothills of the Ranya anticline. Flood plain sediments and river terraces are also developed in the studied site.

3.2. Tectonics and Structural Geology

The studied site lies within the High Folded Zone, Outer Platform of the Arabian Plate, which is a part of the Zagros Thrust – Fold Belt. The belt suffers from the stresses exerted by the collision of the Arabian and Iranian plates. Only Ranya anticline exists in the studied site, it has the following charactersitics.

Ranya Anticline: It forms en-echelon plunge with the Korak anticline. The length of the anticline is 45 km trending NW – SE and the southwestern limb is steeper. The axis of the anticline is dissected by faults, which have almost the trend of the axis causing ambiguity of the trend of the axis. Thick alluvial fan sediments cover the south eastern plunge. The oldest exposed formations in the Ranya anticline are of a Lower Jurassic age (Figure 4).

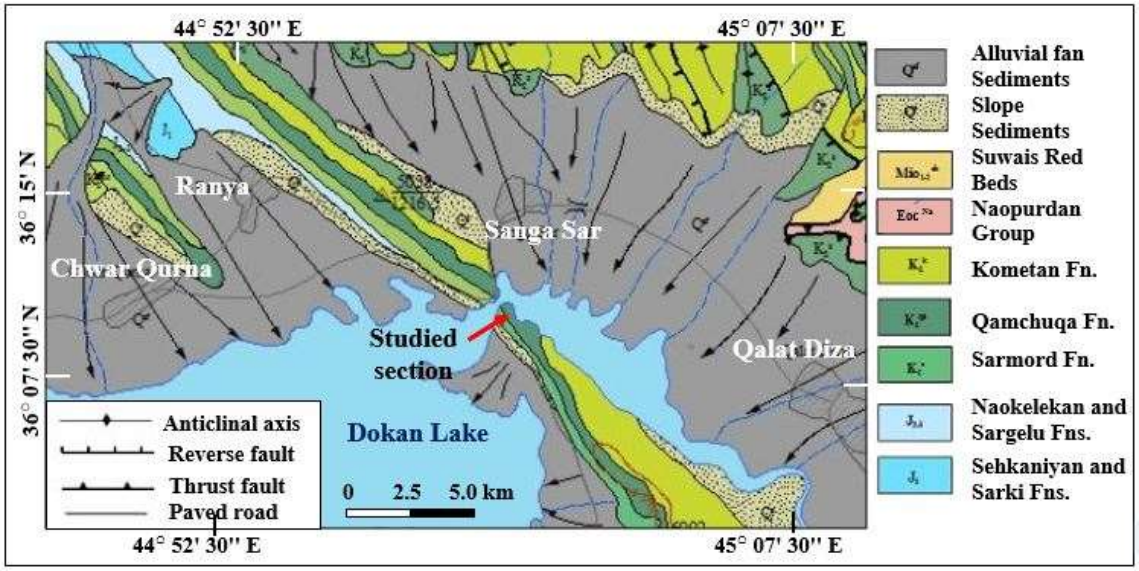

Figure 4. Geological Map of the Studied Site (Sissakian & Fouad, 2015).

3.3. Stratigraphy

The studied section lies within the Qamchuqa Formation. Although many formations are exposed surrounding the studied section (Figure 4), we have described the exposed Qamchuqa Formation only, because it is the target of the current research work.

Qamchuqa Formation (Lower Cretaceous): The formation comprises of massive (Figure 5) limestone, dolomitic limestone and dolomite, usually light and dark grey, and brownish grey, and hard to very hard (Table 1). The thickness of the formation in Ranya it is around 500 m, however, we have only sampled the uppermost 89 m only.

4. Results

The 10 rock samples were uploaded into an XRF equipment to indicate the concentrations of the main oxides (Table 4). The main oxides weighted averages were calculated from the XRF test results for each sample (Table 4). The weighted averages which are used in the industrial assessments were calculated because the sampling interval is not uniform (Tables 1 and 4).

The weighted percentage of each oxide in each sample is calculated by the following equation (IET, 2021)

$$Weighted\ Percentage = \frac{\sum C1+C2+C3+C4+Ci}{\sum T1+T2+T3+T4+Ti} \quad (1)$$

Where C = the percentage of each oxide multiplied by the sample's thickness (T),

The weighted average is calculated as follows:

$$Weighted\ Average = \frac{\sum W1+W2+W3+W4+Wi}{\sum T1+T2+T3+T4+Ti} \quad (2)$$

Where W = the weighted percentage of each oxide multiplied by the sample's thickness (T).

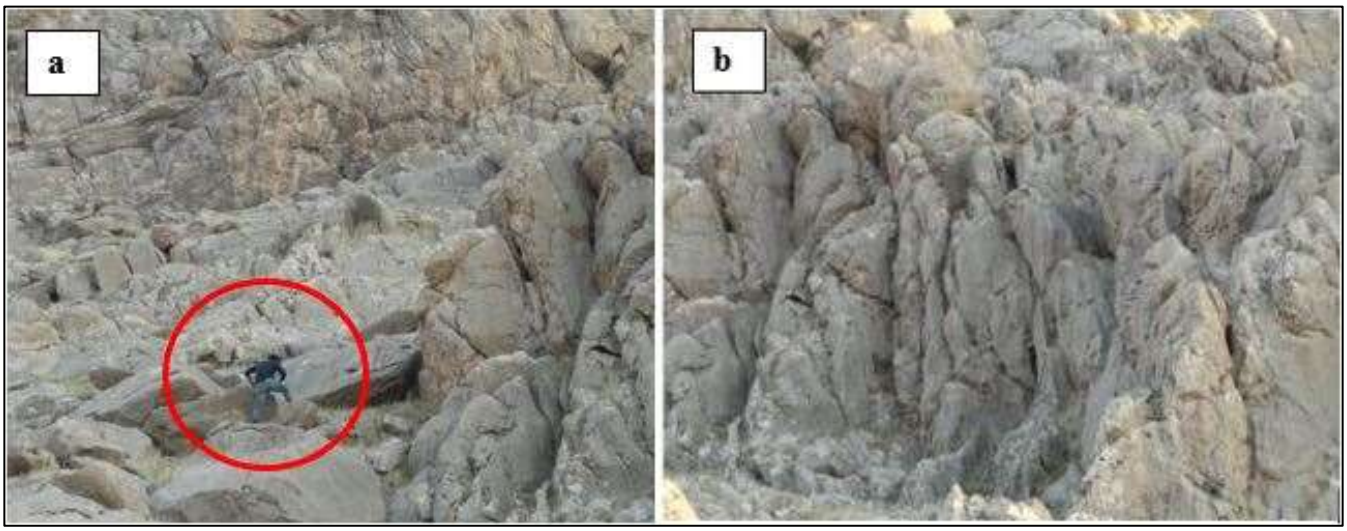

Figure 5. Well Bedded and Massive Beds of the Qamchuqa Formation, a) Sampling Of The Beds; the third author is encircled in red, b) Close up View of the Sampled Beds.

Table 4. The Concentration of Oxides with Weighted Percentages and Averages of the 10 Samples.

Sample No.	Thick. (m)	CaO		MgO		SiO_2		Fe_2O_3		Al_2O_3		Na_2O		L. O. I.	
		%	Wa%	%	Wa%	%	Wa%	%	Wa%	%	Wa%	%	Wa%	%	Wa%
1	3	54.52	163.56	1.33	3.99	0.37	1.11	0.31	0.93	0.18	0.54	0.07	0.21	43.97	131.91
2	3	54.77	164.31	1.19	3.57	0.28	0.84	0.31	0.93	0.17	0.51	0.06	0.18	43.56	130.68
3	9	54.43	489.87	1.37	12.33	0.31	2.79	0.31	2.79	0.22	1.98	0.07	0.63	43.85	304.65
4	10	54.57	545.70	1.39	13.90	0.19	1.90	0.30	3.00	0.16	1.60	0.10	1.00	43.82	438.20
5	10	53.79	537.90	1.35	13.50	0.94	9.40	0.35	3.50	0.21	2.10	0.06	0.60	43.60	436.00
6	10	53.99	539.90	1.31	13.10	0.76	7.60	0.32	3.20	0.31	3.10	0.09	0.90	53.71	537.10
7	12	54.52	654.24	1.32	15.84	0.29	3.48	0.30	3.60	0.19	2.28	0.10	1.20	43.70	524.40
8	10	54.82	548.20	1.22	12.10	0.13	1.30	0.30	3.00	0.13	1.30	0.10	1.00	43.92	439.20
9	12	54.86	657.60	1.22	14.64	0.16	1.92	0.30	3.60	0.14	1.68	0.09	1.08	43.30	519.60
10	10	54.94	549.40	1.15	11.50	0.13	1.30	0.30	3.00	0.13	1.30	0.14	1.40	53.65	536.50
Total			4850.68		114.47		31.64		27.55		16.39		8.20		4088.20
Average			54.50		1.29		0.35		0.31		0.18		0.09		45.93

K_2O, MnO, SO_3, and Cl were also analyzed but all of them were below the detection limits of the XRF equipment.

5. Discussion

5.1. Industrial Assessments

The concentrations of the main oxides of the collected 10 samples, and their weighted averages (Table 4) indicate that the 10 samples are pure limestone since the maximum and minimum CaO and MgO concentrations are 54.94% (Sample No. 10), 53.79 (Sample No. 5), 1.39 % (Sample No. 4), and 1.15 % (Sample No. 10), respectively (Table 4). Therefore, we have discussed the industrial assessments of the collected samples by comparing the results with the Iraqi Standards for cement industry (Table 3).

- **Cement Industry:** The main two oxides which control the cement production are CaO and MgO, and both are within the required standards (Table 3, 4 and 5). However, concentrations of SO_3 and Cl^- were not recorded; meaning undictable concentrations. Accordingly, the concentrations will be within the limits of the used standards (Tables 3, 4 and 5). As for white cement the Fe_2O_3 needs to be less than the recorded percentage.

Table 5. Comparison of the Standard of Cement Industry and the Current Study's Results.

Cement Standards		Current Study		Legend	
CaO	> 45.00	54.94		Standards	
MgO	< 2.00	1.29			
Fe_2O_3	< 0.10*	0.31			Within the range
SO_3	< 1.00				
Cl	0.50 – 1.00				Not detected
L.O.I.	> 43.00	46.22			

5.2. Quarrying Conditions

Before selecting a relevant area for sampling, the quarrying conditions were considered, besides considering available relevant area to be the site for a plant. The following aspects were considered:

- No overburden or very thin (Figure 6a),
- No innerburden (Figure 5a),
- Clear bedding and intense jointing (Figure 5a and 6a) which will facilitate quarrying,
- Available water and electricity sources for plant construction (Figure 6b),
- Available area for plant construction (Figure 6b),
- Relevant thickness of the exposed limestone (Figure 7a),
- Possibility of quarrying by bulldozers and excavators (Figure 7b), and
- Availability of main roads nearby the quarry area (Figure 2).

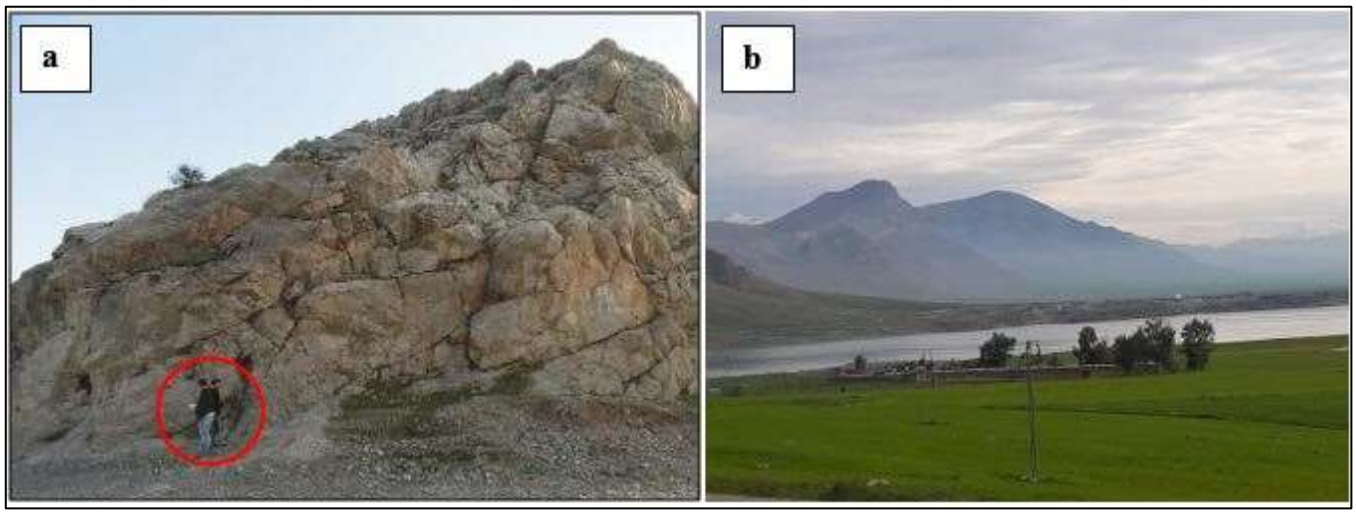

Figure 6. a) The Uppermost Part of the Sampled Section, Note the Absence of Overburden, B) Dokan Lake and Alluvial Fans (Occupied as Agricultural Fields).

5.3. Geological Reserve Estimation for a Cement Plant

The acquired results from analyzing of the 10 collected limestone samples showed very interesting and encouraging results for different industries; however, the results are more suitable for the construction of a cement plant (Tables 3, 4 and 5), besides the available mentioned quarrying conditions. Consequently, a geological reserve estimation can be considered by using the acquired chemical data for the weighted averages of Cao and MgO concentrations, which are 54.50% and 1.29%, respectively.

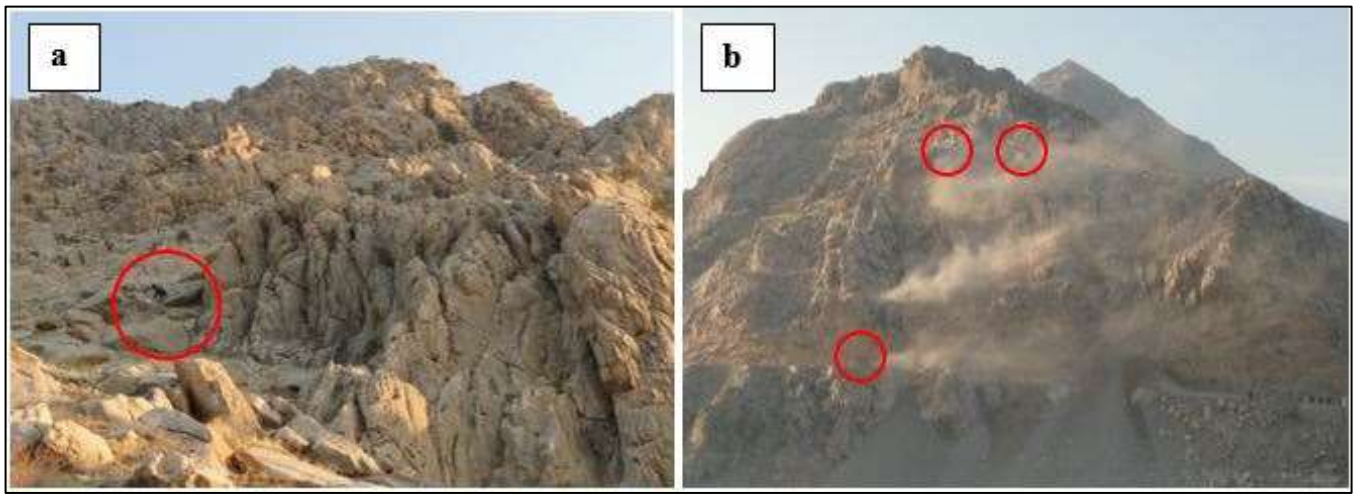

Figure 7. a) The Upper Part of the Sampled Section, Compare the Thickness of the Sampled Section with the Author's Height; circled by red, b) Mechanical Ripping of the Rocks by Bulldozers and Excavators; circled by red (During the Widining of the Road in the Opposite Side of the Sampled Section).

This is an assumption about a quarry area of 0.5 km^2, then the geological reserve can be calculated as follows:
The surface area = 250,000 m^2
The thickness of the sampled part = 89 m, and we will consider it 90 m,
The volume of the limestone within the supposed quarry = 250,000 X 90 = 22,500, 000 m^3
The average density of the limestone is about 2,400 kg/ m3,
The weight of the limestone which can be quarried = 2400 X 22,500,000 = 54 X 10 ^{9} kg,
= 54,000,000 tons.

The second raw material for the raw mix in cement production is clay, which is available in the sampled area where huge alluvial fans cover the whole flat area (Figures 2, 4 and 6b). The added clay to the raw mix is about 30 – 40 % of the used limestone.
Therefore, 35% of 54,000,000 = 18,900,000 tons
Total used raw mix = 54,000,000 + 18,900,000 = 72,900,000 tons
If the daily production of a cement plant is 3,500 tons, then the used quantitiy of the raw mix is about 7,000 tons/day, accordingly means:
72,900,000 ÷ 7,000 = about 10410 days, which is about 29 years.

The acquired result of the tested samples showed that the limestone beds are homogeneous along the sampled section (Table 4). This means the limestone beds surrounding the sampled section have almost the same chemical composition. Therefore, the area of the suggested quarry can be extended; consequently, the calculated geologic reserves will be more than the estimated. However, we have to emphasize that this is a prelimenary reserve estimation with a Low Level of Confidence according to JORC (1999). Therefore, it cannot be used for investments, unless, relevant site investigation is carried out to estimate the reserve with High Level of Confidence according to JORC (1999) which accordingly can be used for investment. The detailed site investigation should include boreholes' drilling of continuous core with spacing not more than 150 m and core sampling of one-meter interval, and the analyzing of all collected samples.

6. Conclusions

From the acquired results of the this study, the following can be concluded: the exposed beds within the Qamchuqa Formation in the studied section are pure limestone. The exposed limestone can be used for cement production using available clay within the alluvial fan sediments. However, the acquired results cannot be used for investment of the rocks in the studied section, since the curried out work is a preliminary evaluation for the studied rocks.

Acknowledgment

The used data in the current study are from the graduation project of Mr. Sarhang O. Omer from the University of Kurdistan Hewler (UKH) as a Natural Resource Engineer. Without the presented data, we couldn't be able to perform this research; therefore, we highly appreciate his work. Thanks are extended to Mr. Hassan O. Omer and Mrs. Dalya Akram both from UKH for their help in using the XRF equipment. The authors also would like to thank Mr. Paul Dirk Embey, English Language Lecturer in UKH for proofreading the manuscript.

References

Al-Bassam, K.S. (2012). Mineral Deposits and Occurrences. In: the Geology of the Low Folded Zone. *Iraqi Bulletin of Geology and Mining*, Special Issue,159-188.

Fouad, S.F. (2015). Tectonic Map of Iraq, scale 1: 1000000 (3rd ed.). *Iraqi Bulletin of Geology and Mining, 11*(1), 1–8.

Ghafur, A.A., Sissakian, V.K. & Bapir, A.M. (2021). Industrial Assessment of the Rocks of the Bekhme Formation in Korek Mountain, Iraqi Kurdistan Region. *Carbonates and Evaporates, 36*(3), 1-10.

Hack, H.R. & Huisman, M. (September 2002). *Estimating the intact rock strength of a rock mass by simple means*. Proceedings of 9th Congress of the International Association for Engineering Geology and theEnvironment. Durban, South Africa.

IET (2021). How To Calculate Weighted Average in 3 Steps (with Example). Retrieved on 12 August 2021 from https://www.indeed.com/career-advice/career-development/how-to-calculate-weighted-average.

Iraqi Standardization and Quality Control System (2016). Iraqi Standards for cement Production, 1984. Retrieved in Arabic from http://www.uokufa.edu.iq/qclab/wp-content/uploads/2016/03. Last retrieved on 31 August.

JORC (1999). Australian Code for Reporting of Mineral Resources. Retrieved from http://www.jorc.org/docs/historical_documents/1999_jorc_code.pdf.

Sissakian, V.K. (2018). The Minerals Wealth in Kurdistan Region: A Critical Review. *UKHJSE, 2*(3), 23–36.

Sissakian, V.K. & Fouad, S.F. (2015). Geological Map of Iraq, scale 1: 1000000, 4th edition. *Iraqi Bulletin of Geology and Mining, 11*(1), 9–18.

Sissakian, V.K. & Al-Jiburi, B.M. (2014). Stratigraphy of the High Folded Zone. *Iraqi Bulletin of Geology and Mining,* Special Issue, 73–16.

Sissakian, V.K., Kadhim, T.H. & Abdul Jabbar, M.F. (2014). Geomorphology of the High Folded Zone. In: Geology of the High Folded Zone. *Iraqi Bulletin of Geology and Mining*, Special Issue, 7–56.

Sissakian, V.K., Hamoudi, D.A., Omer, H.O. & Niazi, S.A. (2019). Assessment of the Carbonate Rocks of the Pila Spi Formation for Cement Industry, in Permam Mountain, Erbil, Iraqi Kurdistan Region. *UKHJSE*, *3*(4), 1–9.

Sissakian, V.K., Ahmed, J.M. & Ibrahem, R.K. (2020). Industrial Assessment of the Carbonate Rocks of the Pila Spi Formation at Haibat Sultan Mountain, Iraqi Kurdistan Region. *ARO*, *8*(1), 24–30.

Sissakian, V.K., Ghafur, A.A., Ibrahem, F.I., Abdulahaq, H.A., Hamoodi, D.A. & Omer, H.O. (2021). Suitability of the Carbonate Rocks of the Bekhme Formation for Cement Industry, Hareer Mountain, North Iraq, Kurdistan Region. *Iraqi Geological Journal*, *54*(2C), 59–67.

Review Article

A Summary on the Use of Fly Ash as a Partial Replacement Material for Cement in Concrete

Heba Adnan Ahmed *

Department of Surveying, Darbandikhan Technical Insititute, Sulaimani Polytechnic University, Sulaymaniyah, KRI, Iraq

E-mail: [a] hiba.adnan@spu.edu.iq

Access this article online		
Received on: September 21, 2021	**Accepted on:** December 9, 2021	**Published on:** December 28, 2021
DOI: 10.25079/ukhjse.v5n2y2021.pp72-80	**E-ISSN:** 2520-7792	

Abstract

Cement is one of the most widely used building materials on the planet. Cement manufacturing has also increased carbon emissions to their greatest level in recent years. Alternative or low-emissions binders have become more popular as a partial cement substitute in recent years. Because of its huge yearly output as waste material and low cost, fly ash is now regarded as one of the most accessible choices. Fly ash-based construction materials have a lot of promise as cement substitutes because of their high performance and inexpensive cost. The purpose of this article is to study how fly ash affects the workability, setting time, compressive strength, and tensile strength of concrete. The kinds and characteristics of fly ash were also investigated.

Keywords: Fly Ash, Compressive Strength, Cement, Tensile Strength, Workability.

1. Introduction

Concrete is one of the most utilized "construction materials" due to its durability, accessibility, and strength (Berry, 2009). Globally, over ten billion tons of concrete are produced each year (Babor *et al.*, 2019). Concrete is made up of three basic ingredients: Portland cement (PC), aggregate, and water. Cement is manufactured by combining a variety of basic materials, such as clay and limestone, and heating them to high temperatures to cause chemical reactions. This process consumes huge quantities of energy (about 5% of global consumption each year) and emits massive volumes of carbon dioxide each year (Tafheem *et al.*, 2011). Many researchers have looked at using waste material to replace cement (Valipour *et al.*, 2016). The use of waste material instead of cement in a specified ratio reduces the cost of utilizing cement and allows the production of concrete with fewer environmental consequences and lower costs (Al-Zubaid *et al.*, 2017).

The amount of cement in the concrete mixture can be reduced by substituting alternative pozzolanic materials, which can function as a cement-like binder for some of it (Golewski, 2017). There is a wide range of waste materials that have pozzolanic properties and can be used to replace cement for example fly ash (FA) ground granulated blast furnace slag (GGBFS), silica fume (SF), and rice husk (RHA). These materials are known as supplementary cementitious materials (SCM). Consumption of industrial waste materials instead of cement in concrete manufacturing is an important factor in the conservation of the natural resources, environmental protection by reducing the negative effect of the waste on the environment and solving its disposal problems, energy-saving, and decrease the cost of concrete production (Kotwica *et al.*, 2017). In addition, utilization of waste material would cause a decrease in pollutant emissions from extracting, mining, and handling process (Tafheem *et al.*, 2011). SCM, such as fly ash, may be utilized to make green concrete instead of cement. Green concrete is described as concrete that employs natural and/or recyclable resources in its components to make concrete that is less harmful to the environment, has higher performance, is more durable, and is less expensive (Valipour *et al.*, 2016).

SCM comes in a variety of forms that can be used to partially replace cement in concrete production. The availability, durability, closeness, and cost considerations all factor into the decision to use SCM. One of the most popular waste products utilized as a cement substitute is fly ash (Tafheem *et al.*, 2011). It interacts chemically with water and calcium hydroxide formed during cement hydration, which is why it is only used as a partial substitute for cement. Fly ash concrete is a concrete product made by partially replacing cement with fly ash. The United States of America began developing fly ash as a component of Portland cement concrete in 1930. Fly ash is mostly composed of silica, alumina, and iron. Sodium, potassium, sulfur, magnesium, and Calcium are also found in fly ash (Tafheem *et al.*, 2011).

There are numerous advantages to using fly ash as a cement substitute in concrete, including reduced permeability, improved workability to strengthen the concrete, increased resistance to sulfate attack, reduced alkali-aggregate reaction, reduced crack development, and reduced cement hydration heat (Bhavana *et al.*, 2017). The goal of this study was to study how fly ash as a partial replacement for cement affects the workability, setting time, compressive strength, and tensile strength of concrete.

2. FLY ASH

Steel, iron, and thermal power facilities create fly ash, which is a solid waste product (Panda *et al.*, 2019) as shown in Figure 1. Iron, aluminum, calcium oxide, and silica make up most of the fly ash (Bagheri *et al.*, 2020). Fly ash reacts chemically with calcium hydroxide in concrete to create secondary calcium silicate, making it more durable and stronger than pure cement concrete (George *et al.*, 2012).

The hazardous chemicals present in fly ash are bound in concrete created with fly ash and cement, keeping them from polluting the environment. Fly ash as a cement substitute reduces CO_2 emissions as well as energy and resource use. It increases workability, reduces bleeding, and reduces body temperature (Liew *et al.*, 2020). It acts as a filler in concrete and helps to reduce overall voids (Krishnamoorthi & Kumar, 2013). To densify the matrix and make the concrete stronger and more durable, several construction companies have chosen to partially replace cement with pozzolanic materials such as fly ash (Liew *et al.*, 2020).

2.1 Types of Fly Ash

Due to differences in coal quality, the physical and chemical characteristics of fly ash can vary significantly from one power station to the next. The physical and cementitious characteristics of fly ash are influenced by the composition of the fly ash, the burning temperature, and the rate of cooling (Nath & Sarker, 2011). According to ASTM C 618 (Altwair & Kabir, 2010), fly ash is classified into two types: Class F and Class C. Table 1 (Altwair & Kabir, 2010; Rashad, 2015)shows the primary distinction between Class F and Class C.

Table 1. the main difference between Class F and Class C.

C FA	F FA
1- It is generated from the burning of sub-bituminous coal or lignite	1-It generated from burning bituminous and anthracite coal
2- It has high free lime	2-It has low free lime
3- It contains CaO of more than 10%	3- It contains CaO of less than 10%
4- The sum of three significant oxides (SiO_2, Al_2O_3, and Fe_2O_3) between 50% -70%	4-The sum of three significant oxides (SiO_2, Al_2O_3, and Fe_2O_3) more than 70%
5- It has cementitious properties	5- It has rarely cementitious properties
6- It is generally finer than F FA, because of the higher quantities of alkali sulfate in it.	6- It is generally bigger than C FA, due to the lesser quantities of alkali sulfate in it.

Figure 1. Fly ash powder.

2.2 Physical Properties

Glassy, spherical 'ball bearings', fly ash particles are finer than cement particles (Pitroda1 *et al.*, 2012). Individual fly ash particles range in size from 1 micron to 1 mm (Abushad & Sabri, 2017). Fly ash has a specific gravity (relative density) of 1.9 to 2.8. Blaine fineness (surface area) varies from 300 to 500 m^2/kg (Rashad, 2015). The physical characteristics of fly ash are listed in Table 2.

Table 2. physical properties of fly ash.

properties	(Berndt, 2009)	(Sahmaran *et al.*, 2009)	(Sahmaran *et al.*, 2009)	(Kayali & Ahmed, 2013)	(Memon *et al.*,2010)	(Marthong & Agrawal, 2012)	(Namagga & Atadero, 2009)	(Pati1 *et al.*, 2012)
Specific Gravity (g/cm^3)	**2.35**	**2.27**	**2.08**	**2.13**	**2.54**	**2.13**	**2.71**	-
Blaine fineness (m^2/kg)	341	306	289	310		330		340-360

2.3 Chemical Components

The main chemical components of fly ash are silica (SiO_2), iron (Fe_2O_3), alumina (Al_2O_3), and oxides of calcium (CaO). These chemicals components are responsible for their pozzolanic activity (Mohammadhosseini *et al.*, 2020). Table 3 presents the chemical components of fly ash.

Table 3. chemical components of fly ash.

Chemical Components %	(Nath & Sarker, 2011)	(Dhiyanesh *et al.*, 2013)	(Sathawane *et al.*, 2013)	(Namagga & Atadero , 2009)	(Berndt, 2009)	(Kayali, & Ahmed , 2013)	(Onera *et al.*, 2005)	(Mukherjee *et al.*, 2012)	(Sahmaran *et al.*, 2009)	(Sahmaran *et al.*, 2009)
CaO	**2.13**	**18.67**	**2.0**	**23.45**	**5.54**	**<1**	**2.10**	**0.59**	**10.07**	2.21
SiO_2	**50.50**	**45.98**	**40**	**39.76**	**47.58**	**67.5**	**57.55**	**64.58**	**48.08**	54.13
AI_2O_3	**26.57**	**23.55**	**25**	**14.31**	**26.42**	**23**	**25.16**	**25.89**	**25.87**	25.73
MgO	**1.54**	**1.54**	**3.71**		**0.90**	**<1**	**2.5**	**5.27**	**1.46**	2.12
Fe_2O_3	**13.77**	**4.91**	**6**	**5.56**	**12.19**	**4.5**	**6.5**	**0.26**	**4.54**	6.43
SO_3	**0.41**	**1.47**	**1.74**	**6.19**	**1.08**	**0.1**	**0.19**		**0.55**	0.11
K_2O	**0.77**	**1.8**	**0.80**		**1.9**	**1.5**	**3.65**	**0.041**	**1.22**	4.33
Na_2O_3	**0.45**	**0.24**	**0.96**		**1.5**	**0.5**	**0.66**	**0.027**	**0.73**	0.47
Loss on ignition (LOI)	0.6	2.31	3	1.65	2.20	1	1.66	2.4	1.01	1.34

3. Fresh Properties of Concrete

3.1 Workability

Concrete workability is described as the characteristic of concrete that influences how easy or difficult it is to mix, pour, consolidate, and finish fresh concrete. Slump flow diameter (D) and slump flow time (T50) are two popular measures for determining concrete workability.

The amount of water in the mix affects the workability of fly ash concrete, much as conventional concrete (Wattimena & Hardjito, 2017). Experiments were conducted out by (Sahmaran *et al.,* 2007) and (Sahmaran *et al.,* 2009) As demonstrated in Figure 2, increasing the substitution of PC with FA lowers the (water/ cementitious material (including PC & FA)) (w/cm) ratio. This is due to the lubricating effect of fly ash's spherical particle form and smooth surface, which decreases concrete's water requirement.

As demonstrated in Figures 3 and 4, (Dhiyaneshwaran *et al.*, 2013) and (Sahmaran *et al.*, 2009) conducted tests that indicate that workability (as assessed by D and t50) increases with increasing fly ash substitution up to a certain percentage, then gradually decreases, but remains higher than control concrete. This could be because the small size and

spherically shaped particles of fly ash reduce friction between cement paste and aggregates at low replacement levels (Bendapudi & Saha,2011) but as the percentage of fly ash replacement increases, the concrete's workability decreases due to the high surface area of fly ash in the concrete (Xu & Shi, 2018; Mukherjee *et al.*, 2013; Valdez, 2011).

The geometry and surface roughness of the FA (Sahmaran *et al.*, 2007), as well as the rate of PC replacement by FA (Xu & Shi, 2018), have a significant impact on the workability of fly ash concrete. On the other hand, it appears that variations in fly ash chemical composition have less of an impact on workability (Wattimena & Hardjito, 2017).

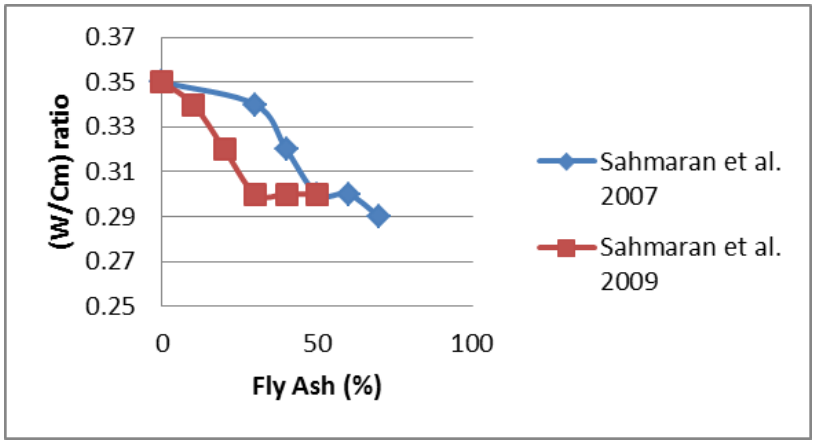

Figure 2. Effect of fly ash content on (w/cm) ratio.

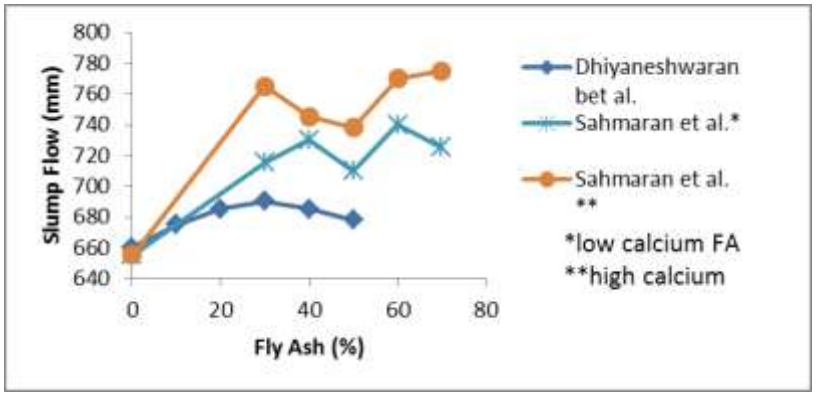

Figure 3. Effect of fly ash content on slump flow.

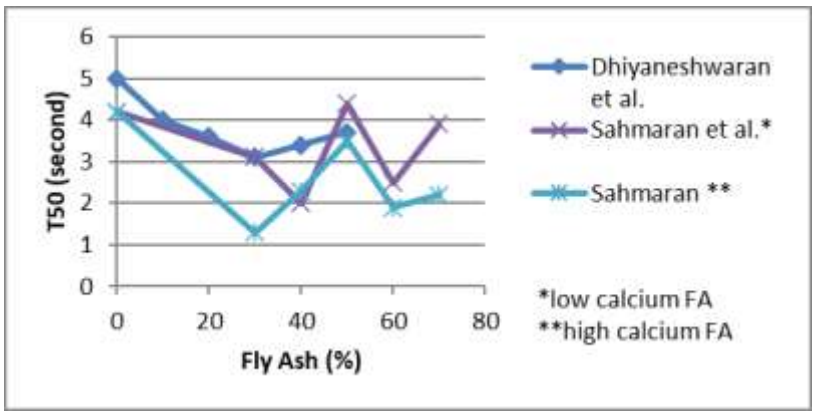

Figure 4. Effect of fly ash content on slump flow time (T50).

3.2 Setting Time

Setting time can be described as the time required for concrete to change from liquid state to solid state.. It is one of the most significant elements in fly ash concretes because it influences the characteristics of the hardened state in addition to the necessity for handling time before putting and compacting (Wattimena & Hardjito, 2017). In comparison

to identical concrete prepared without fly ash, fly ash tends to slow down the time it takes for cement to cure (Kesharwan *et al.*, 2017). In general, increasing the number of absorbed calcium ions, which prevents calcium ions concentration build-up in new paste during early hydration, increases the setting time of fly ash concrete. (Sahmaran *et al.*, 2009; Wang, 2004; Kocak & Nas, 2014). The features and quantities of fly ash used in concrete impact the time it takes for fly ash concrete to cure (Bendapudi & Saha,2011; Wang, 2004; Ravina & Mehta, 1986; Siddique, 2008). The use of Class F and Class C fly ashes extends the time it takes for concrete to set. Some kinds of C FA, on the other hand, can induce a fast setting (Wattimena & Hardjito, 2017; Siddique, 2008). According to (Marthong & Agrawal, 2012), when the cement particle size decreases, the setting time reduces. Because there is more surface area available for chemical interaction, the finer the cement, the faster it hydrates. Early hardness and strength development result because of this. The influence of fly ash on concrete setting behavior, according to previous studies, is dependent not only on the composition and quantity of fly ash used but also on the type and amount of cement used, as well as the water content (Siddique, 2008; Sata *et al.*, 2007).

4. Hardened Properties of Fly Ash

4.1 Compressive Strength

The most important test in concrete production is the compressive strength test due to two reasons. Firstly, it is an important test to assess many other properties of concrete. Secondly, it is an easy test to be determined. In fly ash concrete, the compressive strength is affected strongly by the chemical properties of fly ash particularly the content of CaO where high calcium fly ash reacts faster to provide better early age strength (Hemalathaa & Ramaswamy, 2017). Experimental works conducted by (Dhiyaneshwaran *et al.*, 2013) and (Namagga & Atadero, 2009) observed that concrete with fly ash had higher compressive strength than concrete without fly ash after 7 and 28 days. On the other hand, (Sahmaran *et al.,* 2009) discovered that concrete with fly ash had lower compressive strength than concrete without fly ash after 7 and 28 days. This discrepancy might be attributed to the differing ratios of CaO in FA utilized, with the first using fly ash with CaO content of 18.67 percent and 23.45 percent, respectively, and the latter using fly ash with a CaO concentration of 2.21 percent.

At the later age, the compressive strength of fly ash concrete is affected strongly by the content of sio_2 where it reacts with calcium hydroxide to form calcium silicate hydrate, which improves the compressive strength of fly ash concrete (Sata *et al.*, 2007).

From a variety of studies, Table 4 highlights the connection between compressive strength, rate of replacement of PC by FA, time, and (w/cm) ratio. Table 4 demonstrates that the compressive strength of fly ash concrete improves significantly over time when compared to normal concrete. Because of the pozzolanic reaction delay, the pace of strong development in fly ash concrete is sluggish. When calcium hydroxide (CH) is liberated from the cement hydration process, the pozzolanic reaction of fly ash begins. The early strength increase of concrete containing fly ash is hampered as a result of this (Shaikuthali *et al.*, 2019). However, other studies have found a substantial increase in compressive strength at an early age. This might be owing to the use of high Cao content fly ash (C FA), which contributes to strength development at an early age after mixing due to their self-hardening and pozzolanic characteristics. Table 4 further shows that with a high degree of replacement, compressive strength drops considerably. This may be related to the fact that fly ash functions as a pozzolanic ingredient in low-volume fly ash concrete. While only a portion of the fly ash in large volume fly ash concrete participates in the pozzolanic reaction, the other portion remains unreacted even after a lengthy period of curing (Rashad, 2015). According to previous studies, the compressive strength of fly ash concrete is affected by the amount of cement replacement, w/c ratio, and duration, in addition to the physical and chemical characteristics of the fly ash.

Table 4. Compressive strength of fly ash mixed concrete.

		Compressive Strength (MPa) of fly ash concrete at days						Reference
fly ash :cement	**w/cm ratio**	**7**	**28**	**56**	**90**	**180**	**365**	
0:100 10:90 20:80 30:70	0.35	23.18 26.33 25.93 22.08	39.07 43.11 40.59 30.92					(Wankhede & Fulari, 2014)
0:100 20:80 40:60	0.45	29.82 26.68 27.9	46 48.91 46.35	46.66 49.33 47.46				(Swaroop *et al.*, 2013)

0:100 10:90 20:80 30:70 40:60 50:50	According to Normal consistency	26.7 27.4 28.3 30.25 27.75 25.5	40.2 41.9 43.23 45.28 42.00 39.15					(Abushad & Sabri, 2017)
0:100 10:90 20:80 30:70 40:60 0:100 10:90 20:80 30:70 40:60	0.40 0.3 	28.77 21.33 16.15 13.04 9.93 34.81 29.33 13.78 13.04 8.59	44. 59 34.67 24.3 22.22 17.33 52.74 38.22 27.56 21.48 20					(Pitroda1 *et al.*, 2012)
0:100 15:85 25:75 35:65 45:55 55:45 65:35 0:100 15:85 25:75 35:65 45:55 55:45 65:35	According to Normal consistency	25 24 18 19 15 10 6 38 37 24 25 28 24 9	46 43 39 37 29 21 14 57 56 54 51 48 41 32	50 47 41 40 32 30 20 61 60 59 55 50 45 37				(Chakraborty & Banerjee , 2016)
0:100 30:70 40:60 50:50 60:40 70:30 0:100 30:70 40:60 50:50 60:40 70:30	0.35 0.32 	55.9 40.6 37.4 24.5 21.9 14.9 55.9 38.6 34.5 32 22.8 18.3	62.2 57.3 59.1 40.8 38.1 34.4 62.2 52.4 52.3 47.5 39.9 32.8		69.9 64.9 61.5 47.1 48.8 39.4 69.9 64.9 63.2 59.9 52.1 45	71 66.2 68.3 51 51.7 43 71 69.2 67.2 68.7 62.6 53.7	74.1 70.7 67.3 54.6 56.4 51.8 74.1 75.6 75.6 70 65.8 61.6	(Sahmaran *et al.*, 2009)
0:100 25:75 45:55 0:100 25:75 45:55	0.24 0.19 	79.5 74.6 56.3 83.5 74.2 56.4	97.4 105.9 89.4 96.8 102.3 88.5		110.2 124.5 107.2 114.5 123.6 109.2			(Poon *et al.*, 2000)

0:100 10:90 20:80 30:70 40:60 50:50	According to Normal consistency	19.4 21.4 22.6 25.0 26.5 27.2	26.4 28.2 30.8 34.9 38.9 40.0	29.0 31.2 34.0 40.2 44.6 46.3	31.0 34.2 38.0 44.0 49.8 51.4		32.8 36.3 40.5 46.4 52.3 54.8	(Siddique, 2003)

4.2 Splitting Tensile Strength

The size and extent of fractures in concrete are influenced by the tensile strength of the concrete. The most significant element affecting tensile strength is paste quality, which is influenced by fine aggregate characteristics (Mehtaa & Ashishb, 2019). The behavior of concrete's splitting tensile strength is like that of its compressive strength, although it is much lower. Table 5 summarizes the connection between splitting tensile strength, rate of replacement of PC by FA, time, and (w/cm) ratio for many investigations. As shown in table 5, the splitting tensile strength of fly ash concretes appeared to be greater than that of control concrete since the grain and pore refinement of concrete resulted from the fineness of particles and the pozzolanic reaction of the ashes. However, it has been shown that tensile strength rises with increasing fly ash content up to a specific percentage and declines at high levels of replacement in some situations. This might be because the fly ash enhances the interfacial connection between the aggregate and the paste in a low-volume fly ash concrete. The fly ash, on the other hand, reduces the interfacial connection between the aggregate and the paste in high-volume fly ash concrete (Dhiyaneshwaran, 2013; Magureanu and Negrutiu, 2009). Table 5 further shows that the splitting tensile strength of all mixtures continued to grow with age (Siddique, 2003).

Table 5. Splitting Tensile Strength of fly ash mixed concrete.

		Splitting Tensile Strength (MPa) of fly ash concrete at days					Reference
fly ash :cement	**w/cm ratio**	**7**	**28**	**56**	**90**	**365**	
0:100 10:90 15:85 20:80 30:70 40:60	According to Normal consistency		1.72 1.58 1.58 0.89 1.21 0.89				(Barbuta *et al.*, 2016)
0:100 10:90 20:80 30:70 40:60 0:100 10:90 20:80 30:70 40:60	0.4 0.3			3.44 3.52 3.21 2.55 2.41 3.96 4.1 2.78 2.69 2.04			(Pitroda1 *et al.*, 2012)
0:100 10:90 20:80 30:70 40:60 50:50	According to Normal consistency	1.08 1.23 1.34 1.47 1.36 1.28	1.74 1.88 2.01 2.06 1.96 1.84				(Dhiyaneshwaran *et al.*, 2013)
0:100 10:90 20:80 30:70 40:60 50:50	0.49	2.5 2.6 2.6 2.7 2.8 2.7	3.0 3.1 3.2 3.4 3.5 3.5	3.2 3.3 3.4 3.7 3.9 4.0	3.3 3.5 3.6 4.0 4.2 4.3	 3.4 3.6 3.8 4.2 4.4 4.4	(Poon *et al.*, 2000)

5. Conclusions

Based on the discussion above, the following conclusions were drawn:

1- The use of fly ash in concrete reduces water content up to a certain limit, if you keep increasing the FA percentage in concrete water demand increases to maintain the required workability.

2- The workability of fly ash concrete is affected by the geometry and surface roughness of the FA.

3- The chemical composition of the fly ash has a lesser impact on workability, but it has a greater impact on setting time.

4- The optimal content of fly ash in concrete depends on its physical and chemical properties

5- The value of compressive strength and tensile strength depends on the level of cement replacement, type of FA, and age.

6- The behavior of concrete's splitting tensile strength is like that of its compressive strength.

Reference

Abushad, M., & Sabri, M. D. (2017). Comparative study of compressive strength of concrete with fly ash replacement by cement. *International Research Journal of Engineering and Technology*, *4*(07), 2627-2630.

Altwair, N. M., & Kabir, S. (2010, June). Green concrete structures by replacing cement with pozzolanic materials to reduce greenhouse gas emissions for sustainable environment. In *6th International Engineering and Construction Conference, Cairo, Egypt* (pp. 269-279).

AL-Zubaid, A. B., Shabeeb, K. M., & Ali, A. I. (2017). Study the effect of recycled glass on the mechanical properties of green concrete. *Energy procedia*, *119*, 680-692.

Bagheri, S. M., Koushkbaghi, M., Mohseni, E., Koushkbaghi, S., & Tahmouresi, B. (2020). Evaluation of environment and economy viable recycling cement kiln dust for use in green concrete. *Journal of Building Engineering*, *32*, 1-11.

Barbuta, M., Bucur, R., Serbanoiu, A. A., Scutarasu, S., & Burlacu, A. (2016). Combined effect of fly ash and fibers on properties of cement concrete. *Procedia Engineering*, *181*, 280-284.

Bendapudi, S. C. K., & Saha, P. (2011). Contribution of fly ash to the properties of mortar and concrete. *International Journal of Earth Sciences and Engineering*, *4*(6), 1017-1023.

Berndt, M. L. (2009). Properties of sustainable concrete containing fly ash, slag and recycled concrete aggregate. *Construction and building materials*, *23*(7), 2606-2613.

Berry, M., Cross, D., & Stephens, J. (May 2009). Changing the Environment: An Alternative Green Concrete Produced without Portland Cement. *2009 World of Coal Ash (WOCA) Conference*. Lexington, KY, USA. Retrieved from *http://www.flyash.info/2009/130-berry2009.pdf*.

Bhavana, R. S., Raju, P. P., & Asadi, S. S. (2017). Experimental Study on Bacterial Concrete with Partial Replacement of Cement by Fly Ash. *International Journal of Civil Engineering and Technology*, *8*(4), 201-209.

Chakraborty, J., & Banerjee, S. (2016). Replacement of Cement by Fly Ash in Concrete. *SSRG International J. of Civil Engineering*, *3*(8), 58-60.

Dhiyaneshwaran, S., Ramanathan, P., Baskar, I., & Venkatasubramani, R. (2013). Study on durability characteristics of self-compacting concrete with fly ash. *Jordan journal of civil engineering*, *7*(3), 342-352.

George, R. P., Vishwakarma, V., Samal, S. S., & Mudali, U. K. (2012). Current understanding and future approaches for controlling microbially influenced concrete corrosion: a review. *Concrete research letters*, *3*(3), 491-506.

Golewski, G. L. (2018). Green concrete composite incorporating fly ash with high strength and fracture toughness. *Journal of Cleaner Production*, *172*, 218-226.

Grădinaru, C. M., Şerbănoiu, A. A., Babor, D. T., Sârbu, G. C., Petrescu-Mag, I. V., & Grădinaru, A. C. (2019). When agricultural waste transforms into an environmentally friendly material: The case of green concrete as alternative to natural resources depletion. *Journal of Agricultural and Environmental Ethics*, *32*(1), 77-93.

Hemalatha, T., & Ramaswamy, A. (2017). A review on fly ash characteristics–Towards promoting high volume utilization in developing sustainable concrete. *Journal of cleaner production*, *147*, 546-559.

Kayali, O., & Ahmed, M. S. (2013). Assessment of high volume replacement fly ash concrete–Concept of performance index. *Construction and Building Materials*, *39*, 71-76.

Kesharwani, K. C., Biswas, A. K., Chaurasiya, A., & Rabbani, A. (2017). Experimental study on use of fly ash in concrete. *Int. Res. J. Eng. Technol*, *4*(9), 1527-1530.

Kocak, Y., & Nas, S. (2014). The effect of using fly ash on the strength and hydration characteristics of blended cements. *Construction and Building Materials*, *73*, 25-32.

Kotwica, Ł., Pichór, W., Kapeluszna, E., & Różycka, A. (2017). Utilization of waste expanded perlite as new effective supplementary cementitious material. *Journal of Cleaner production*, *140*, 1344-1352.

Krishnamoorthi, A., & Kumar, G. M. (2013). Properties of green concrete mix by concurrent use of fly ash and quarry dust. *IOSR Journal of Engineering*, *3*(8), 48-54.

Liew, M. S., Nguyen-Tri, P., Nguyen, T. A., & Kakooei, S. (Eds.). (2019). *Smart Nanoconcretes and Cement-Based Materials: Properties, Modelling and Applications*. Elsevier.

Magureanu, C., & Negrutiu, C. (2009, June). Performance of concrete containing high volume coal fly ash-green concrete. In *Proceedings 4th International Conference on Computational Methods and Experiments in Material Characterisation*,64,373-379.

Marthong, C., & Agrawal, T. P. (2012). Effect of fly ash additive on concrete properties. *International Journal of Engineering Research and Applications*, *2*(4), 1986-1991.

Mehta, A., & Ashish, D. K. (2019). Silica fume and waste glass in cement concrete production: A review. *Journal of Building Engineering*, *29*, 1-18.

Memon, F. A., Memon, N. A., Memon, R. A., URSANI, A. A., UMRANI, A. W., UMRANI, F. A., ... & MEMON, H. M. (2010). Study of compressive strength of concrete with coal power plant fly ash as partial replacement of cement and fine aggregate. *Mehran University Research Journal of Engineering & Technology*, *29*(4), 647-652.

Mohammadhosseini, H., Alyousef, R., Lim, N. H. A. S., Tahir, M. M., Alabduljabbar, H., Mohamed, A. M., & Samadi, M. (2020). Waste metalized film food packaging as low cost and ecofriendly fibrous materials in the production of sustainable and green concrete composites. *Journal of Cleaner Production*, *258*, 1-15.

Muhit, I. B., Ahmed, S. S., Amin, M. M., & Raihan, M. T. (2013, December). Effects of silica fume and fly ash as partial replacement of cement on water permeability and strength of high performance concrete. In *4th International Conference on Advances in Civil Engineering, AETACE, Association of Civil and Environmental Engineers*.

Mukherjee, S., Mandal, S., & Adhikari, U. B. (2012). Study on the physical and mechanical property of ordinary portland cement and fly ash paste. *International Journal of Civil & Structural Engineering*, *2*(3), 731-736.

Mukherjee, S., Mandal, S., & Adhikari, U. B. (2013). Comparative study on physical and mechanical properties of high slump and zero slump high volume fly ash concrete (HVFAC). *Global NEST J*, *20*(10), 1-7.

Namagga, C., & Atadero, R. A. (2011). Optimization of fly ash in concrete. High lime fly ash as a replacement for cement and filler material. World of Coal Ash Conference (WOCA), Lexington, USA, 4-7 May, 2009.

Nath, P., & Sarker, P. (2011). Effect of fly ash on the durability properties of high strength concrete. *Procedia Engineering*, *14*, 1149-1156.

Oner, A. D. N. A. N., Akyuz, S., & Yildiz, R. (2005). An experimental study on strength development of concrete containing fly ash and optimum usage of fly ash in concrete. *Cement and Concrete Research*, *35*(6), 1165-1171.

Panda, S., Panigrahi, R., & Narshimam, M. L. (2019). A review on utilization of alkali activated flyash and ggbfs as green concrete. *Adalya Journal*, 8(7), 91-96.

Pati1, S. , J. N. Kale, J. N. , & Suman, S. (2012). Fly Ash Concrete : A Technical Analysis for Compressive Strength. *International Journal of Advanced Engineering Research and Studies*, 2(1), 128-129.

Pitroda1, J. , Zala , L.B., & Umrigar, F.S. (2012). Experimental Investigations on Partial Replacement of Cement with Fly Ash in Design Mix Concrete. International Journal of Advanced Engineering Technology, 3(4), 126-129.

Poon, C. S., Lam, L., & Wong, Y. L. (2000). A study on high strength concrete prepared with large volumes of low calcium fly ash. *Cement and concrete research*, *30*(3), 447-455.

Rashad, A. M. (2015). A brief on high-volume Class F fly ash as cement replacement–A guide for Civil Engineer. *International Journal of Sustainable Built Environment*, *4*(2), 278-306.

Ravina, D., & Mehta, P. K. (1986). Properties of fresh concrete containing large amounts of fly ash. *Cement and Concrete Research*, *16*(2), 227-238.

Şahmaran, M., Yaman, İ. Ö., & Tokyay, M. (2009). Transport and mechanical properties of self consolidating concrete with high volume fly ash. *Cement and concrete composites*, *31*(2), 99-106.

Sahmaran,M., Yaman, O.,& Tokyay,M. (2007). Development of high-volume low-lime andmhigh-lime fly-ash-incorporated self-consolidating concrete. *Magazine of Concrete Research*, 59(2), 97-106.

Sata, V., Jaturapitakkul, C., & Kiattikomol, K. (2007). Influence of pozzolan from various by-product materials on mechanical properties of high-strength concrete. *Construction and Building Materials*, *21*(7), 1589-1598.

Sathawane, S. H., Vairagade, V. S., & Kene, K. S. (2013). Combine effect of rice husk ash and fly ash on concrete by 30% cement replacement. *Procedia Engineering*, *51*, 35-44.

Shaikuthali, S. A. , Mannan, M. A. , Ahmadi, R. , & Ismail, I. (2019). Workability and compressive strength properties of normal weight concrete using high dosage of fly ash as cement replacement. 4(26), 1-7.

Siddique, R. (2003). Effect of fine aggregate replacement with Class F fly ash on the mechanical properties of concrete. *Cement and Concrete research*, *33*(4), 539-547.

Siddique, R. (2007). *Waste materials and by-products in concrete*. Springer Science & Business Media.

Swaroop, A.H.L., Venkateswararao, K.,& Kodandaramarao, P . (2013). Durability Studies On Concrete With Fly Ash & Ggbs. *Engineering Research and Applications (IJERA)*, 3(4), 285-289.

Tafheem, Z., Khusru, S., & Nasrin, S. (December 2011). Environmental Impact of Green Concrete in Practice. *International Conference on Mechanical Engineering and Renewable Energy 2011*. Chittagong, Bangladesh.

Valdez, P. (2011). Evaluation of sustainable high volume fly ash concretes. Cement & Concrete Composites, 33(1), 39-45.

Valipour, M., Shekarchi, M., & Arezoumandi, M. (2016). Chlorine Diffusion Resistivity of Sustainable Green Concrete in Harsh Marine Environments. *Journal of Cleaner Production*, *142*, 4092-4100.

Wang, K. (Ed.). (2004). *Proceedings of the International Workshop on Sustainable Development and Concrete Technology, Beijing, China, May 20-21, 2004*. Center for Transportation Research and Education Iowa State University.

Wankhede, P. R. & Fulari, V. A. (2014). Effect of Fly ASH on Properties of Concrete. *International Journal of Emerging Technology and Advanced Engineering*, 4(7), 284-289.

Wattimena, O.K. & Hardjito, D. (2017). A Review on the Effect of Fly Ash Characteristics and Their Variations on the Synthesis of Fly Ash Based Geopolymer. *in AIP Conference Proceedings*, 1-12.

Wattimena, O. K., Antoni, & Hardjito, D. (2017, September). A review on the effect of fly ash characteristics and their variations on the synthesis of fly ash based geopolymer. In *AIP Conference Proceedings* (Vol. 1887, No. 1, p. 020041). AIP Publishing LLC.

Xu, G., & Shi, X. (2018). Characteristics and applications of fly ash as a sustainable construction material: A state-of-the-art review. *Resources, Conservation and Recycling*, *136*, 95-109.

Research Article

A New Method for Solving Interval and Fuzzy Quadratic Equations of Dual Form

Kamal Mamehrashi *

Mathematics Unit, School of Science and Engineering, University of Kurdistan Hewlêr, Erbil, KRG, Iraq.

E-mail: kamal.mamehrashi@ukh.edu.krd

Access this article online		
Received on: September 26, 2021	**Accepted on:** November 4, 2021	**Published on:** December 28, 2021
DOI: 10.25079/ukhjse.v5n2y2021.pp81-89	**E-ISSN:** 2520-7792	

Abstract

In this paper, a numerical method for solving a quadratic interval equation of dual form is presented. The idea for the method is based on the generalized procedure of interval extension called "interval extended zero" method. It is stated that the solution of interval quadratic equation based on the presented method may be naturally treated as a fuzzy number. An important advantage of the proposed approach is that it substantially decreases the excess width defect. Three numerical examples are included to demonstrate the applicability and validity of the presented method.

Keywords: Extended Zero, Dual Equation, Interval Arithmetic, Fuzzy Equations, Uncertainty Theory.

1. Introduction

In 1975-1978, for first time the authors of (Zadeh, 1975) and (Dubios & Prade, 1978) introduced the concept of fuzzy number and fuzzy arithmetic operations. The reader can find more information on fuzzy numbers and fuzzy arithmetic in (Kaufman & Gupta, 1985) and (Zadeh, 1965). Now, there are many inherent application of fuzzy systems to study a variety of problems such as mathematics, engineering (Chen & Yang, 2000), finance (Buckley, 1987), (Calzi, 1990), economics (Buckley, 1992), (Wu & Chang, 2003) and social sciences which polynomials play a major role in those areas.

One of the important applications of fuzzy number arithmetic is handling fuzzy linear systems and fully fuzzy linear systems. In the studies (Abbasbandy & Ezzati ,2006), (Abbasbandy & Otadi, 2006), (Ferreira *et al.*, 2005), (Mosleh & Otadi, 2010) and (Shieh, 2008) there are some efforts to find the numerical solution of fuzzy polynomial equation such as

$$a_1x + a_2x_2 + \cdots + a_nx_n = a_0,$$

such that $a_0, a_1, \dots, a_n$ are fuzzy numbers. In (Allahviranloo *et al.*, 2007), the authors also presented a method for solving fuzzy nonlinear equations. Furthermore, the authors of (Muzziloi & Reynaerts, 2006) studied the fully fuzzy linear systems of the form

$$A_1x + b_1 = A_2x + b_2,$$

such that A_1, A_2 are square matrices of fuzzy coefficients and b_1, b_2 are fuzzy number vectors. In (Dehghan *et al.*, 2007), the iterative methods are utilized for the fully fuzzy linear systems of the form $Ax = b$ which A is a fuzzy matrix and b is a fuzzy vector.

Additionally, based on a new arithmetic calculation, Mosleh (Mosleh *et al.*, 2008) studied the general duality fully fuzzy linear systems of the form

$$Ax + b = Cx + d,$$

where A and C are square matrices of fuzzy coefficients and b, d are fuzzy numbers.

In 2009, a new method to the solution of interval and fuzzy equations based on the generalized procedure of the interval and fuzzy extension is proposed in (Seastjanov & Dymova, 2009). The key idea is the treatment of the interval zero as an interval centered around zero. It is shown that such proposition is not of heuristic nature, but is the direct consequence of the interval subtraction and division operations.

The authors in (Movahedian *et al.*, 2009) applied this method for solving the linear interval equation in dual form

$$ax = bx + c,$$

where a, b, c are intervals.

The restricted variation method and optimization method have been used for solving the fully fuzzy equations of the form $\tilde{A}\tilde{X}^2 + \tilde{B}\tilde{X} + \tilde{C} = \tilde{D}$ in (Moazam, 2016) and (Allahviranloo & Moazam, 2014), respectively. In (Landoweski, 2017), the RDM interval method is utilized for solving quadratic interval equation. The interval extended zero method is applied to the solution of nonlinear interval and fuzzy equations which includes the form $ax^2 + bx = c$ in (Dymova & Seastjanov, 2018).

Since in the case of the α-cut presentation, fuzzy arithmetic is based on the interval arithmetic rules, the basic definitions of applied interval analysis should also be presented. One of the most inconvenient features of interval arithmetic is the fast increasing of width of intervals obtained as the results of interval calculations. To reduce this undesirable effect, several different modifications of interval arithmetic were proposed.

In this paper, the idea of interval extended zero method is applied for solving the quadratic equation of the dual form

$$ax^2 + bx + c = dx^2 + ex + f,$$

where the coefficients are interval numbers.

Usually, there is no additive inverse element for an arbitrary fuzzy number $u \in E$ (Lai & Hwang, 1992), i.e., there exists no element $v \in E$ such that $u + v = 0$, so it is assumed that two equations

$$ax^2 + bx + c = dx^2 + ex + f,$$

and

$$ax^2 + bx + c - dx^2 - ex - f = 0,$$

are not equivalent, therefore the term 0 in the right hand side of the last equation as is taken an interval centered at zero and then can deal with these two equations as equivalent ones.

The key to the suggested scheme is the observation that the zero value in interval discussion does not mean "nothing" and a more natural is the handling of the interval zero as an interval centred around zero. This assumption allows us to avoid formally what we have as "interval equation's right hand side problem" and to use the classical technique to the solution of the quadratic equations of the dual form.

The rest of the paper is organized as follows. Section 2 is devoted to some preliminaries are needed in subsequent development. The suggested method for solving the quadratic equation of the dual form is presented in section 3. In section 4, three numerical examples are considered to demonstrate the performance of the presented method. Finally, the paper ends with conclusion in section 5.

2. Preliminaries

This section consists of the problem statement, some basic definitions and properties in fuzzy arithmetic and the base of the interval extended zero method.

2.1. Problem statement

Consider the equation

$$ax^2 + bx + c = dx^2 + ex + f.$$

This equation is an arbitrary duality form of quadratic equation, where

$$a = [\underline{a}, \overline{a}], b = [\underline{b}, \overline{b}], c = [\underline{c}, \overline{c}], d = [\underline{d}, \overline{d}], e = [\underline{e}, \overline{e}], f = [\underline{f}, \overline{f}],$$

and for simplicity, assume

$$\underline{a}, \overline{a} \geq 0, \underline{b}, \overline{b} \geq 0, \underline{c}, \overline{c} \geq 0, \underline{d}, \overline{d} \geq 0, \underline{e}, \overline{e} \geq 0, \underline{f}, \overline{f} \geq 0, a \neq d.$$

2.2. Fuzzy arithmetic

Let us recall some basic principles of fuzzy arithmetic needed for our further analysis. As the direct outcome of the basic definition, the following expressions were obtained (Alefeld & Herzberger, 1983).

$$[x] + [y] = [\underline{x} + \underline{y}, \overline{x} + \overline{y}],$$
$$[x] - [y] = [\underline{x} - \overline{y}, \overline{x} - \underline{y}],$$

$$[x] * [y] = \left[\min\left\{\underline{x}\underline{y}, \underline{x}\overline{y}, \overline{x}\underline{y}, \overline{x}\overline{y}\right\}, \max\left\{\underline{x}\underline{y}, \underline{x}\overline{y}, \overline{x}\underline{y}, \overline{x}\overline{y}\right\}\right]$$
$$\frac{[x]}{[y]} = [\underline{x}, \overline{x}] * \left[\frac{1}{\overline{y}}, \frac{1}{\underline{y}}\right], 0 \notin [y].$$

2.3. The idea of interval extended zero method

The technique of interval extended zero method for solving interval equations is based on the fuzzy extension principle (Chalco-Cano *et al.*, 2007) which has been developed in (Seastjanov & Dymova, 2007) and (Seastjanov & Dymova, 2009). The values of uncertain parameters in an equation are substituted for corresponding intervals or fuzzy values and all arithmetic operations are substituted for relevant interval fuzzy operations. In general, for an arbitrary form of membership function the technique of fuzzy-interval calculations is based on the representation of initial fuzzy intervals in form of so-called α-cut (Hanss, 2005), (Dutta *et al.*, 2011) which are the intervals associated with the corresponding degrees of membership. All calculations are made with those α-cut according to the well known interval arithmetic rules and the resulting fuzzy intervals are obtained as the set of the corresponding final α-cut.
Consider the non-interval algebraic equation

$$g(x) = 0.$$

The interval extension of the equation is obtained by replacement of all variables and arithmetic operations with intervals and relevant interval operations, respectively. As a result, we can present an interval equation as $[g]([x]) = 0$. In this equation, the right part is non interval degenerated the zero value, whereas the left part has an interval value form. Clearly, if $[g]([x]) = [\underline{g}, \overline{g}]$, then the equation $[g]([x]) = 0$ is correct only if $\overline{g} = \underline{g} = 0$. In conventional interval analysis, it is usually assumed any interval containing zero may be considered as "interval zero". Here, an operation of "interval zero extension" is proposed to obtain "interval zero" in the right side of the question. To aim this, let us look at the problem from another point of view. We can define the result of operation $[c] - [c]$ as an "interval zero", where $[c]$ is an interval. Then, we get

$$[\underline{c}, \overline{c}] - [\underline{c}, \overline{c}] = [\underline{c} - \overline{c}, \overline{c} - \underline{c}].$$

So the result of interval subtraction $[c] - [c]$ is an interval centered around zero. As a result, what we can say for the equation $g(x) = 0$ is that the right hand side should be a symmetric interval with respect to zero with not defined width. Therefore, we can assume zero as $[-y, y]$ which is an interval centered around zero. This is the reason why this scheme is called interval extended zero (Dymova, 2007).

3. Solution of the equation by interval extended zero method

Consider the following quadratic algebraic equation

$$ax^2 + bx + c = dx^2 + ex + f. \quad (1)$$

Assuming the uncertain parameters, Eq.1 can be rewritten to its interval form as

$$[\underline{a}, \overline{a}][\underline{x}^2, \overline{x}^2] + [\underline{b}, \overline{b}][\underline{x}, \overline{x}] + [\underline{c}, \overline{c}] = [\underline{d}, \overline{d}][\underline{x}^2, \overline{x}^2] + [\underline{e}, \overline{e}][\underline{x}, \overline{x}] + [\underline{f}, \overline{f}]. \quad (2)$$

Then by manipulating Eq.2, one may write

$$[\underline{a}\underline{x}^2, \overline{a}\overline{x}^2] + [\underline{b}\underline{x}, \overline{b}\overline{x}] + [\underline{c}, \underline{c}] + [-\overline{d}\overline{x}^2, -\underline{d}\underline{x}^2] + [-\overline{e}\overline{x}, \underline{e}\underline{x}] + [-\overline{f}, -\underline{f}] = [-y, y], \quad (3)$$

and hence the following two equations are obtained

$$\underline{a}\underline{x}^2 + \underline{b}\underline{x} + \underline{c} - \overline{d}\overline{x}^2 - \overline{e}\overline{x} - \overline{f} = -y,$$
$$\overline{a}\overline{x}^2 + \overline{b}\overline{x} + \overline{c} - \underline{d}\underline{x}^2 - \underline{e}\underline{x} - \underline{f} = y. \quad (4)$$

Summing up both sides of Eq.4 implies

$$\underline{a}\underline{x}^2 + \underline{b}\underline{x} + \underline{c} - \overline{d}\overline{x}^2 - \overline{e}\overline{x} - \overline{f} + \overline{a}\overline{x}^2 + \overline{b}\overline{x} + \overline{c} - \underline{d}\underline{x}^2 - \underline{e}\underline{x} - \underline{f} = 0. \quad (5)$$

To solve Eq.5, firstly we assume that $\underline{x} = \overline{x} = x_m$, therefore

$$(\underline{a} - \overline{d} + \overline{a} - \underline{d})x_m^2 + (\underline{b} - \overline{e} + \overline{b} - \underline{e})x_m + (\underline{c} - \overline{f} + \overline{c} - \underline{f}) = 0. \quad (6)$$

Thanks to the classical method for solving an algebraic quadratic equation form, the data parameter is computed as

$$\Delta = (\underline{b} - \overline{e} + \overline{b} - \underline{e})^2 - 4(\underline{a} - \overline{d} + \overline{a} - \underline{d})(\underline{c} - \overline{f} + \overline{c} - \underline{f}). \quad (7)$$

The Eq.6 is a quadratic form, therefore to find the solution, the following three cases, according to value of Δ parameter, are considered.

Case 1: $\Delta > 0$.

The Eq.6 has two roots as following

$$x_{m1}, x_{m2} = \frac{-(\underline{b} - \overline{e} + \overline{b} - \underline{e}) \pm \sqrt{\Delta}}{2(\underline{a} - \overline{d} + \overline{a} - \underline{d})}. \quad (8)$$

Without loss of generality, let $x_{m1} < x_{m2}$, therefore x_{m1} is the lower and upper bound for $\overline{x}_{m1}$ and $\underline{x}_{m1}$, respectively. Similarly, x_{m2} is the lower and upper bound for $\underline{x}_{m2}$ and $\overline{x}_{m2}$, respectively. Next, we try to find the lower bounds for $\underline{x}_{m1}$ and $\underline{x}_{m2}$ and the upper bounds for $\overline{x}_{m1}$ and $\overline{x}_{m2}$.

Applying the fuzzy arithmetic for Eq.2, the following equation is obtained.

$$[\underline{a} - \overline{d}, \overline{a} - \underline{d}][\underline{x}^2, \overline{x}^2] + [\underline{b} - \overline{e}, \overline{b} - \underline{e}][\underline{x}, \overline{x}] + [\underline{c} - \overline{f}, \overline{c} - \underline{f}] = 0. \quad (9)$$

Therefore, Eq.9 is rewritten as

$$\begin{aligned} (\underline{a} - \overline{d})\underline{x}^2 + (\underline{b} - \overline{e})\underline{x} + (\underline{c} - \overline{f}) = 0, \\ (\overline{a} - \underline{d})\overline{x}^2 + (\overline{b} - \underline{e})\overline{x} + (\overline{c} - \underline{f}) = 0. \end{aligned} \quad (10)$$

The delta parameters are computed for both equations of Eq.10 as

$$\begin{aligned} \Delta\overline{x} = (\underline{b} - \overline{e})^2 - 4(\underline{a} - \overline{d})(\underline{c} - \overline{f}), \\ \Delta\underline{x} = (\overline{b} - \underline{e})^2 - 4(\overline{a} - \underline{d})(\overline{c} - \underline{f}). \end{aligned} \quad (11)$$

Based on the obtained values for $\Delta\overline{x}$ and $\Delta\underline{x}$, the following options are considered.

(I) $\Delta\underline{x} > 0$ and $\Delta\overline{x} > 0$.

In this case, two equations in (10) have two answers like $\underline{x}_1, \underline{x}_2$ and $\overline{x}_1, \overline{x}_2$. Thus, we have

$$\begin{aligned} [\underline{x}_{m1}] = [\underline{x}_1, x_{m1}], \quad [\overline{x}_{m1}] = [x_{m1}, \overline{x}_1], \\ [\underline{x}_{m2}] = [\underline{x}_2, x_{m2}], \quad [\overline{x}_{m2}] = [x_{m2}, \overline{x}_2], \end{aligned} \quad (12)$$

where $\underline{x}_1 < \underline{x}_2$ and $\overline{x}_1 < \overline{x}_2$.

Notice that if $\overline{x}_1 < x_{m1}$ or $\underline{x}_2 > x_{m2}$, set

$$[\overline{x}_{m1}] = \left[x_{m1}, \frac{x_{m1} + x_{m2}}{2}\right], \quad [\underline{x}_{m2}] = \left[\frac{x_{m1} + x_{m2}}{2}, x_{m2}\right]. \quad (13)$$

(II) $\Delta\underline{x} = 0$ and $\Delta\overline{x} = 0$

Let the roots of two equations in (10) be as $\underline{x}_1 = \underline{x}_2 = \underline{x}_{12}$ and $\overline{x}_1 = \overline{x}_2 = \overline{x}_{12}$. If $\underline{x}_{12} < x_{m1}$ then

$$[\underline{x}_{m1}] = [\underline{x}_{12}, x_{m1}], \quad [\underline{x}_{m2}] = \left[\frac{x_{m1} + x_{m2}}{2}, x_{m2}\right]. \quad (14)$$

On the other hand if $x_{m1} < \underline{x}_{12} < x_{m2}$ then

$$[\underline{x}_{m1}] = [x_{m1}, x_{m1}], \quad [\underline{x}_{m2}] = [x_{12}, x_{m2}]. \quad (15)$$

If $\underline{x}_{12} > x_{m2}$, let

$$[\underline{x}_{m1}] = [x_{m1}, x_{m1}], \quad [\underline{x}_{m2}] = \left[\frac{x_{m1} + x_{m2}}{2}, x_{m2}\right]. \quad (16)$$

For the case $\overline{x}_{12} > x_{m2}$, then

$$[\overline{x}_{m1}] = \left[x_{m1}, \frac{x_{m1} + x_{m2}}{2}\right], \quad [\overline{x}_{m2}] = [x_{m2}, \overline{x}_{12}]. \quad (17)$$

If $x_{m1} < \overline{x}_{12} < x_{m2}$, let

$$[\underline{x}_{m1}] = [x_{m1}, x_{m1}], \quad [\overline{x}_{m1}] = [x_{m1}, \overline{x}_{12}], \quad [\overline{x}_{m2}] = [x_{m2}, x_{m2}], \quad (18)$$

and if $\overline{x}_{12} < x_{m1}$, then the interval solutions are

$$[\overline{x}_{m1}] = \left[x_{m1}, \frac{x_{m1} + x_{m2}}{2}\right], \quad [\overline{x}_{m2}] = [x_{m2}, x_{m2}]. \quad (19)$$

(III) $\Delta\underline{x} < 0$ and $\Delta\overline{x} < 0$.

The two equations in (10) have no real roots, so as a result, set

$$[\underline{x}_{m1}] = [x_{m1}, x_{m1}],\ \ [\overline{x}_{m1}] = \left[x_{m1}, \frac{x_{m1}+x_{m2}}{2}\right], \tag{20}$$

$$[\underline{x}_{m2}] = \left[\frac{x_{m1}+x_{m2}}{2}, x_{m21}\right], \qquad [\overline{x}_{m2}] = [x_{m2}, x_{m2}].$$

The other cases for $\Delta\underline{x}$ and $\Delta\overline{x}$ can be treated in similar ways.

Now, let the interval solutions are

$$[\underline{x}_{m1}] = \left[\underline{x}'_1, x_{m1}\right], \qquad [\overline{x}_{m1}] = [x_{m1}, \overline{x}'_1], \tag{21}$$

$$[\underline{x}_{m2}] = \left[\underline{x}'_2, x_{m2}\right], \qquad [\overline{x}_{m2}] = [x_{m2}, \overline{x}'_2].$$

Obviously, if $\underline{x}_{m1}$ and $\underline{x}_{m2}$ be minimal in the intervals $[\underline{x}_{m1}] = [\underline{x}'_1, x_{m1}]$ and $[\underline{x}_{m2}] = \left[\underline{x}'_2, x_{m2}\right]$, respectively, the maximal values of $\overline{x}_{m1}$ and $\overline{x}_{m2}$ are obtained by substituting $\underline{x}_{m1}$and $\underline{x}_{m2}$ in Eq.5.

Substituting $\underline{x}'_1$and $\underline{x}'_2$ in Eq.5, the following equations are achieved.

$$\underline{a}\underline{x}'^2_1 + \underline{b}\underline{x}'^2_1 + \underline{c} - \overline{d}\overline{x}^2 - \overline{e}\overline{x} - \overline{f} + \overline{a}\overline{x}^2 + \overline{b}\overline{x} + \overline{c} - \underline{d}\underline{x}'^2_1 - \underline{e}\underline{x}'_1 - \underline{f} = 0, \tag{22}$$

$$\underline{a}\underline{x}'^2_2 + \underline{b}\underline{x}'^2_2 + \underline{c} - \overline{d}\overline{x}^2 - \overline{e}\overline{x} - \overline{f} + \overline{a}\overline{x}^2 + \overline{b}\overline{x} + \overline{c} - \underline{d}\underline{x}'^2_2 - \underline{e}\underline{x}'_2 - \underline{f} = 0. \tag{23}$$

Suppose that $\overline{x}'_{m1}$ and $\overline{x}''_{m1}$ are the solutions of quadratic equation (22) for $\Delta'_1 > 0$ and the solutions of equation (23) be $\overline{x}'_{m2}, \overline{x}''_{m2}$ for $\Delta'_2 > 0$. Therefore, $\overline{x}^U_{m1.max}$ and $\overline{x}^U_{m2.max}$ are defined as follows

$$\overline{x}^U_{m1.max} = \max\{\overline{x}'_1, \overline{x}'_{m1}, \overline{x}''_{m1}\}, \tag{24}$$

$$\overline{x}^U_{m2.max} = \max\{\overline{x}'_2, \overline{x}'_{m2}, \overline{x}''_{m2}\}.$$

If $\Delta'_1 = \Delta'_2 = 0$ then $\overline{x}'_{m1} = \overline{x}''_{m1}$ and $\overline{x}'_{m2} = \overline{x}''_{m2}$, so

$$\overline{x}^U_{m1.max} = \max\{\overline{x}'_1, \overline{x}'_{m1}\}, \tag{25}$$

$$\overline{x}^U_{m2.max} = \max\{\overline{x}'_2, \overline{x}'_{m2}\}.$$

It is easy to obtain

$$\overline{x}^U_{m1.max} = \overline{x}'_1\ , \quad \overline{x}^U_{m2.max} = \overline{x}'_2, \tag{26}$$

for the case $\Delta'_1 < \Delta'_2 < 0$.

Similarly, we get the minimum of $\underline{x}_{m1}$and $\underline{x}_{m2}$ by substituting of the maximal values of $\overline{x}_{m1}$ and $\overline{x}_{m2}$ in equation (5) as

$$\underline{a}\underline{x}^2 + \underline{b}\underline{x} + \underline{c} - \overline{d}\overline{x}'^2_1 - \overline{e}\overline{x}'_1 - \overline{f} + \overline{a}\overline{x}'^2_1 + \overline{b}\overline{x}'_1 + \overline{c} - \underline{d}\underline{x}^2 - \underline{e}\underline{x} - \underline{f} = 0, \tag{27}$$

$$\underline{a}\underline{x}^2 + \underline{b}\underline{x} + \underline{c} - \overline{d}\overline{x}'^2_2 - \overline{e}\overline{x}'_2 - \overline{f} + \overline{a}\overline{x}'^2_2 + \overline{b}\overline{x}'_2 + \overline{c} - \underline{d}\underline{x}^2 - \underline{e}\underline{x} - \underline{f} = 0. \tag{28}$$

Suppose that for $\Delta''_1 > 0$ and $\Delta''_2 > 0$, the solutions for Eq.27 and Eq.28 are $\underline{x}'_{m1}, \underline{x}''_{m1}$ and $\underline{x}'_{m2}$, $\underline{x}''_{m2}$, respectively. So, $\underline{x}^L_{m1.min}$ and $\underline{x}^L_{m2.min}$ are defined as follows:

$$\underline{x}^L_{m1.min} = \min\{\underline{x}'_1, \underline{x}'_{m1}, \underline{x}''_{m1}\}, \tag{29}$$

$$\underline{x}^L_{m2.min} = \min\{\underline{x}'_2, \underline{x}'_{m2}, \underline{x}''_{m2}\}.$$

If $\Delta''_1 = \Delta''_2 = 0$ then $\underline{x}'_{m1} = \underline{x}''_{m1}$ and $\underline{x}'_{m2} = \underline{x}''_{m2}$ therefore, we have

$$\underline{x}^L_{m1.min} = \min\{\underline{x}'_1, \underline{x}'_{m1}\}, \tag{30}$$

$$\underline{x}^L_{m2.min} = \min\{\underline{x}'_2, \underline{x}'_{m2}\}.$$

Considering $\Delta''_1 < 0,\ \Delta''_2 < 0$, we get

$$\underline{x}^L_{m1.min} = \underline{x}'_1\ , \quad \underline{x}^L_{m2.min} = \underline{x}'_2. \tag{31}$$

Finally, the following interval solutions are obtained.

$$[\underline{x}_{m1}] = [\underline{x}^{L}_{m1.min}, x_{m1}], \qquad [\overline{x}_{m1}] = [x_{m1}, \overline{x}^{U}_{m1.max}], \tag{32}$$
$$[\underline{x}_{m2}] = [\underline{x}^{L}_{m2.min}, x_{m2}], \qquad [\overline{x}_{m2}] = [x_{m2}, \overline{x}^{U}_{m2.max}].$$

Case 2: $\Delta = 0$.

The Eq.6 has the following root

$$x_m = x_{m1} = x_{m2} = \frac{-(\underline{b} - \overline{e} + \overline{b} - \underline{e})}{2(\underline{a} - \overline{d} + \overline{a} - \underline{d})}, \tag{33}$$

Hence, x_m is the upper bound for $\underline{x}_m$ and lower bound for $\overline{x}_m$.

Referring to Eq.11, the delta parameters are calculated for both quadratic equations in Eq.10. Similarly, there are the following three cases.

(I) $\Delta\underline{x} > 0$ and $\Delta\overline{x} > 0$.

Let the roots of two equations in Eq.10 are denoted by $\underline{x}_1, \underline{x}_2$ and $\overline{x}_1, \overline{x}_2$, respectively.

If $\underline{x}_1 < \underline{x}_2 < x_m$ and $x_m < \overline{x}_2 < \overline{x}_1$ then

$$[\underline{x}_m] = [\overline{x}_2, x_m], \qquad [\overline{x}_m] = [x_m, \overline{x}_2], \tag{34}$$

and if $\underline{x}_1 < x_m < \underline{x}_2$ and $\overline{x}_2 < x_m < \overline{x}_1$ then

$$[\underline{x}_m] = [\underline{x}_1, x_m], \qquad [\overline{x}_m] = [x_m, \overline{x}_1] \tag{35}$$

Also, if $x_m < \underline{x}_1 < \underline{x}_2$ and $\overline{x}_2 < \overline{x}_1 < x_m$ then

$$[\underline{x}_m] = [x_m, x_m], \qquad [\overline{x}_m] = [x_m, x_m]. \tag{36}$$

Similarly, the other cases easily can be constructed.

(II) $\Delta\underline{x} = 0$ and $\Delta\overline{x} = 0$.

Let the roots of two quadratic equations in Eq.10 are $\underline{x}_{12} = \underline{x}_1 = \underline{x}_2$ and $\overline{x}_1 = \overline{x}_2 = \overline{x}_{12}$, respectively. Therefore, if $\underline{x}_{12} < x_m < \overline{x}_{12}$ then

$$[\underline{x}_m] = [\underline{x}_{12}, x_m], \qquad [\overline{x}_m] = [x_m, \overline{x}_{12}], \tag{37}$$

and if $x_m < \underline{x}_{12}$ and $x_m < \overline{x}_{12}$, then

$$[\underline{x}_m] = [x_m, x_m], \qquad [\overline{x}_m] = [x_m, \overline{x}_{12}]. \tag{38}$$

Also, if $x_m < \underline{x}_{12}$ and $\overline{x}_{12} < x_m$, then we have

$$[\underline{x}_m] = [\overline{x}_m] = [x_m, x_m]. \tag{39}$$

(III) $\Delta\underline{x} < 0$ and $\Delta\overline{x} < 0$.

The intervals solutions are $[\underline{x}_m] = [\overline{x}_m] = [x_m, x_m]$.

Other cases for $\Delta\underline{x}, \Delta\overline{x}$ are treated similarly.

Now, let the interval solutions are $[\underline{x}_m] = [\underline{x}'_1, x_m]$ and $[\overline{x}_m] = [x_m, \overline{x}'_1]$. Substituting $\underline{x}'^{2}_1$ and $\underline{x}'^{2}_2$ in Eq.5, the two following equations are obtained.

$$\underline{a}\underline{x}'^{2}_1 + \underline{b}\underline{x}'^{2}_1 + \underline{c} - \overline{d}\overline{x}^2 - \overline{e}\overline{x} - \overline{f} + \overline{a}\overline{x}^2 + \overline{b}\overline{x} + \overline{c} - \underline{d}\underline{x}'^{2}_1 - \underline{e}\underline{x}'_1 - \underline{f} = 0, \tag{40}$$
$$\underline{a}\underline{x}'^{2}_2 + \underline{b}\underline{x}'^{2}_2 + \underline{c} - \overline{d}\overline{x}^2 - \overline{e}\overline{x} - \overline{f} + \overline{a}\overline{x}^2 + \overline{b}\overline{x} + \overline{c} - \underline{d}\underline{x}'^{2}_2 - \underline{e}\underline{x}'_2 - \underline{f} = 0. \tag{41}$$

If $\Delta'_1 > 0$ and $\Delta'_2 > 0$, let $\overline{x}'_m$ and $\overline{x}''_m$ the roots of Eq.40 and $\underline{x}'_m$, $\underline{x}''_m$ the roots of Eq.41. Thus,

$$\overline{x}^{U}_{m.max} = \max\{\overline{x}'_1, \overline{x}'_m, \overline{x}''_m\}, \tag{42}$$
$$\underline{x}^{L}_{m.min} = \min\{\underline{x}'_1, \underline{x}'_m, \underline{x}''_m\}.$$

If $\Delta'_1 = \Delta'_2 = 0$ then $\overline{x}'_m = \overline{x}''_m$ and $\underline{x}'_m = \underline{x}''_m$ therefore,

$$\overline{x}^{U}_{m.max} = \max\{\overline{x}'_1, \overline{x}'_m = \overline{x}''_m\}, \tag{43}$$
$$\underline{x}^{L}_{m.min} = \min\{\underline{x}'_1, \underline{x}'_m = \underline{x}''_m\}.$$

At last if $\Delta'_1 < 0$ and $\Delta'_2 < 0$, then

$$\overline{x}^{U}_{m.max} = \overline{x}'_1, \qquad \underline{x}^{L}_{m.min} = \underline{x}'_1. \tag{44}$$

Finally, we get the following interval solutions as

$$[\underline{x}_m] = [\underline{x}^L_{m.min}, x_m], \qquad [\overline{x}_m] = [x_m, \overline{x}^U_{m.max}]. \qquad (45)$$

Case 3: $\Delta < 0$.
There are no interval solutions.

4. Numerical Examples

In this section, three examples with different uncertain parameters are provided to illustrate the simplicity and applicability of the presented method.

Example 1. Consider the following quadratic algebraic equation with interval parameters

$$ax^2 + bx + c = dx^2 + ex + f,$$

where, $a = [3,4], b = [1,2], c = [3,4], d = [1,2], e = [6,7], f = [1,2].$
To solve this problem, consider

$$(\underline{a} - \overline{d} + \overline{a} - \underline{d})x_m^2 + (\underline{b} - \overline{e} + \overline{b} - \underline{e})x_m + (\underline{c} - \overline{f} + \overline{c} - \underline{f}) = 0.$$

According to the assumptions, we get

$$4x_m^2 - 10x_m + 4 = 0.$$

Thus, the solutions are

$$x_{m1} = \frac{1}{2}, \quad x_{m2} = 2.$$

The delta parameters for both equations of Eq.10 are calculated as

$$\Delta\underline{x} = 32, \qquad \Delta\overline{x} = -20 < 0,$$

and

$$\underline{x}_1 = 0.2\,, \quad \underline{x}_2 = 5.8\,.$$

So, we get

$$[\underline{x}_{m1}] = [0.2,0.5], \quad [\overline{x}_{m1}] = [0.5,0.5],$$
$$[\underline{x}_{m2}] = [1.25,2], \quad [\overline{x}_{m2}] = [2,2].$$

Substituting $\underline{x}'_1 = 0.2$ and $\underline{x}'_2 = 1.25$ in Eq.22 and Eq.23, respectively, the following results are obtained.

$$\Delta'_1 = 0.36, \quad \overline{x}'_{m1}, \overline{x}''_{m1} = 1.1,1.4, \quad \overline{x}^U_{m1.max} = \max\{0.5,1.1,1.4\} = 1.4,$$
$$\Delta'_2 = 18, \quad \overline{x}'_{m2}, \overline{x}''_{m2} = 0.2,2.3, \quad \overline{x}^U_{m2.max} = \max\{2,0.2,2.3\} = 2.3,$$

and by substituting the lower bounds of $\overline{x}_{m1}$ and $\overline{x}_{m2}$, that is, 0.5 and 2 in Eq.27 and Eq.28, respectively, we achieve

$$\Delta''_1 = 9, \quad \underline{x}'_{m1} = 0.5\,, \underline{x}''_{m1} = 2\,, \underline{x}^L_{m1.min} = \min\{0.2,2,0.5\} = 0.2\,,$$
$$\Delta''_2 = 9, \quad \underline{x}'_{m2} = 0.5\,, \underline{x}''_{m2} = 2\,, \underline{x}^L_{m2.min} = \min\{1.25,2,0.5\} = 0.5.$$

Therefore, the interval solution are as follows.

$$[\underline{x}_{m1}] = [0.2,0.5], \quad [\overline{x}_{m1}] = [0.5,1.4],$$
$$[\underline{x}_{m2}] = [0.5,2], \quad [\overline{x}_{m2}] = [2,2.3].$$

Example 2. Let $a = [0.1,3], b = [1,9], c = [3,8], d = [2,5], e = [1,5], f = [1,7]$, for the following quadratic algebraic equation with interval parameters

$$ax^2 + bx + c = dx^2 + ex + f.$$

Considering the quadratic algebraic equation

$$-3.9x_m^2 + 4x_m + 3 = 0.$$

Delta parameter and the roots are calculated as

$$\Delta = 62.8\,, \qquad x_{m1} = -0.50316\,, \qquad x_{m2} = 1.528801,$$

and

$$\Delta\underline{x} = -62.4 < 0\,, \quad \Delta\overline{x} = 36 > 0\,, \quad \overline{x}_1 = -7\,, \quad \overline{x}_2 = -1.$$

Furthermore

$$[\underline{x}_{m1}] = [-0.50316,0.50316], \quad [\overline{x}_{m1}] = [-0.50316,-0.50316],$$
$$[\underline{x}_{m2}] = [1.528801,1.528801], \quad [\overline{x}_{m2}] = [1.528801,1.528801].$$

In the other side,

$$\Delta'_1 = 36.151816\,, \qquad \overline{x}'_{m1} = -0.50316\,, \qquad \overline{x}''_{m1} = 2.50316.$$

So,

$$\overline{x}^U_{m1.max} = \max\{-0.50316, 2.50316, -0.50316\} = 2.50316\,,$$

and

$$\Delta''_1 = 4.474064\,, \quad \overline{x}'_{m2} = 0.4712\,, \quad \overline{x}''_{m2} = 1.528799,$$
$$\overline{x}^U_{m2.max} = \max\{1.528801, 1.528799.0.4712\} = 1.528801.$$

Calculating $\overline{x}'_{m1}$, $\overline{x}''_{m1}$, $\overline{x}'_{m2}$ and $\overline{x}''_{m2}$, we find

$$\underline{x}^L_{m1.min} = \min\{-0.50316, 0.50316, -0.50316\} = -0.50316\,,$$
$$\underline{x}^L_{m2.min} = \min\{1.528801, 1.528801, -1.528801\} = -1.528801.$$

Therefore,

$$[\underline{x}_{m1}] = [-0.50316, 0.50316], \qquad [\overline{x}_{m1}] = [-0.50316, -2.50316],$$
$$[\underline{x}_{m2}] = [-1.528801, 1.528801], \qquad [\overline{x}_{m2}] = [1.528801, 1.528801].$$

Example 3. Let $a = [3,4], b = [1,2], c = [1,2], d = [1,2], e = [4,5], f = [3,4]$. Find the interval solutions for the following quadratic algebraic equation

$$ax^2 + bx + c = dx^2 + ex + f.$$

The quadratic algebraic equation related to the given values are achieved as

$$4x_m^2 - 6x_m - 4 = 0.$$

Considering the process in section 3, the following results are obtained.

$$x_{m1} = -0.5\,, \quad x_{m2} = 2\,, \quad \Delta\underline{x} = 28\,, \quad \Delta\overline{x} = 16,$$
$$\underline{x}_1 = -0.64\,, \quad \underline{x}_2 = 4.64\,, \quad \overline{x}_1 = 0\,, \quad \overline{x}_2 = \frac{4}{3},$$

and

$$[\underline{x}_{m1}] = [-0.64, -0.5]\,, \quad [\overline{x}_{m1}] = [-0.5, 0],$$
$$[\underline{x}_{m2}] = [0.75, 2]\,, \quad [\overline{x}_{m2}] = [2, 2].$$

Following the mentioned process, we get

$$\overline{x}^U_{m1.max} = \overline{x}_1 = 0\,, \quad \overline{x}^U_{m2.max} = \max\{2, -1, 2.5\} = 2.5.$$

Similarly

$$\underline{x}^L_{m1.min} = \min\{-0.64, -0.85, 2.35\} = -0.85,$$
$$\underline{x}^L_{m2.min} = \min\{0.75, -0.5, 2\} = -0.5.$$

Therefore, the interval solutions are obtained as follows.

$$[\underline{x}_{m1}] = [-0.85, -0.5]\,, \quad [\overline{x}_{m1}] = [-0.5, 0],$$
$$[\underline{x}_{m2}] = [0.5, 2]\,, \quad [\overline{x}_{m2}] = [2, 2.5].$$

5. Conclusion

The objective of the paper is to present a new concept to the solution of interval and fuzzy quadratic equations of dual form based upon the generalized technique of interval and fuzzy extension called "interval extended zero" method. The key idea is the dealing of "interval zero" as a symmetrical interval around zero. It is presented that the idea of such approach is a direct consequence of interval subtraction operation. The method makes it easy to solve some formerly unresolved methodological problems in applied interval analysis and fuzzy arithmetic. An important for practice advantage of the idea of this method is that it provides substantially narrower solutions than conventional methods. The effectiveness and applicability of the derived interval method was demonstrated by three numerical examples.

References

Abbasbandy, S. & Ezzati, R. (2006). Newton's method for solving a system of fuzzy nonlinear equations. *Appl. Math. Comput., 175*(2), 1189-1199.

Abbasbandy, S. & Otadi, M. (2006). Numerical solution of fuzzy polynomials by fuzzy neural network. *Appl. Math. Comput., 181*(2), 1084-1089.

Alefeld, G. & Herzberger, J. (1983). *Introduction to Interval Computations*. New York, USA: Academic Press.

Allahviranloo, T. & Moazam, L.G. (2014). The solution of fuzzy quadratic equation based on optimization theory. *Sci. World J.*, *2014*(Special Issue), 1–6. Retrieved from https://www.hindawi.com/journals/tswj/2014/156203/.
Allahviranloo, T., Otadi, M. & Mosleh, M. (2007). Iterative method for fuzzy equations. *Soft Comput., 12*(10), 935-939.
Buckley, J.J. (1992). Solving fuzzy equations in economics and finance. *Fuzzy Sets and Systems, 48*(3), 289-296.
Buckley, J.J. (1987). The fuzzy mathematics of finance. *Fuzzy Sets and Systems, 21*(3), 257-273.
Calzi, M. Li. (1990). Towards a general setting for the fuzzy mathematics of finance. *Fuzzy Sets and Systems, 35*(3), 265-280.
Chalco-Cano, Y., Román-Flores, H., Rojas-Medar, M., Saavedra, O.R. & Jiménez-Gamero, M.D. (2007). The extension principle and a decomposition of fuzzy sets. *Information Sciences, 177*(23), 5394-5403.
Chen, S.H. & Yang, X.W. (2000). Interval finite element method for beam structures. *Finite Elements in Analysis and Design, 34*(1), 75-88.
Dehghan, M., Hashemi, B. &. Ghatee, M. (2007). Solution of the fully fuzzy linear systems using iterative techniques. *Chaos Solitons and Fractals, 34*(2), 316-336.
Dubois, D. & Prade, H. (1978). Operations on fuzzy numbers. *J. Systems Sci., 9*(6), 613-626.
Dutta, P. Boruah, H. & Ali, T. (2011). Fuzzy arithmetic with and without using α-cut method: a comparative study. *International Journal of Latest Trends in Computing*, *2*(1), 99-107.
Dymova, L. (2010). Fuzzy solution of interval nonlinear equations. *Lecture Notes in Computer Science*, 6068 LNCS, 418-426. doi: 10.1007/978-3-642-14403-5_44.
Dymova, L. & Sevastjanov, P. (2018). A New Method for Solving Nonlinear Interval and Fuzzy Equations. In: Wyrzykowski R., Dongarra J., Deelman E., Karczewski K. (eds) Parallel Processing and Applied Mathematics. PPAM 2017, Lecture Notes in Computer Science, 10778, Springer, Cham. doi: 10.1007/978-3-319-78054-2_35.
Ferreira, J.A., Patricio, F. & Oliveira, F. (2005). On the computation of solutions of systems of interval polynomial equations. *Journal of Computational and Applied Mathematics, 173*(2), 295-302.
Hanss, M. (2005). *Applied Fuzzy Arithmetic*. Berlin, Germany: Springer.
Kaufmann, A. & Gupta, M.M. (1985). *Introduction Fuzzy Arithmetic*. New York, USA: Van Nostrand Reinhold.
Lai, Y.J. & Hwang, C.L. (1992). *Fuzzy Mathematical programming theory and applications*. Berlin, Germany: Springer.
Moazam, L.G. (2016). The solution of fuzzy quadratic equations based on restricted variation. *Int. J. Ind. Math*., *8*(4), 395-400.
Mosleh, M. & Otadi, M. (2010). A New Approach to the Numerical Solution of Dual Fully Fuzzy Polynomial Equations. *Int. J. Industrial Mathematics, 2*(2), 129-142.
Mosleh, M., Otadi, M. & Vafaee Varmazabadi, Sh. (2008). General Dual Fuzzy Linear Systems. *Int. J. Contemp. Math. Sciences, 3*(28), 1385-1394.
Movahedian, M., Salahshour, S., Haji Ghasemi, S., Khezerloo, S., Khezerloo, M. & Khorasany, S.M. (2009). Duality in linear interval equations. *Int. J. Industrial Mathematics, 1*(1), 41-45.
Muzzioli, S. & Reynaerts, H. (2006). Fuzzy linear systems of the form $A_1x+b_1 = A_2x+b_2$. *Fuzzy Sets and Systems, 157*(7), 939-951.
Landowski, M. (2017), *RDM interval method for solving quadratic interval equation. Przegląd Elektrotechniczny, 93*(1), 65-68.
Sevastjanov, P. & Dymova, L. (2007). Fuzzy solution of interval linear equation. *International conference on parallel processing and applied mathematics*. Springer. Berlin, Heidelberg. pp. 1392-1399. doi: *10.1007/978-3-540-68111-3_147*.
Sevastjanov, P. & Dymova, L. (2009). A new method for solving interval and fuzzy equations: linear case. *Information sciences, 179*(7), 925-937.
Shieh, B.-S. (2008). Infinite fuzzy relation equations with continuous t-norms. *Information Sciences, 178*(8), 1961-1967.
Wu, C.C. & Chang, N.B. (2003). Grey input-output analysis and its application for environmental cost allocation. *European Journal of Operational Research, 145*(1), 175-201.
Zadeh, L.A. (1965). Fuzzy sets. *Information and Control, 8*(3), 338-353.
Zadeh, L.A. (1975). The concept of a linguistic variable and its application to approximate reasoning. *Information Sciences, 8*(3), 199-249.

Research Article

Performance Evaluation of WDM Optical Fiber Communication System in the Presence of PMD

Nawroz I. Hamadamen

Department of Software and Informatics Engineering, College of Engineering, Salahaddin University – Erbil, Erbil, KRI, Iraq

E-mail: nawroz.hamadamen@su.edu.krd

Access this article online		
Received on: March 10, 2021	**Accepted on:** December 12, 2021	**Published on:** December 31, 2021
DOI: 10.25079/ukhjse.v5n2y2021.pp90-103	**E-ISSN:** 2520-7792	

Abstract

This paper investigates for rising optical fiber transmission strength, increasing bandwidth, and decreasing communication system weakness by using wavelength division multiplexing (WDM). WDM gives today's distention speed and communication traffic. Systems using WDM faces nonlinearities, which the most intensive nonlinear attack is, four wave mixing (FWM). FWM creates and increases crosstalk between WDM channels as a result slows down and impairs the performance of the communication system. This investigation uses orthogonal frequency division multiplexing (OFDM) for evaluating execution of WDM fiber system by repairing Polarization Mode Dispersion (PMD). We took results in the case of trying PMD-Emulator and without trying PMD-Emulator in the system design. We compared the results got in both cases. Furthermore, we compared the performance of the system with the investigations done using different ways, methods, and techniques for compensating PMD and FWM appears in WDM systems. As PMD-Emulator, helps enhancing the system design performance, and OFDM gives the feature of robustness and useful execution to the system. OFDM examined by appointing interfered orthogonal signal sets, for 16 channels; with equally spaced OFDM channels. Oure results showed that the optical fiber communication system using OFDM technique gives perfect removing FWM signal crosstalk, and accurate data transmission, comparing to other techniques used in other researches. We got a decreased FWM power to -77dBm, and the BER of -0.317. Furthermore, the system quality increased with applying PMD-Emulator and OFDM. In addition, using PMD-Emulator in the system design raised the results effectiveness. The program used in the present work is optisystem-15, and the results obtained in this study coincide with the theoretical and actual results obtained by the previous studies.

Keywords: WDM Improvement, PMD, OFDM, Nonlinearity, FWM.

1. Introduction

In systems operate on the bases of wavelength division multiplexing (WDM), nonlinear effects grown in significance, particularly at moderate powers and bitrates. In the WDM systems, at new frequencies FWM provide rise of new signals. These signals appear as crosstalk to the existing signals in the system (Alberto *et al.*, 2019), and (Petr *et al*, 2020). The effect of FWM is a great aspect for the future optical networks to consider (Alifdal *et al.*, 2017). As it decreases the performance of (WDM) optical networks, which damages the channel energy and the output signal (Petr *et al*, 2020). Moreover, to meet nowadays expansion demand for bandwidth, studying for overcoming ways of these transmission capacity limitations is continuous by the researchers (Salim, 2019). Furthermore, WDM is one of the solutions for expanding each fiber capacity to match the needing of enhanced mobile broadband (eMBB) within 5G network system

(Xiang Liu, 2019). In this paper, we connect an optical fiber communication system with (10 Gb/s) and modulating (16) channels using OFDM to evaluate the appearance of FWM, and (PMD) compensation in WDM systems.
In the latest years many researchers searched, studied, and published papers about this important issue. Researches are in different directions on it. Some of them are as following. In 2017 another group, worked on conservation matter set on controlling procedure of (FWM) make use of optical phase conjugation (OPC) elements, and using arrangements of OPCs that were non-identical in ultra-dense wavelength division multiplexing (WDM) system with coherent orthogonal frequency division multiplexing (OFDM) incorporation (Chawhan *et al.*, 2018). In 2018 researchers worked on the performance of (OCDMA/WDM), Simulation results showed bit-error-rate (BER)$\leq 10^{-9}$ for up to 25 Km distance at the bitrate of 1Gb/s optical communication networks (Ahmed *et al.*, 2018).. In 2019 investigation has been done on four-wave mixing noises suppression in QAM Coherent OFDM System They worked in polarization domain and showed improving the nonlinear tolerance of such system (Jianxin *et al,* 2019). They used the plan of phase-conjugated twin waves (PCTW) for decreasing the effect of FWM noise. In 2020 a group of researchers studied for upgrading FWM order in two-directed ultra DWDM-PON networking. They evenly located source of light and operated PMD emulator (Manzoor *et al,* 2020). In 2021 Fazal and his workmate worked for mitigation of FWM by operating DSP receiver. They could compensate FWM effect to attain a BER under 10^{-6} for reaching an optical fiber propagation far to 500 Km. (Fazal *et al*, 2021). Moreover, it will be continuous as overtime work on the internet, its various uses for fast, accurate, and pure communications needed and with a high possibility, the need increased.

2. Fiber Nonlinearity

The transmitted spectrum in optical WDM is linear as long as the fiber power is not large. Utilizing high input optical power in long haul connection for reducing the repeater numbers is some other great nonlinearity reference. These give rise to high production impairments. The basic nonlinear impairments in WDM fiber communication systems known as Kerr effects, which are self-phase modulation (SPM), cross phase modulation (XPM), and four wave mixing (FWM). Need to be reduced (Muhammad Irfan *et al,* 2020). SPM brings out new wavelength by widening the optical spectrum. It can be controlled by many techniques for restoring optical information such as operate spectral reparation filtering (Chung *et al,* 2018). Conversion of an optical pulse by another optical pulse expects to cross-phase modulation (XPM), that all the optical signal phases affected by one signal; and vice-versa (Alifdal *et al.*, 2017).
In fact FWM is interference just like ISI. Reaction of three wavelengths give rise to fourth wavelength. It causes phase shift in a WDM channel and lead for creation of new frequencies as shown in Fig 1 (Fazal *et al*, 2021).
The obstacle that is most worthy among the nonlinear type's wares by bringing down the execution of WDM optical networks. Creates possible distortion of the signal output and disperse channel energy is FWM. Which is the most powerful damage influence. When the index of refraction inside the fiber changes with the power level, the FWM turns up (Fazal *et al*, 2021).
In WDM, the occurrence of FWM counts on some factors. Among them; the power per channel, the channel spacing wavelength, the interact distance of transmission, effective area, and the optical fiber run features (Fazal *et al*, 2021). In FWM due to channel interference a heavy crosstalk is generated in the network (Alifdal *et al.*, 2017).

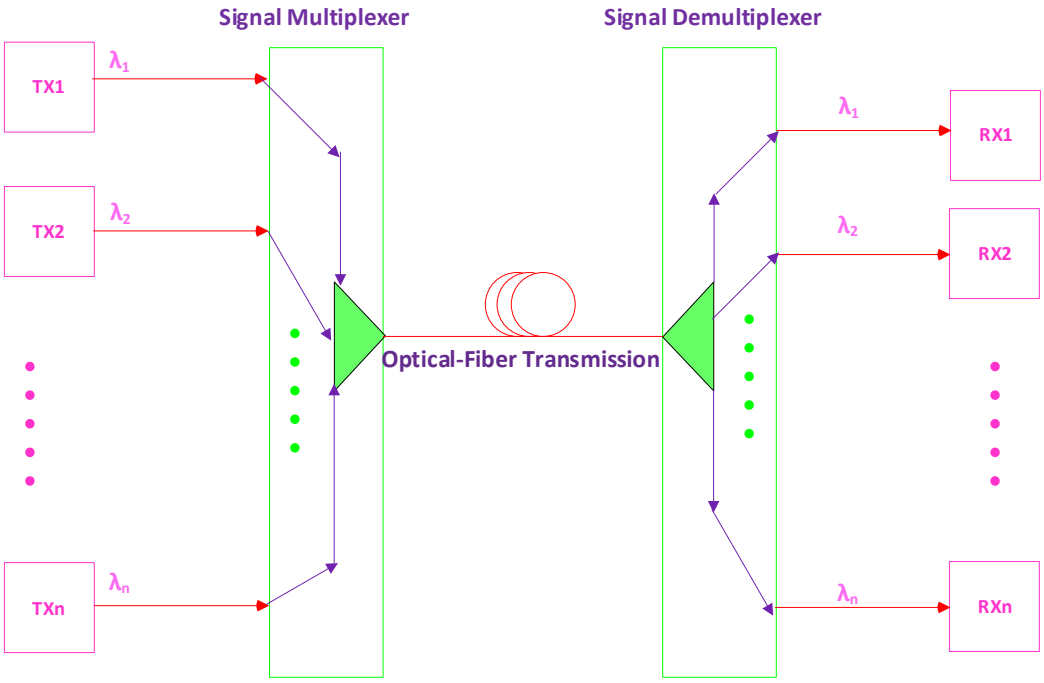

Figure 1. (WDM) Process Diagram.

If we have three waves with frequencies f_i, f_j, and f_k, over an optical fiber cooperating. They produce nonlinearity by interacting with each other and getting out nine new waves at frequencies of equation 1, and Fig 2 (Manzoor *et al,* 2020):

$$f_{ijk} = f_i \pm f_j \pm f_k \qquad (1)$$

The number of new waves produced by the FWM symbolled as M. In general shown in the formula of equation (2) for N number of input wavelengths: (Alifdal *et al.*, 2017), and (Manzoor *et al,* 2020):

$$M = \frac{N^2(N-1)}{2} \qquad (2)$$

Where: N = number of channels multiplexed.

At frequency fijk the power of the new produced optical wave is (Alifdal *et al.*, 2017):

$$P_{ijk} = \eta \frac{1024\pi^6}{\eta^4 \lambda^2 c^2} \left(\frac{DX_{1111} L_{eff}}{A_{eff}}\right)^2 P_i P_j P_k e^{-\alpha L} \qquad (3)$$

Where:

Pi, pj, pk = Insert powers, α = loss coefficient of Fiber, n = index of refraction of Core, X_{1111} = Nonlinear susceptibility (third order), λ = inner wavelength, c = Vacuum velocity of Light (= 3×108 m/s), L_{eff} = Fiber effective length. It given by

$$L_{eff} = \frac{(1-e^{-\alpha L})}{\alpha} \qquad (4)$$

A_{eff} = effective area of Core, D = decadence factor (D = 3 for i = j, D = 6 for i ≠j

FWM efficiency, it is given by (η).

$$\eta = \frac{\alpha^2}{\alpha^2+\Delta\beta^2}\left[1+\frac{4e^{-\alpha L}sin^2(\Delta\beta L/2)}{\left[1-e^{-\alpha L}\right]^2}\right] \qquad (5)$$

This efficiency depends on the channel spacing through the phase mismatch (Alifdal *et al.*, 2017):

$$\Delta\beta = \frac{2\pi\lambda^2}{c}|f_i - f_k|\left[D_c + \frac{dD}{d\lambda}\left(\frac{\lambda^2}{2c}\right)\left(|f_i - f_k| + |f_j - f_k|\right)\right] \qquad (6)$$

Dc is the chromatic dispersion coefficient and $\frac{dD}{d\lambda}$ is its slop.

For N number of WDM system channels, the total power produced in the result of FWM at the frequency fm expressed as (Alifdal *et al.*, 2017):

$$P_{tot}(f_m) = \sum f_k = f_i + f_j - f_m \sum f_j \sum f_i P_{ijk} \qquad (7)$$

The schematic of Figure-2 illustrates the FWM frequencies, the subscripts i, j, and k pick out 1, 2, and 3. It clears three various signal frequencies f1, f2, and f3, and nine new frequencies fijk.

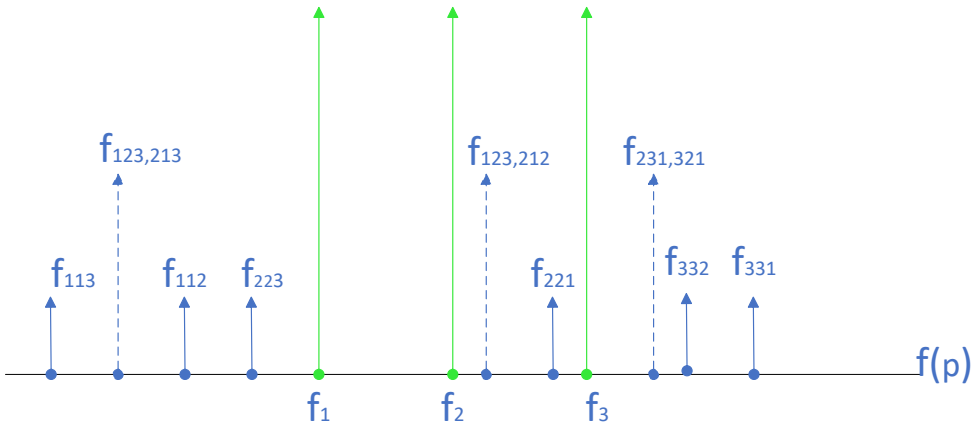

Figure 2. Sketch of the three input waves and the nine unwanted created waves in FWM sum.

3. PMD Theory

Fiber index of refraction determines the speed of propagated optical pulses in an optical fiber for X and Y polarized light; the refractive indices are symbolized as n_x and n_y respectively. For graphically explaining light refractive indices, with a particular polarization it is familiar to draw an index of refraction ellipse. The ellipse index of refraction becomes a circle with a fiber of completely symmetric index of refraction outline, as shown in Fig 3,

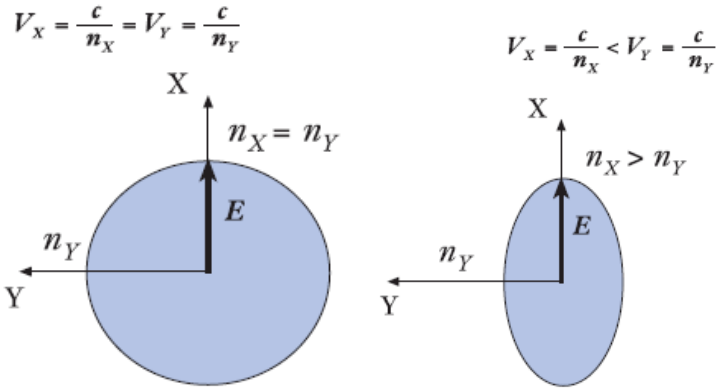

(a) Completely symmetrical fiber description when the speed of light does not depend on its polarization.

(b) Description of fiber birefringence because Y-polarized light propagates faster than X-polarized lig

Figure 3. (Dubovan *et al,* 2020).

The two orthogonally polarized modes go along the fiber in unlike group velocities. Consequently time propagation delay occurring between them, that affects the optical fibers' polarization features.

The appearance of the time delay showed differential group delay (DGD) and its symbol $\Delta\tau$ equation 8, and Fig 4. (Jozef Dubovan *et al,* 2020).

$$\Delta\tau = D_{PMD}\sqrt{L} \quad (8)$$

$$\Delta\tau = D_{PMD}\sqrt{L} < 0.1T \quad (9)$$

The standard pulse

Two orthogonal polarization modes

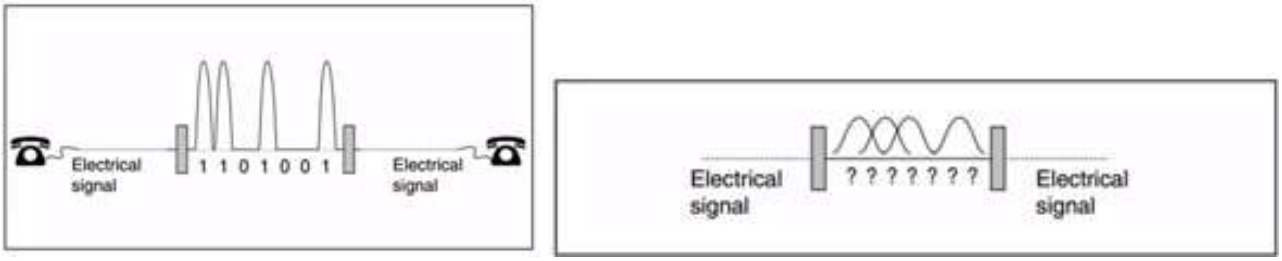

Pulses in 10 Gb/s are closer PMD-affected pulses in a 10 Gb/s system overlap

Figure 4. The transmitted pulses status PMD and DGD

4. OFDM THEORY

Next generation optical fiber networks call for switching strength, spectral efficiency, segmentation, and wanted capacity; to generate these a powerful modulation format is needed. Since large bitrates along optical transmission link is requested (Arpan Garg, and Nitin Mittal, 2020). OFDM is one of the newest versions of telecommunication and wireless communication system modulation technique (David *et al,* 2020). It has been quite suggested for presenting this strong modulation shape, as it uses digital signal processing (DSP) technique efficiently.

OFDM modulates many carriers with individual modulated subcarriers. The orthogonality structure of the carriers decrease crosstalk, interference, and channel scattering (Arpan *et al,* 2020). Many wireless employments use OFDM, such as, 3G, 4G, WLAN standards, and Digital Video Broadcasting (DVB). It characterized as flexibility and large spectral efficiency (Davinder *et al,* 2019). OFDM system is cleared in the block diagram of Fig -5. The OFDM signal represented as eq. 10 (David *et al,* 2020):

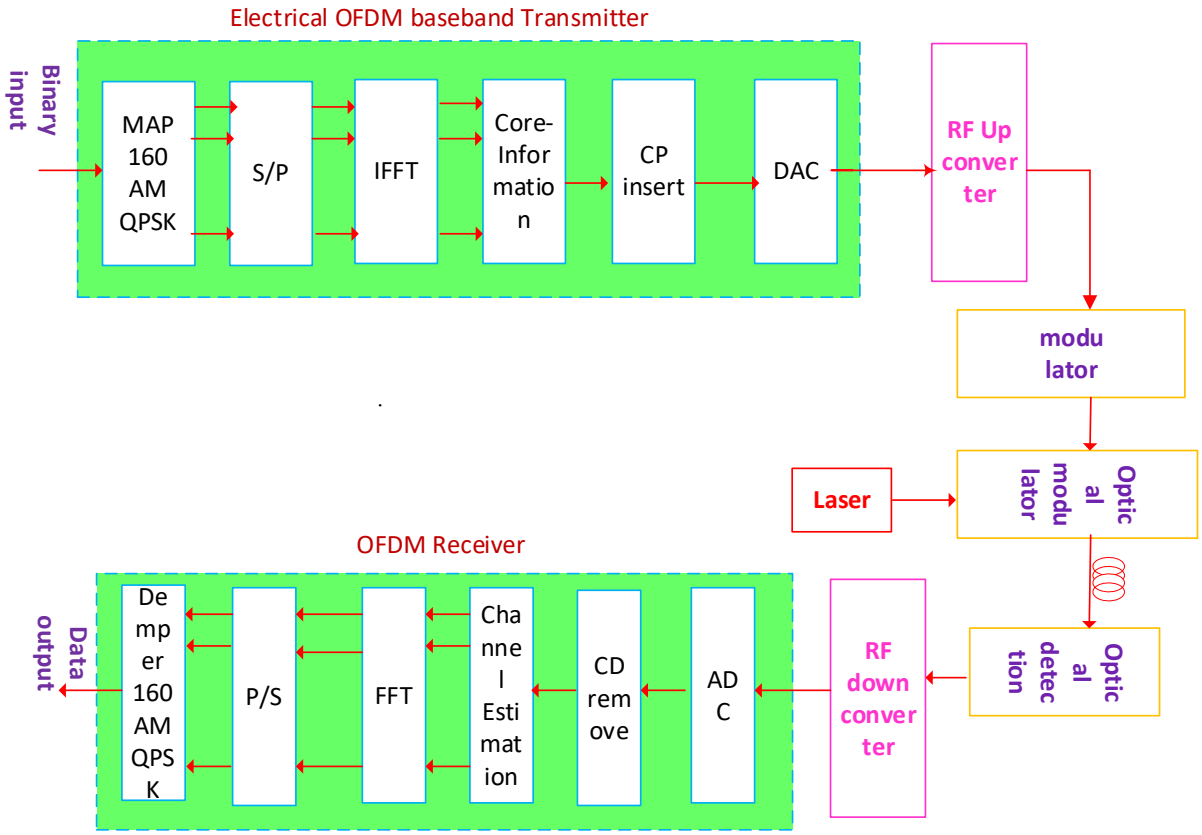

Figure 5. Proposed Structure diagram of OFDM system

$$g(t) = \sum_{\eta=-\infty}^{\infty} a_n(t)\cos\left(2\pi nt/T\right) - b_n(t)\sin\left(2\pi nt/T\right) \quad (10)$$

The orthogonality represented as eq. 11 when, moves to zero on a certain time (Arpan *et al,* 2020):

$$\frac{2}{T}\int_t^{t-T}\cos\left(2\pi nt/T\right)\times\cos\left(2\pi mt/T\right)dt = \begin{cases}0\ (n\neq m)\\1\ (n=m)\end{cases} \quad (11)$$

$$\frac{2}{T}\int_t^{t-T}\sin\left(2\pi nt/T\right)\times\sin\left(2\pi mt/T\right)dt = \begin{cases}0\ (n\neq m)\\1\ (n=m)\end{cases} \quad (12)$$

Demodulation:

$$a_n(t_o) = \frac{2}{T}\int_t^{t-T} g(t)\cos\left(2\pi nt/T\right)dt \quad (13)$$

$$b_n(t_o) = \frac{2}{T}\int_t^{t-T} g(t)sin\left(2\pi nt/T\right)dt \quad (14)$$

Where $T = \frac{1}{Nf_s}$ the symbol period fs is Nyquist filter of frequency.

g(t) is analog signal and is taken from gn insertion (Arpan *et al,* 2020).

$$g(t) = \sum_n g(nT)\emptyset_n(t) \quad (15)$$

$\Phi_n(t)$ are time interleaved optical Nyquist pulses and is given by:

$$\emptyset_n(t) = r(t-nT) \quad (16)$$

Any OFDM subcarrier has a sinc, $\left(\frac{\sin x}{x}\right)$ spectrum in the frequency domain as shown in Fig-6.

The measurement of spectral efficiency is Bps/Hz such as $C = B\times\log\left(1+\frac{S}{N}\right)$. Comprise to noise extra data is transmitted (Davinder *et al,* 2019).

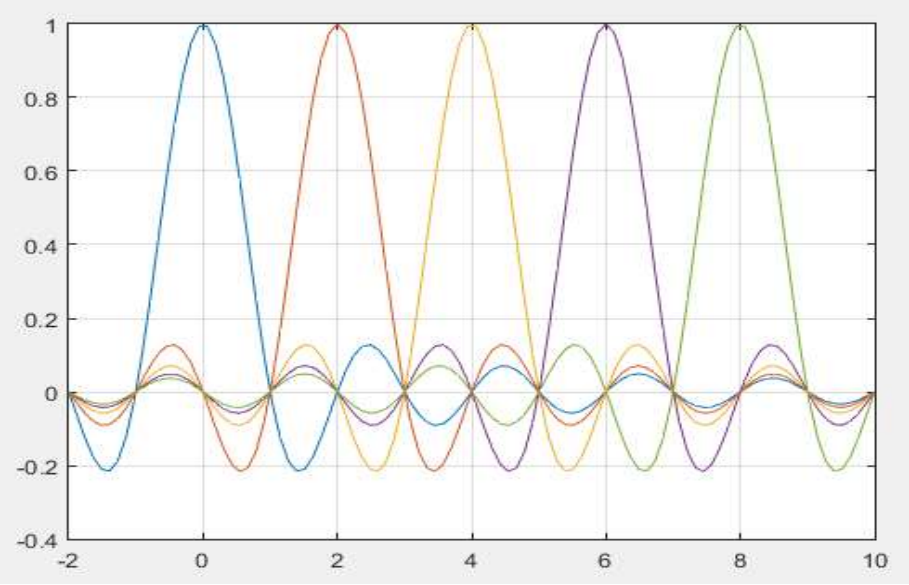

Figure 6. Orthogonal OFDM spectrum

5. Modelling System Analysis

Through certain length of fiber link having SMF 5 Km for 1 Km DCF which has a given PMD, polarization dependent loss (PDL), and chromatic dispersion (CD), a system of (N = 16) channels of OFDM signals as shown in Figure-7 is designed. Starting from frequency of first channel 193.1 THz to the frequency 194.6 THz of the 16th channel has transmitted. In the experimental setup, considering a model of receiver has OFDM/ Demodulator that consists of LP Cosine Roll off Filters, with two Mach-Zehnder Modulators. The signal output from the receiver OFDM model go through QAM Sequence Decoder, NRZ Pulse Generator, and 3R Regenerator. Optisystem-15 has used for the simulation and the parameters given in the data table-1where applied for the simulation.

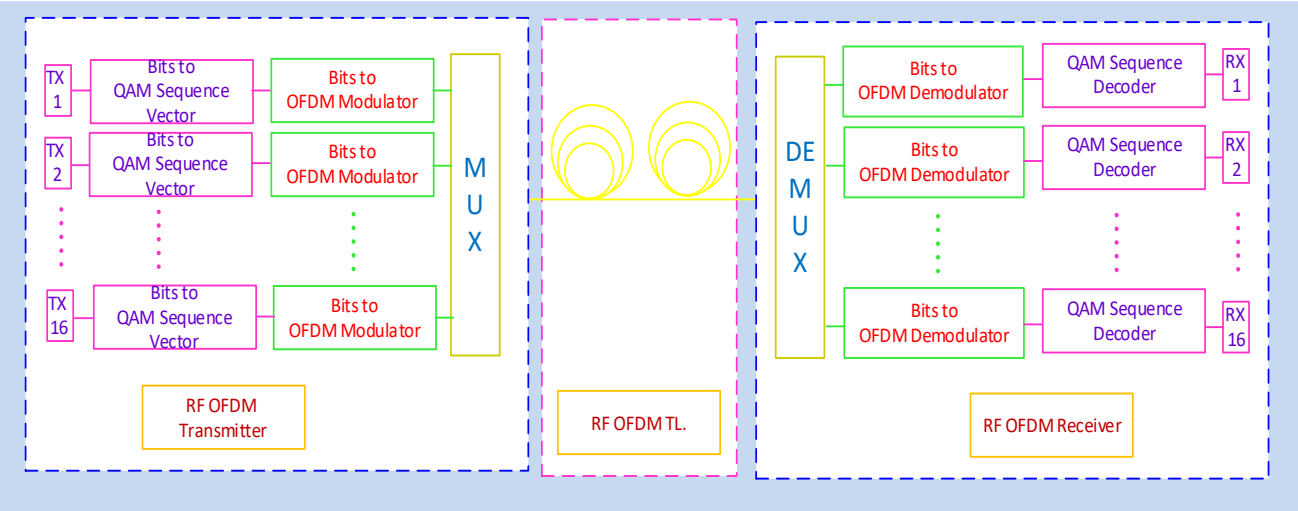

Figure 7. Analytical Model of OFDM System

Table 1: Parameters used in the current simulated system

Parameter	Quantity or Rank
Modulation	16 QAM
Bit rate	10 Gb/s
Channels Frequency	193.1 THz to 194.6 THz
Input Laser Power	-7 to 7
Symbol rate	2.5 G Symbol/s
Output Signal Type	Parameterized
OSA Filter Type	Rectangle
OSA Band Width	0.001 nm Unwrapped Phase
OFDM number of Subcarriers	512
Number of FFT Points	1024
Number of Prefix Points	0
EDFA and FWM	Included
Line SMF	5 Km
DCF	1 Km

6. Simulation Results and Discussion

In the system bandwidth, FWM created product terms locates at the frequencies of the channel.
Because this simulation setup uses OFDM Modulation, while the information signal extend it's top; the maximum point, their adjacent are at zero point (or null) which points orthogonality, in this way OFDM suppress interference while several signals interweaving, based on this orthogonal feature the de-multiplexer at the receiver end would separate the channels. As orthogonal means, signals multiplexed in a way that the peak of one signal take place at the null of the other nearby signals. In this search, results have shown that the effect of FWM decreases using OFDM technology for the communication system transmission. The spectrum results shown in figures- 7 and 8 before trying PMD Emulator and after using a PMD Emulator respectively in the circuit design having standards of 50 Km long, dispersion of 1.3

ps/GHz and of 0.2 dB/Km attenuation with dispersion slop 0.075 ps/nm/Km, to reform products of FWM. It was clear in the result figures that the efficiency of FWM enhanced from -67 dBm to -77 dBm after trying PMD Emulator; it is the effect of using PMD Emulator in the system design, in other side there was another reduction of FWM, and this one due to applying OFDM modulation. It can be noticed from the data results in table-2 which shows a huge power reduction of FWM comparing to the investigation done in 2019 Publication Journal mentioned in references by Habib Ullah and the rest researchers worked with in 'mitigation of FWM operating non-identical techniques of modulation and optical filters in dense WDM (DWDM) fiber optic communication systems. The analysis modified. Which they got reduction FWM power from -36 to -61 dBm by using modified duo-binary modulation against normal system.

The results shown by this investigation, upgraded better as compared to the investigation done in 2020, publication shown in references Habib Ullah Manzoor, Muhammad Zafar, Woo Young Kim and the rest friends, performed 'boosting regulation of FWM in two-way radical passive optical networking; DWDM-PON. Self-controlled light source make use of PMD-Emulator'. As they showed their work results improving FWM from -68 dBm to -73 dBm after putting in PMD emulator and after optical amplifier.

Figures- 10 and 11 show the BER when the power approaches to zero. We can notice from the two results that when the system works without PMD, BER is -0.31563 this value decreases to -0.317 after trying PMD and this characterizes better performance of the communication system design using PMD Emulator. We can see the overall enhancement of the system in figure- 14 the BER Analyzer after trying PMD emulator.

Table-2 gives signal quality data too, at 0.62 s bit period the receiver signal quality is 0.03944 this amount increases to 0.03979 at the same bit period after trying PMD, which tells us that the impairment is quantified perfectly, i.e. the power in the useful signal to the power in imperfections such as (noise power and distortion power) have improved. This shows of high quality evaluation of detection, as cleared in figures- 12 and 13.

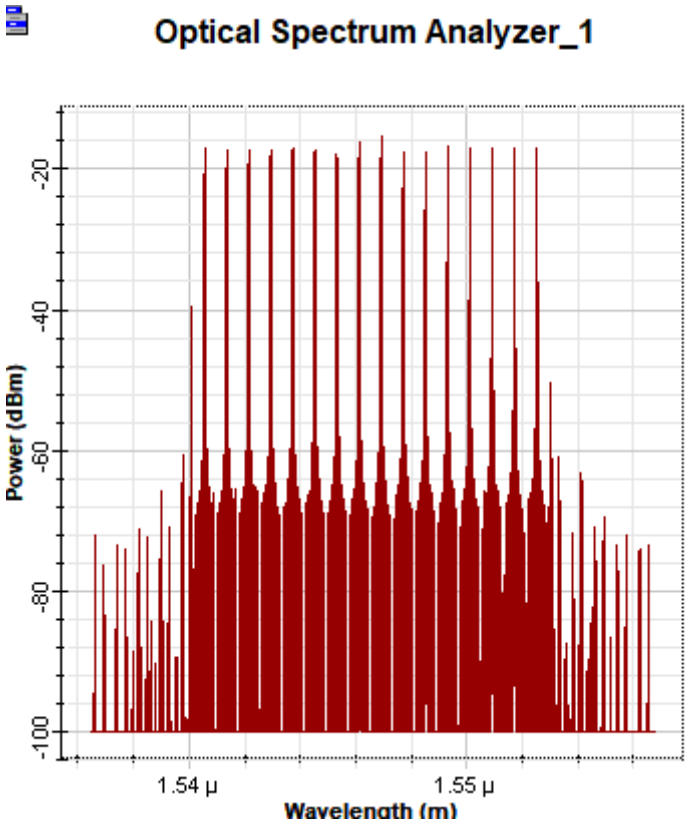

Figure 8. Spectrum in Receiver of 16 channel OFDM system before trying PMD Emulator

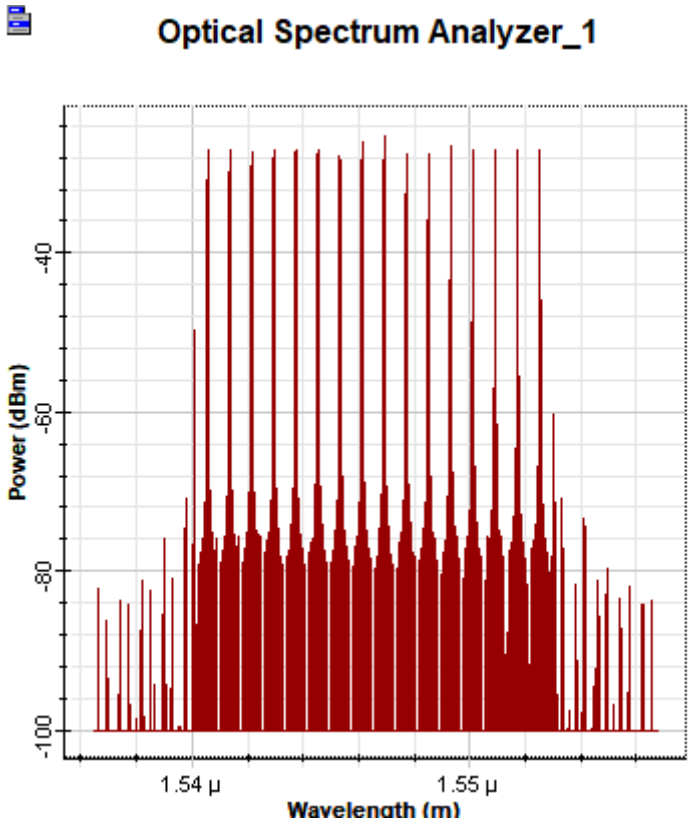

Figure 9. Spectrum in Receiver of 16 channel OFDM system after trying PMD Emulator

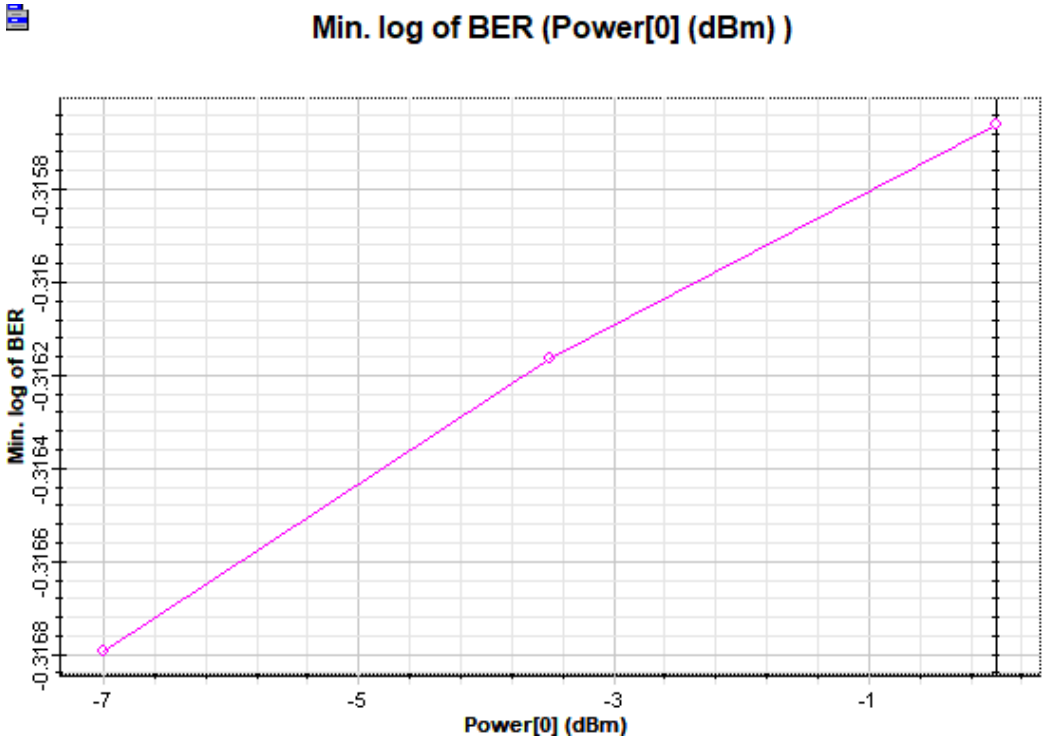

Figure 10. BER vs Power before trying PMD Emulator

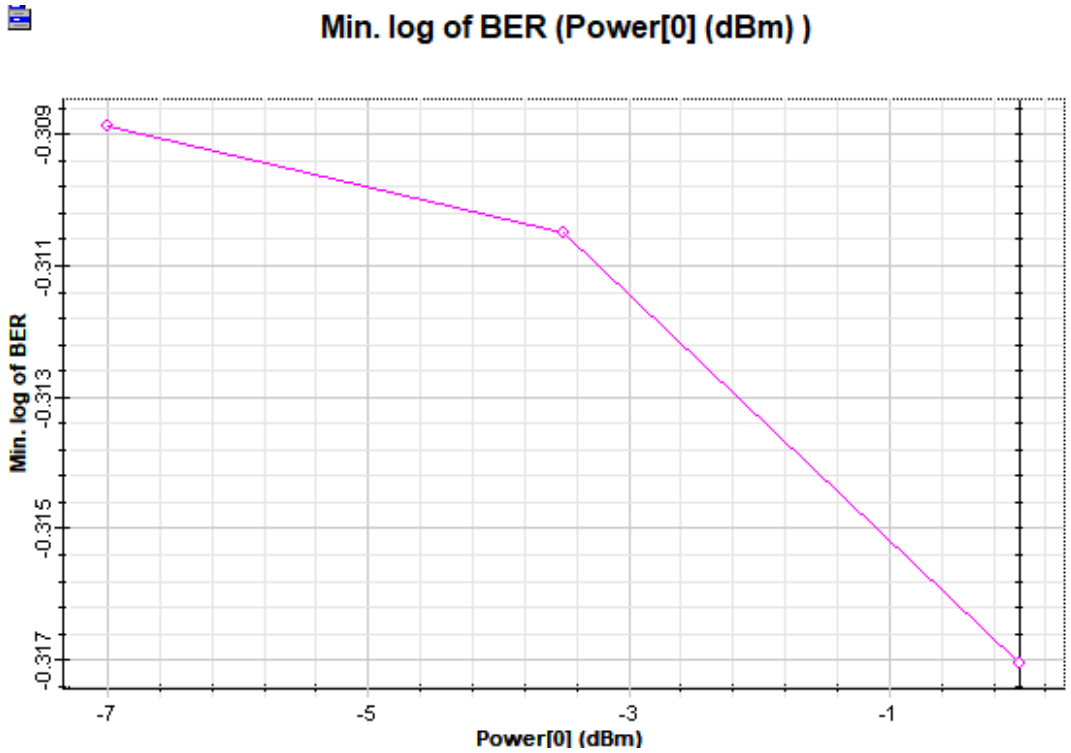

Figure 11. BER vs Power after trying PMD Emulator

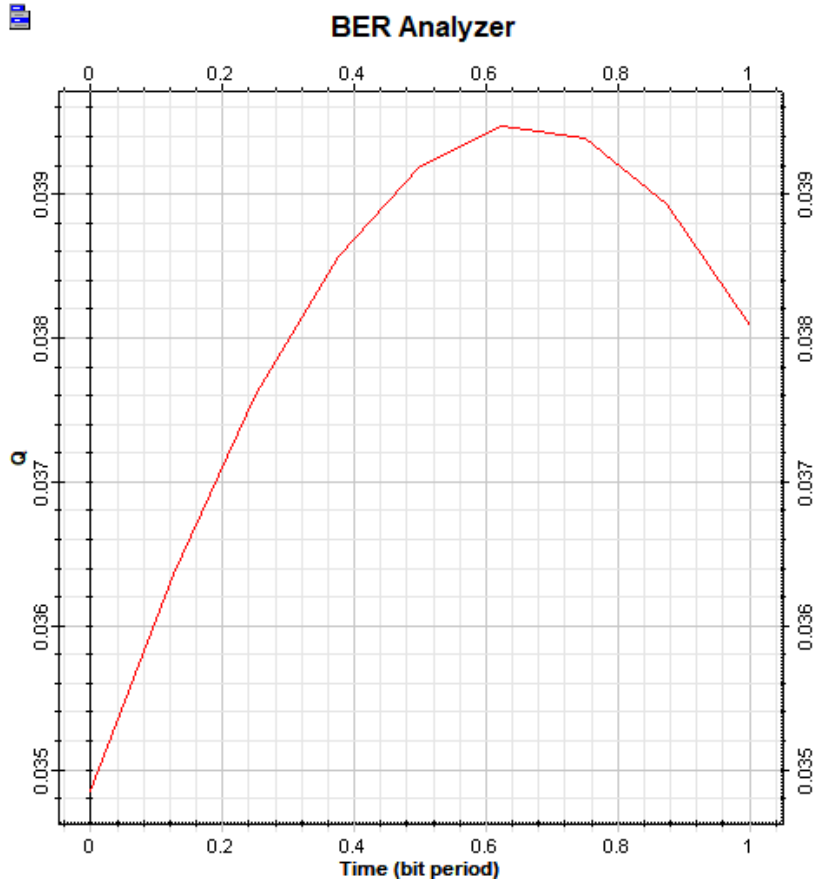

Figure 12. Signal Quality before trying PMD Emulator

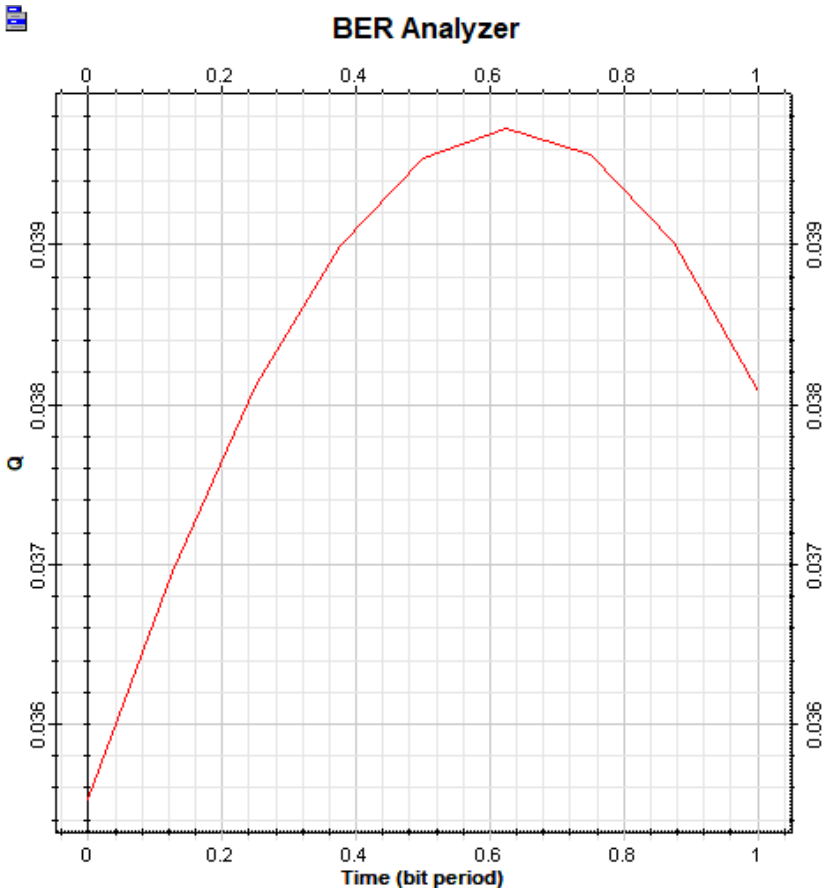

Figure 13. Signal Quality after trying PMD Emulator

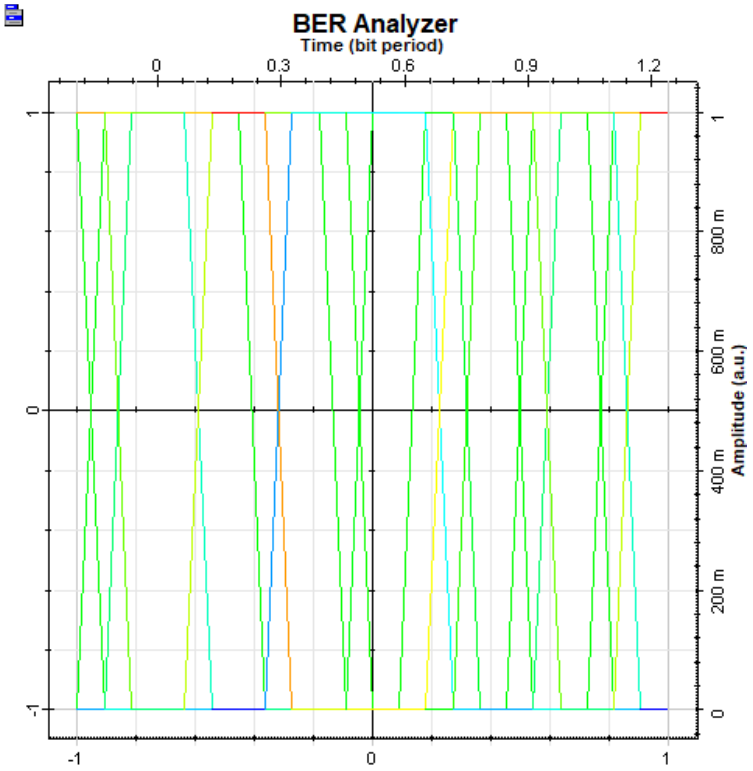

Figure 14. The BER Analyzer after trying PMD Emulator

Table 2: Data of the Results Output Figures

Figure No.	Description	Before Trying PMD-Emulator	After Trying PMD-Emulator
8, 9	Receiver Spectrum	FWM = -67 dBm	FWM = -77 dBm
10, 11	BER vs Power	-0.31563	-0.317
12, 13	Signal Quality	0.03944 at 0.62s Bit-Period	0.03979 at 0.62s Bit-Period

7. Conclusion

On the bases of the results, it is possible to conclude that OFDM viewed as a favorable applicant for high capacity transmission systems for the time being and ahead. In the system, its evidence decreases the effect of nonlinearity, which attacks the channel as ISI that called FWM when WDM used for transmitting multiple channels together. This investigation, therefore, has proposed using this advanced modulation technique OFDM with PMD-Emulator utilization together in fiber optic communication systems transmitting a bundle of carriers along a single fiber line with different colors that called WDM. These two techniques are used for decreasing the FWM appear among the channel signals. As we can see in the results and discussion section, the improvement of the transmission channels has been done by testing the circuit design with and without using PMD-Emulator with utilization of OFDM advanced modulation technique.

The circuit design simulation done by using Optisystem-15 software program, the results of received spectrums difference of the two cases showed, without using PMD-Emulator -67dBm FWM power strength, this result decreased to -77dBm when we used PMD-Emulator in the design and we raised our signal quality value from 0.03944 to 0.03979. Finally, this investigation shows that the results of implementing OFDM and PMD-Emulator together give higher FWM suppression improvement versus the results of the researchers got by using other techniques as mentioned in simulation results and discussion section in detail.

In future, we can extend the process of evaluation of WDM performance to examine with other available techniques in various groups for minimizing impact of nonlinear breakdown WDM optical fiber communication system.

References

Ahmed, N and Rashid, MA. (2018). Journal of Optical Communications. *Performance of hybrid OCDMA/WDM scheme under DPSK and QPSK modulation using spectral direct detection technique for optical communication networks, 1*(ahead-of-print).

Alberto Paradisi, Rafael Carvalho Figueiredo, Andrea Chiuchiarelli, Eduardo De Souza Rosa Editors. (2019). Optical Communications Advanced Systems and Devices for Next Generation Networks. *Springer Nature Switzerland AG*.

Alifdal, Hanane and Abdi, Farid and Abbou, Fouad Mohammed. (2017). Performance analysis of an 80Gb/s WDM system using OQPSK modulation under FWM effect and chromatic dispersion. *2017 International Conference on Wireless Technologies, Embedded and Intelligent Systems (WITS)* (pp. 1--6). IEEE.

Arpan Garg, and Nitin Mittal. (2020). A Comprehensive Survey on OFDM Based Radio over Fiber Modulation System. *ResearchGate, 20*(2), 11714 - 11727.

Beniwal, Poonam and Kedia, Deepak. (2018). Analysis of Four Wave Mixing Effects in 16$\times$ 10 Gb/S WDM Optical Communication System. *Journal of Optical Communications, 1*(ahead-of-print).

Chauhan, Anu, Arti Vaish, and Ashu Verma. (2018). To Decrease Maintenance Issues using FWM in Ultradense WDM Systems and Enhancing Optimum Placement of Optical Phase Conjugation. *Journal of Optical Communications , 1.*(ahead-of-print).

Chung, Hsiang-Yu and Liu, Wei and Cao, Qian and Song, Liwei and Kartner, Franz X and Chang, Guoqing. (2018). Megawatt peak power tunable femtosecond source based on self-phase modulation enabled spectral selection. *Optics express, 26*(3), 3684--3695.

David Zabala-Blanco 1, Marco Mora 1, Cesar A. Azurdia-Meza 2 , Ali Dehghan Firoozabadi 3 , Pablo Palacios Játiva 2 and Ismael Soto 4. (2020). Relaxation of the Radio-Frequency Linewidth for Coherent-Optical Orthogonal Frequency-Division Multiplexing Schemes by Employing the Improved Extreme Learning Machine. *MDPI, 45*(9).

Davinder Parkash Chechi, and Sukhpreet Singh. (2019). Analysis and Design of WDM Optical OFDM System with Coherent Detection Using Different Channel Spacing. *ResearchGate, 45*(9).

Dubovan, Jozef and Litvik, Jan and Benedikovic, Daniel and Mullerova, Jarmila and Glesk, Ivan and Veselovsky, Andrej and Dado, Milan. (2020). Impact of wind gust on high-speed characteristics of polarization mode dispersion in optical power ground wire cables. *Sensors, 20*(24), 7110.

Fazal Muhammad 1 , Farman Ali 2, Ghulam Abbas 3 , Ziaul Haq Abbas 4, Shahab Haider 5,Muhammad Bilal 6, Md. Jalil Piran 7 and Doug Young Suh 8. (2021). Palliation of Four-Wave Mixing in Optical Fibers Using Improved DSP Receiver. *MDPI, 124*(15).

Jianxin Du, Jialin Wu, and Tao Miao. (2019). Modeling inter-subcarrier four-wave mixingnoises in QAM coherent OFDM system using phase-conjugated twin waveswith diaversty implement domaines. *Optics Communications, 385*(1), 261--268.

Jozef Dubovan 1, Jan Litvik 1 , Daniel Benedikovic 1, Jarmila Mullerova 1, Ivan Glesk 2 ,Andrej Veselovsky 3 and Milan Dado 1. (2020). Impact of Wind Gust on High-Speed Characteristics of Polarization Mode Dispersion in Optical Power Ground Wire Cables. *white paper, avaiable from:< www. corning. com/WorkArea/downloadasset. aspx.*

Manzoor, Habib Ullah and Zafar, Muhammad and Manzoor, Sana Ullah and Khan, Talha and Liu, Songzuo and Manzoor, Tareq and Saleem, Saqib and Kim, Woo Young and Ali, Muddassir. (2020). Improving FWM efficiency in bi-directional ultra DWDM-PON networking centered light source by using PMD emulator. *Results in Physics, 16*(1), 102922.

Muhammad Irfan 1, Farman Ali 2 , Fazal Muhammad 3, Usman Habib 4, Abdullah S. Alwadie 1, Adam Glowacz 5, Ziaul Haq Abbas 6 and Eliasz Kan´toch 7. (2020). DSP-Assisted Nonlinear Impairments Tolerant 100 Gbps Optical Backhaul Network for Long-Haul Transmission. *MDPI, 125*(17).

Petr Ivaniga1, and Tomáš Ivaniga2. (2020). Mitigation of non-linear four-wave mixing phenomenon in. *5th IEEE International Conference on Advanced Computing & Communication Technologies [ICACCT-2011]* (p. 2878~2885). TELKOMNIKA.

Salim, N. (2019). Robustness of Modulation Formats Technique to Four Wave Mixing Crosstalk Under 80 Gbps Data Rate. *Journal of University of Babylon for Engineering Sciences*, 42--49.

Xiang Liu. (2019). Evolution of Fiber-Optic Transmission and Networking toward the 5G Era. *iScience, 45*(9).